TIME-DELAYED BILATERAL TELEOPERATION OF AN AERIAL MANIPULATOR

André Fialho Coelho

Dissertação de Mestrado apresentada ao Programa de Pós-graduação em Engenharia Elétrica, COPPE, da Universidade Federal do Rio de Janeiro, como parte dos requisitos necessários à obtenção do título de Mestre em Engenharia Elétrica.

Orientador: Fernando Cesar Lizarralde

Rio de Janeiro
Dezembro de 2019

TIME-DELAYED BILATERAL TELEOPERATION OF AN AERIAL MANIPULATOR

André Fialho Coelho

DISSERTAÇÃO SUBMETIDA AO CORPO DOCENTE DO INSTITUTO ALBERTO LUIZ COIMBRA DE PÓS-GRADUAÇÃO E PESQUISA DE ENGENHARIA (COPPE) DA UNIVERSIDADE FEDERAL DO RIO DE JANEIRO COMO PARTE DOS REQUISITOS NECESSÁRIOS PARA A OBTENÇÃO DO GRAU DE MESTRE EM CIÊNCIAS EM ENGENHARIA ELÉTRICA.

Examinada por:

Prof. Fernando Cesar Lizarralde, D.Sc.

Prof. Antonio Candea Leite, D.Sc.

Prof. Fernando Pereira Duda, D.Sc.

Prof. Ramon Romankevicius Costa, D.Sc.

RIO DE JANEIRO, RJ – BRASIL
DEZEMBRO DE 2019

Coelho, André Fialho

Time-Delayed Bilateral Teleoperation of an Aerial Manipulator/André Fialho Coelho. – Rio de Janeiro: UFRJ/COPPE, 2019.

XII, 81 p.: il.; 29, 7cm.

Orientador: Fernando Cesar Lizarralde

Dissertação (mestrado) – UFRJ/COPPE/Programa de Engenharia Elétrica, 2019.

Referências Bibliográficas: p. 77 – 81.

1. Manipulação aérea. 2. Telemanipulação. 3. Controle de corpo completo. 4. Passividade no domínio do tempo. I. Lizarralde, Fernando Cesar. II. Universidade Federal do Rio de Janeiro, COPPE, Programa de Engenharia Elétrica. III. Título.

Acknowledgments

Firstly, I would like to thank my wife, Raquel, as my greatest supporter and inspiration. I would also like to express my gratitude to my family for their caring and support. Without them, nothing would have been possible.

Moreover, I would like to thank my supervisor, Prof. Fernando Lizarralde, for his valuable guidance and exciting lectures. I would also like to give special thanks to my colleagues from the Federal University of Rio de Janeiro, who made the (sometimes stressful) experience of taking a great deal of courses in a short period of time much more pleasant.

Ultimately, I would like to thank my DLR colleagues from both the Flying Robots and the Telepresence group for their support, collaboration, and the numerous exciting discussions. I would also like to express my gratitude to my mentors, Dr. Christian Ott and Dr. Konstantin Kondak, for sharing their valuable knowledge and experience.

Resumo da Dissertação apresentada à COPPE/UFRJ como parte dos requisitos necessários para a obtenção do grau de Mestre em Ciências (M.Sc.)

TELEOPERAÇÃO BILATERAL DE UM MANIPULADOR AÉREO SUJEITA A ATRASOS

André Fialho Coelho

Dezembro/2019

Orientador: Fernando Cesar Lizarralde

Programa: Engenharia Elétrica

O presente trabalho apresenta uma estrutura que permite a realização de telemanipulação aérea estável e de alto desempenho com manipuladores aéreos completamente atuados. A fim de cumprir tal objetivo, um controlador baseado em passividade no domínio do tempo foi aplicado a fim de lidar com as fontes de instabilidade introduzidas pelo canal de comunicação, como atrasos, perda de pacotes e *jitter*. Além disso, foi desenvolvido um compensador de desvio baseado na abordagem de passividade no domínio do tempo (TDPA) visando melhorar as características de sincronização de posição do sistema de teleoperação. Além de compensar o desvio causado pelo controlador de passividade, o método proposto garante que as forças de teleoperação permaneçam dentro de uma faixa segura de magnitude. A abordagem de compensação de desvio também foi estendida a fim de permitir sua aplicação a robôs com múltiplos graus de liberdade, incluindo o *DLR Suspended Aerial Manipulator* (SAM). A eficácia do compensador de desvio proposto foi demonstrada através de simulações e experimentos em hardware. Somado a isso, devido à redundância de tais sistemas robóticos, uma estrutura de controle de corpo completo foi aplicada a fim de permitir que o operador comande poses de efetuador no espaço cartesiano enquanto uma tarefa secundária é realizada de forma autônoma no espaço nulo, sem que o sistema de teleoperação seja afetado. Validação numérica foi realizada a fim de demonstrar a aplicabilidade da estrutura proposta a cenários de telemanipulação aérea sujeita a atrasos de comunicação.

Abstract of Dissertation presented to COPPE/UFRJ as a partial fulfillment of the requirements for the degree of Master of Science (M.Sc.)

TIME-DELAYED BILATERAL TELEOPERATION OF AN AERIAL MANIPULATOR

André Fialho Coelho

December/2019

Advisor: Fernando Cesar Lizarralde

Department: Electrical Engineering

This thesis presents a framework to allow stable and performant aerial telemanipulation with fully-actuated aerial manipulators. In order to fulfill this objective a time-domain passivity-based controller was applied to cope with the sources of instability introduced by the communication channel, namely time delay, package loss, and jitter. Additionally, in order to improve the position synchronization characteristics of the teleoperation system, a Time Domain Passivity Approach (TDPA) based drift compensator was developed, which, in addition to compensating the drift caused by the passivity controller, ensures that the teleoperation forces remain within a safe range. The drift-compensation approach was also extended to allow its application to multi-DoF robots, including the DLR Suspended Aerial Manipulator (SAM). The efficacy of the proposed drift compensator was demonstrated through simulations and hardware experiments. Adding to that, due to the redundancy of such systems, a whole-body control framework was applied in order to allow the human operator to command Cartesian end-effector poses while a secondary task is autonomously fulfilled in the null space without disturbing the teleoperation system. Numerical validation was performed in order to demonstrate the applicability of the proposed framework to time-delayed aerial telemanipulation scenarios.

Contents

List of Figures

List of Tables

Chapter 1

Introduction

1.1 Aerial Manipulation

The use of unmanned aerial vehicles (UAVs) as a flying base for robotic manipulators has been object of intensive research in the recent years [1–5]. One of the main goals of such systems is to replace and assist humans in tasks as inspection and repairing of bridges, high-voltage electric lines, and wind-turbine rotor blades [2].

Despite the rapid development of new technologies in this field, in order to be able to replace humans in dangerous tasks, two aspects of aerial manipulators still have to be explored:

- Safety and reliability;
- Power and dexterity.

The first aspect relates to the capacity of robotic systems to match human capabilities in terms of generated forces and velocities. The second characteristic refers to the ability of performing tasks correctly without putting material resources and human integrity at risk.

To this date, multiple small aerial manipulation systems have been developed in order to perform safe and reliable tasks [1, 2, 6–8]. However, most of them lack the necessary power to perform human tasks. On the other hand, some large-sized aerial manipulators can match human power and dexterity [9–11]. Nevertheless, those lack the necessary safety and reliability to perform tasks.

The large-sized platforms developed to this date consist of an industrial robotic manipulator attached to an autonomous helicopter. The helicopter is meant to fly close enough to the manipulation object and hover above it while the robotic arm performs the manipulation task. Although being comparable to human workers in terms of strength, some safety issues might appear when dealing with such aerial manipulators. The first issue relates to the size of the rotor blades, which restricts

Figure 1.1: A prototype of the Suspended Aerial Manipulator.

the application of those systems to open spaces. Adding to that, manipulation tasks involve making direct contact with the environment and, in case of unpredictably high contact forces, the stability of the helicopter might be jeopardized, causing the system to crash.

In that scope, a novel Suspended Aerial Manipulator (SAM) has been developed in order to allow powerful aerial manipulation while enhancing the safety of the task [12]. The system consists of an industrial robotic manipulator fixed to an octarotor, which is attached to an autonomous helicopter or a crane by means of actuated cables (see Fig. 1.1). With this novel construction, the safety of the system is enhanced since the helicopter rotor blades are far from the manipulation task space. The octarotor, which is used to stabilize the base of the manipulator, is less prone to collide with the environment due to its reduced size. Adding to that, in case an unexpected collision happens, the outcome would be less disastrous for the two following reasons. First, due to their smaller size compared to the helicopter blades, the octarotor blades do not cause as much hazard. Second, in case an accident happens, the helicopter could still be kept stable and would be able to fly back to a desired home location.

In order to be considered suitable, the aerial manipulator has to be able to stably perform aerial manipulation tasks in a safe and reliable way. Due to the complexity of aerial manipulation applications, bilateral teleoperation presents itself as a solution to tasks which would not be otherwise autonomously performed.

Another interesting issue that comes out when dealing with the Suspended Aerial Manipulator is related to its redundancy. Due to its large number of degrees of freedom, such system can be present internal motions, which do not affect the end-effector at kinematic level. However, if not properly treated, these motions can dynamically interfere in the end-effector task being performed, putting its passivity

properties at risk.

1.2 Bilateral Telemanipulation

Despite being able to autonomously fulfill a significant range of objectives, state-of-the-art robots still need human assistance to perform more complex or unforeseen tasks [13]. The level of human participation in robotic tasks can range from supervised autonomy [14] to direct telemanipulation [15–18]. In the latter, an important characteristic of the telemanipulation setup is to be able to passively interact with the environment and the human operator.

1.2.1 Time Domain Passivity Approach

Among the passivity-based telemanipulation approaches [19, 20] developed to solve that issue, Time Domain Passivity Approach (TDPA, [21, 22]) presents the advantage of adapting the energy dissipation necessary to passivate the teleoperation channel based on measurements of the flow and effort variables acting on the system. This characteristic allows the implementation of a model-independent passivity observer and passivity controller (PO-PC) pair, which is robust to varying time delays and package losses in the communication channel. The adaptive characteristic of TDPA results in better performance compared to other passivity-enforcing controllers for teleoperation, e.g., wave-variable methods (see [23]).

Nevertheless, in spite of being able to render the communication channel passive, TDPA presents the drawback of creating position drift between master and slave devices whenever the PO-PC pair is applied in admittance configuration, which is necessary in many telemanipulation architectures ([15, 18, 22, 24]).

1.2.2 Drift Compensation in TDPA

In order to tackle this issue, Artigas et al. [25] proposed a compensator that modifies the existing PO-PC in order to inject energy into the system to compensate for the existing drift. Later, Chawda et al. [26] adapted Artigas' compensator in order keep the original TDPA formulation by using a virtual velocity injection source before the PO-PC. Despite being able to compensate for the position drift, these two methods present a drawback. As mentioned by Chawda et al. [26], force spikes are generated when drift compensation happens after significant position drift has been accumulated. This behavior affects the natural feeling desired for teleoperation since force spikes are suddenly felt by the operator during free-space motion or wall contact. Adding to that, these spikes can put the hardware and the human operator's integrity at risk.

Moreover, the efficacy of TDPA-based compensation methods has been shown through its application to one-degree-of-freedom (1-DoF) devices or in a concatenated manner, treating each DoF as an independent system. Nevertheless, no multi-DoF application of TDPA-based compensators has been tackled to this date.

1.3 Problem Statement

In light of that, in order to allow bilateral telemanipulation of the Suspended Aerial Manipulator, the following issues have to be tackled:

- Applying a local control framework that allows bilateral telemanipulation of the end-effector without having to take the energy acting in its null space into account;
- Developing a multi-DoF drift compensation method, that preserves the performance of the local controller in the presence of delays while keeping the control forces in their normal range.

1.4 Contribution

In that scope, this thesis describes the steps to applying a previously presented dynamic decoupling controller for kinematically redundant robots in order to allow passive bilateral teleoperation of the end-effector of redundant aerial manipulators, like the SAM. In addition, a novel drift compensation method for TDPA-based teleoperation is proposed, which presents the following advantages:

- As in [26], the approach is also based on TDPA and carries along the advantages of such formulation.
- The approach provides smoother drift compensation (with lower forces caused by the compensator), enhancing the natural feeling of free-space motion and wall contact.
- A way of tuning the behavior of the compensator in order to achieve desired performance (smoothness and compensation speed) is provided.

An extension of the previously presented drift compensators [25, 26] as well as the proposed one to multi-DoF robotic systems is also provided. In addition, a convergence analysis is carried out. It is shown that, if the gains are kept within a given range and if allowed by the passivity condition, the presented method is able to successfully reduce the accumulated drift caused by admittance type passivity controllers in TDPA.

The proposed framework, as well as its composing elements, is validated through numerical simulation and hardware experiments, which show its efficacy in allowing stable bilateral telemanipulation of aerial manipulators and other redundant robots.

1.5 Thesis Outline

The remainder of this thesis is divided as follows: Chapter 2 provides an introduction to Lie groups and Lie algebra as well as geometric control techniques that are used in the subsequent chapters. Chapter 3 provides an overview of the Time Domain Passivity Approach, introduces the proposed 1-DoF and multi-DoF drift compensators, and shows experimental results of their implementation. Chapter 4 presents whole-body control techniques used to decouple the Cartesian and null-space dynamics of redundant manipulators in order to perform Cartesian-space teleoperation. In addition, a two-task controller for the Suspended Aerial Manipulator is proposed and validated though Numerical simulation. Chapter 5 provides a numerical evaluation of time-delayed bilateral teleoperation of the Cartesian space of the redundant Aerial Manipulator with drift compensation and whole-body control techniques. Lastly, Chapter 6 concludes the thesis and briefly discusses the future work.

Chapter 2

Geometric Control of Robot Manipulators

2.1 Overview

This chapter briefly introduces two useful mathematical groups, namely, the Special Orthogonal group of rigid body rotations, $SO(3)$, and the Special Euclidean group of rigid body motions, $SE(3)$. In addition, their Lie algebras [27], which are used to represent rigid-body velocities and time-derivatives of rigid body motions, are also presented. After describing a way defining rigid-body poses and velocities as elements of these groups and presenting the kinematics and dynamics of manipulators, proportional (P) and proportional-derivative (PD) control techniques are described, which allow regulation and tracking tasks to be performed on these groups. This chapter is mainly based on the works of BULLO and LEWIS [27], BULLO and MURRAY [28], MURRAY [29]. The reader is referred to those references for a more comprehensive discussion on geometric control of robots.

2.2 The $SO(3)$ and $SE(3)$ Groups and Their Lie Algebras

2.2.1 The Special Orthogonal Group $SO(3)$

The $SO(3)$ group is a subgroup of the general linear group of 3×3 nonsingular real matrices, $GL(3, \mathbb{R})$, which can be defined as [29]

$$SO(3) = \{\boldsymbol{R} \in GL(3, \mathbb{R}) : \boldsymbol{R}^T \boldsymbol{R} = I, \det \boldsymbol{R} = 1\}. \tag{2.1}$$

The elements of this group can be used to represent the basis vectors of a right-handed coordinate frame in $\mathbb{R}^3$ with respect to another coordinate frame. They also can be used to represent rotation or change of coordinate frame actions on elements of $\mathbb{R}^3$ defined by linear maps $\boldsymbol{R} : \mathbb{R}^3 \to \mathbb{R}^3$ of the form $\boldsymbol{R}(\boldsymbol{x}) = \boldsymbol{R}\boldsymbol{x}$.

The Lie algebra of $SO(3)$ is $\mathfrak{so}(3)$. An element of $\mathfrak{so}(3)$ can be represented in matrix form as

$$\widehat{\varphi} = \begin{bmatrix} 0 & -\varphi_3 & \varphi_2 \\ \varphi_3 & 0 & -\varphi_1 \\ -\varphi_2 & \varphi_1 & 0 \end{bmatrix}. \tag{2.2}$$

It is also useful to represent elements of $\mathfrak{so}(3)$ in $\mathbb{R}^3$ as $\varphi^T = \begin{bmatrix} \varphi_1^T & \varphi_2^T & \varphi_3^T \end{bmatrix}^T$, such that

$$\widehat{\varphi}\boldsymbol{x} = \varphi \times \boldsymbol{x}\,, \quad \forall \boldsymbol{x} \in \mathbb{R}^3\,, \tag{2.3}$$

where "$\times$" is the regular vector product.

2.2.2 The Special Euclidean Group $SE(3)$

The Special Euclidean Lie group $SE(3)$, whose elements are of the form $\boldsymbol{g} = (\boldsymbol{R}, \boldsymbol{p}) \in SO(3) \times \mathbb{R}^3$, where $\boldsymbol{R} \in SO(3)$ and $\boldsymbol{p} \in \mathbb{R}^3$ may be used to express the pose of a rigid body in space. Elements of the $SE(3)$ can also be expressed in matrix form as

$$\boldsymbol{g} = \begin{bmatrix} \boldsymbol{R} & \boldsymbol{p} \\ \boldsymbol{0} & 1 \end{bmatrix} \in SE(3)\,. \tag{2.4}$$

The action of this group on vectors in $\mathbb{R}^3$ is defined by $\boldsymbol{g}(\boldsymbol{x}) = \boldsymbol{R}\boldsymbol{x} + \boldsymbol{p}$, which can be represented by the matrix product

$$\begin{bmatrix} \boldsymbol{x}_0 \\ 1 \end{bmatrix} = \begin{bmatrix} \boldsymbol{R} & \boldsymbol{p} \\ \boldsymbol{0} & 1 \end{bmatrix} \begin{bmatrix} \boldsymbol{x} \\ 1 \end{bmatrix} \tag{2.5}$$

Furthermore, the velocity of a rigid body can be expressed by elements of the Lie algebra of $SE(3)$, namely $\mathfrak{se}(3)$, as

$$[\boldsymbol{V}]^\wedge = \begin{bmatrix} \widehat{\omega} & \boldsymbol{v} \\ \boldsymbol{0} & 0 \end{bmatrix} \in \mathfrak{se}(3)\,, \tag{2.6}$$

where $\widehat{\omega} \in \mathfrak{so}(3)$ is the angular velocity and $\boldsymbol{v} \in \mathbb{R}^3$ is the linear velocity component. Adding to that, due to the isomorphism between $\mathfrak{se}(3)$ and $\mathbb{R}^6$, it is useful to define the operators $[\cdot]^\wedge : \mathbb{R}^6 \to \mathfrak{se}(3)$ and $[\cdot]^\vee : \mathfrak{se}(3) \to \mathbb{R}^6$, such that the velocity of a rigid body can be expressed as $\boldsymbol{V} = \begin{bmatrix} \omega^T & \boldsymbol{v}^T \end{bmatrix}^T \in \mathbb{R}^6$, which can be represented in body (${}^B\boldsymbol{V}$) or in spatial frame (${}^S\boldsymbol{V}$) [29].

It is important to note that elements of the Lie algebra of both $SO(3)$ and $SE(3)$ can be used to either represent the matrix logarithmic state of the system (see Section 2.2.3) or its velocity [28]. The logarithmic state is denoted by $\boldsymbol{X} = (\widehat{\varphi}, \boldsymbol{q})$ while the velocity is denoted by $[\boldsymbol{V}]^{\wedge} = (\widehat{\omega}, \boldsymbol{v})$, where $\widehat{\varphi}$ and $\widehat{\omega} \in \mathfrak{so}(3)$ represent the logarithmic state and the velocity of elements of $SO(3)$, respectively.

2.2.3 Exponential and Logarithmic Maps

In both $SO(3)$ and $SE(3)$ there are special maps between the groups and their Lie algebra, which, to cite a few, can be used to define *metrics* on the group and express the solution to an initial value problem. Those maps are defined as follows [28]

Definition 2.2.1 (Exponential map)**.** Given $\widehat{\varphi} \in SO(3)$ and $\boldsymbol{X} = (\widehat{\varphi}, \boldsymbol{q}) \in SE(3)$,

$$\exp_{\mathrm{SO(3)}}(\widehat{\varphi}) = \mathbf{I} + sin||\varphi|| \frac{\widehat{\varphi}}{||\varphi||} + (1 - cos||\varphi||) \frac{\widehat{\varphi}^2}{||\varphi||^2}, \tag{2.7}$$

$$\exp_{\mathrm{SE(3)}}(\mathbf{X}) = \begin{bmatrix} \exp_{\mathrm{SO(3)}}(\widehat{\varphi}) & \boldsymbol{A}(\varphi)\boldsymbol{q} \\ \mathbf{0} & 1 \end{bmatrix}, \tag{2.8}$$

where $||\cdot||$ is the standard Euclidean norm, $\exp_{\mathrm{SO(3)}}(\mathbf{0}) = \mathbf{I}$, and

$$\boldsymbol{A}(\varphi) = \mathbf{I} + \left(\frac{1 - cos||\varphi||}{||\varphi||} \right) \frac{\widehat{\varphi}}{||\varphi||} + \left(1 - \frac{sin||\varphi||}{||\varphi||} \right) \frac{\widehat{\varphi}^2}{||\varphi||^2}, \tag{2.9}$$

$$\boldsymbol{A}(\mathbf{0}) = \mathbf{I}, \tag{2.10}$$

$$\boldsymbol{A}(\varphi)^{-1} = \mathbf{I} - \frac{1}{2}\widehat{\varphi} + (1 - \alpha(||\varphi||)) \frac{\widehat{\varphi}^2}{||\varphi||^2}, \tag{2.11}$$

where

$$\alpha(||\varphi||) \triangleq \frac{||\varphi||}{2} \cot\left(\frac{||\varphi||}{2} \right). \tag{2.12}$$

In addition, a useful identity is

$$\boldsymbol{A}(\varphi)^{-T} = \boldsymbol{A}(\varphi)^{-1} \exp_{\mathrm{SO(3)}}(\widehat{\varphi}), \tag{2.13}$$

where

$$\boldsymbol{A}(\varphi)^{-T} = \mathbf{I} + \frac{1}{2}\widehat{\varphi} + (1 - \alpha(||\varphi||)) \frac{\widehat{\varphi}^2}{||\varphi||^2}. \tag{2.14}$$

Definition 2.2.2 (Logarithmic map)**.** Given $(\boldsymbol{R}, \boldsymbol{p}) \in SO(3) \times \mathbb{R}^3$ such that $\mathrm{tr}(\boldsymbol{R}) \neq -1$,

$$\log_{SO(3)}(\boldsymbol{R}) = \frac{\gamma}{2sin\gamma} \left(\boldsymbol{R} - \boldsymbol{R}^T \right) \in \mathfrak{so}(3), \tag{2.15}$$

where $cos\gamma = \frac{1}{2}(\text{tr}(\boldsymbol{R}) - 1)$ and $|\gamma| < \pi$. Moreover,

$$\log_{SE(3)}(\boldsymbol{R}, \boldsymbol{p}) = \begin{bmatrix} \widehat{\varphi} & \boldsymbol{A}(\varphi)^{-1}\boldsymbol{p} \\ \boldsymbol{0} & 1 \end{bmatrix} \in \mathfrak{se}(3)\,, \tag{2.16}$$

where $\widehat{\varphi} = \log_{SO(3)}(\boldsymbol{R})$.

2.2.4 Adjoint Map and Lie Bracket

Along with the previous ones, there are another two definitions, which are useful in geometric control theory.

Definition 2.2.3 (Adjoint map and Lie bracket)**.** Given $\boldsymbol{X}, \boldsymbol{Y} \in \mathfrak{se}(3)$ and $\boldsymbol{g} = (\boldsymbol{R}, \boldsymbol{p}) \in SE(3)$,

$$\text{Ad}_{\boldsymbol{g}}(\boldsymbol{Y}) = \boldsymbol{g}^{-1}\boldsymbol{Y}\boldsymbol{g}\,, \tag{2.17}$$

$$[\boldsymbol{X}, \boldsymbol{Y}] = \boldsymbol{X}\boldsymbol{Y} - \boldsymbol{Y}\boldsymbol{X}, \tag{2.18}$$

are the adjoint map and the Lie bracket, respectively. Furthermore, given $[\boldsymbol{V}]^\wedge \in \mathfrak{se}(3)$ and $\boldsymbol{V} \in \mathbb{R}^6$ as its column vector representation,

$$\text{Ad}_{\boldsymbol{g}}([\boldsymbol{V}]^\wedge) = \begin{bmatrix} \boldsymbol{R} & \boldsymbol{0} \\ \widehat{\boldsymbol{p}}\boldsymbol{R} & \boldsymbol{R} \end{bmatrix} \boldsymbol{V}\,. \tag{2.19}$$

2.2.5 Dynamical Systems and Discrete-Time Integration on $SE(3)$

A dynamical system with state $\boldsymbol{g} \in SE(3)$ evolves according to the following differential equation in continuous time [28]

$$\dot{\boldsymbol{g}}(t) = [{}^S\boldsymbol{V}(t)]^\wedge\, \boldsymbol{g}(t) = \boldsymbol{g}(t)\, [{}^B\boldsymbol{V}(t)]^\wedge\,, \tag{2.20}$$

where ${}^B\boldsymbol{V}(t)$ and ${}^S\boldsymbol{V}(t)$ are the body and spatial velocities of $\boldsymbol{g}$ at time t, which are related through

$${}^S\boldsymbol{V}(t) = \text{Ad}_{\boldsymbol{g}}(t)\, {}^B\boldsymbol{V}(t)\,. \tag{2.21}$$

The recursive solution to (2.20) in discrete time, given a set of initial conditions, can be approximated to

$$\boldsymbol{g}(k) = \exp_{\text{SE(3)}}\left([{}^S\boldsymbol{V}(k)]^\wedge \Delta T\right)\, \boldsymbol{g}(k-1)\,, \tag{2.22}$$

$$\boldsymbol{g}(k) = \boldsymbol{g}(k-1)\exp_{\text{SE(3)}}\left([{}^B\boldsymbol{V}(k)]^\wedge \Delta T\right)\,. \tag{2.23}$$

2.3 Kinematics and Dynamics of Non-Redundant Robotic Manipulators

The kinematics of a robotic manipulator can be understood as the map (or a set thereof) between a space of generalized coordinates and the space of possible motions of a point of interest on the robot. In general, a vector of generalized coordinates is used to represent the joint angles of a manipulator with rotational joints at a given moment. On the other hand, the Special Euclidean group is usually suitable to represent the pose of a point of interest on the manipulator, usually the end-effector. The joint space, $\mathcal{Q}$, is embedded in $\mathbb{R}^n$, where n is the number of joints of the robot. Therefore, a set of joint angles at a given moment can be represented by a vector $\boldsymbol{q} \in \mathbb{R}^n$. In addition, the end-effector pose can be represented by a vector $\boldsymbol{g} \in SE(3)$. Finally, the forward-kinematic map between the two spaces of a given manipulator can be represented by

$$\boldsymbol{g} = \boldsymbol{f}(\boldsymbol{q})\,, \tag{2.24}$$

where $\boldsymbol{f}$ is assumed to be a differentiable map. Therefore, the relationship between the time derivatives of $\boldsymbol{q}$ and the vector representation of the body velocity of $\boldsymbol{g}$, denoted by $\boldsymbol{V} \in \mathbb{R}^6$ can be written as

$$\boldsymbol{V} = \frac{\partial \boldsymbol{f}}{\partial \boldsymbol{q}}\,\dot{\boldsymbol{q}} = \boldsymbol{J}(\boldsymbol{q})\,\dot{\boldsymbol{q}}\,, \tag{2.25}$$

where $\boldsymbol{J}(\boldsymbol{q}) \in \mathbb{R}^{m\times n}$ is the so-called Jacobian matrix. Here m is the dimension of the space used to represent the end-effector motions. In case $SE(3)$ is used, $m = 6$. See BULLO and LEWIS [27] for a discussion about dimensions of manifolds.

In case $n = m$ and under the assumption of full row-rank, which is locally achievable, the map $\boldsymbol{J}(\boldsymbol{q})$ will be a *homeomorphism* [27], and the (local) map from Cartesian to joint space can be defined as

$$\dot{\boldsymbol{q}} = \boldsymbol{J}(\boldsymbol{q})^{-1}\,\boldsymbol{V}\,. \tag{2.26}$$

Moreover, the dynamic model of a robotic manipulator with n joints can be represented in joint space as

$$\boldsymbol{M}(\boldsymbol{q})\ddot{\boldsymbol{q}} + \boldsymbol{C}(\boldsymbol{q},\dot{\boldsymbol{q}})\dot{\boldsymbol{q}} = \boldsymbol{\tau} - \boldsymbol{G}(\boldsymbol{q})\,, \tag{2.27}$$

where $\boldsymbol{M}(\boldsymbol{q}) \in \mathbb{R}^{n\times n}$ is the inertia matrix, $\boldsymbol{C}(\boldsymbol{q},\dot{\boldsymbol{q}})\dot{\boldsymbol{q}} \in \mathbb{R}^n$ is a vector of Coriolis and centrifugal forces, $\boldsymbol{G}(\boldsymbol{q}) \in \mathbb{R}^n$ is the gravitational generalized torque vector, and $\boldsymbol{\tau} \in \mathbb{R}^n$ is the control torque. Note that no external force other than gravity is

assumed.

In order to represent the manipulator dynamics acting on the end-effector, a change of coordinates can be performed as

$$\boldsymbol{\Lambda}_x(\boldsymbol{q}) = \left(\boldsymbol{J}(\boldsymbol{q})\,\boldsymbol{M}(\boldsymbol{q})^{-1}\,\boldsymbol{J}(\boldsymbol{q})^T\right)^{-1} \tag{2.28}$$

$$\boldsymbol{\mu}_x(\boldsymbol{q},\dot{\boldsymbol{q}}) = \boldsymbol{\Lambda}_x(\boldsymbol{q})\left(\boldsymbol{J}(\boldsymbol{q})\,\boldsymbol{M}(\boldsymbol{q})^{-1}\,\boldsymbol{C}(\boldsymbol{q},\dot{\boldsymbol{q}}) - \dot{\boldsymbol{J}}(\boldsymbol{q})\right)\boldsymbol{J}(\boldsymbol{q})^{-1}\,. \tag{2.29}$$

Such formulation allows the manipulator dynamics to be written as

$$\boldsymbol{\Lambda_x}(\boldsymbol{q})\dot{\boldsymbol{V}} + \boldsymbol{\mu}_x(\boldsymbol{q},\dot{\boldsymbol{q}})\boldsymbol{V} = \boldsymbol{J}(\boldsymbol{q})^{-T}(\boldsymbol{\tau} - \boldsymbol{G}(\boldsymbol{q}))\,, \tag{2.30}$$

where $\boldsymbol{\Lambda_x}(\boldsymbol{q})$ and $\boldsymbol{\mu}_x(\boldsymbol{q},\dot{\boldsymbol{q}})$ are the Cartesian Inertia and Coriolis matrices. It is also important to remark that the so-called passivity property holds for this group of systems, i.e.

$${}^B\boldsymbol{V}^T\left(\dot{\boldsymbol{\Lambda}}(\boldsymbol{g}) - 2\,\boldsymbol{\mu}(\boldsymbol{q},\dot{\boldsymbol{q}})\right){}^B\boldsymbol{V} = \boldsymbol{0}\,. \tag{2.31}$$

2.4 Geometric PD Control on $SO(3)$ and $SE(3)$

This section introduces some results on geometric PD control on $SO(3)$ and $SE(3)$. It starts by defining distance functions on those groups, which are later used to define asymptotically stable controllers on both groups.

2.4.1 Distance Functions on $SO(3)\times\mathbb{R}^3$ and Convergence on $SE(3)$

In order to define stability and convergence on $SE(3)$, two distance functions on $SO(3)$ and $\mathbb{R}^3$ can be defined as follows.

Definition 2.4.1 (Distance function on $\mathbb{R}^3$)**.** Given a vector $\boldsymbol{p}\in\mathbb{R}^3$, the regular Euclidean norm

$$||\boldsymbol{p}|| = (\boldsymbol{p}^T\boldsymbol{p})^{\frac{1}{2}} \tag{2.32}$$

is a distance function that defines the distance from $\boldsymbol{p}$ to the origin of $\mathbb{R}^3$.

Definition 2.4.2 (Distance function on $SO(3)$)**.** Given an element $\boldsymbol{R}\in SO(3)$, a distance function

$$||\boldsymbol{R}||_{SO(3)} = (\varphi^T\varphi)^{\frac{1}{2}}, \tag{2.33}$$

where $\varphi = [\log_{SO(3)}(\boldsymbol{R})]^\vee \in \mathbb{R}^3$, defines the distance of $\boldsymbol{R}$ to the identity element I.

Given these two definitions, a sufficient condition for convergence of a sequence on $SE(3)$ can be defined as follows.

Lemma 2.4.1 (Double-geodesic convergence on $SE(3)$)**.** *Given a sequence* $\{\boldsymbol{g}(k) = (\boldsymbol{R}(k)\,, \boldsymbol{p}(k))\}_{k\in\mathbb{N}}$*, where* k *is the index of a partition of a "time variable" as* $t_p = \{t_1, t_2, .., t_k, ...\}$*, a sufficient condition for convergence of this sequence to the identity element of* $SE(3)$ *is*

$$||\boldsymbol{p}(k)|| < ||\boldsymbol{p}(k-1)|| \quad \wedge \quad |\boldsymbol{R}(k)||_{SO(3)} < |\boldsymbol{R}(k-1)||_{SO(3)} \quad \forall k\,. \tag{2.34}$$

Sketch of Proof. Eq. 2.34 makes sure that, in matrix representation

$$\lim_{k\to\infty} \boldsymbol{R}(k) = I \quad \wedge \quad \lim_{k\to\infty} \boldsymbol{p}(k) = \boldsymbol{0}\,, \tag{2.35}$$

which implies that

$$\lim_{k\to\infty} \boldsymbol{g}(k) = \begin{bmatrix} \lim_{k\to\infty} \boldsymbol{R}(k) & \lim_{k\to\infty} \boldsymbol{p}(k) \\ \boldsymbol{0} & 1 \end{bmatrix} = I\,. \tag{2.36}$$

□

Furthermore, even though the function $||\boldsymbol{p}(k)|| + |\boldsymbol{R}(k)||_{SO(3)}$ is not adjoint invariant [28], the above defined $SO(3)$ and $\mathbb{R}^3$ distance functions can be used in Lyapunov functions to prove stability of control systems on $SE(3)$ (see [27]).

2.4.2 Double-Geodesic Regulation Control of Dynamical Systems on $SE(3)$

In case the velocity variables can be directly command, the following lemma holds.

Lemma 2.4.2 (Double-geodesic kinematic regulation)**.** *Given the control system* $\dot{\boldsymbol{g}}(t) = \boldsymbol{g}(t)\,[{}^B\boldsymbol{V}(t)]^\wedge$ *on* $SE(3)$ *where values of* ${}^B\boldsymbol{V}(t)$ *can be directly commanded and* K_ω *and* K_v *are positive definite symmetric matrices, the control law*

$$\begin{bmatrix} {}^B\omega \\ {}^B\boldsymbol{v} \end{bmatrix} = \begin{bmatrix} -K_\omega log_{SO(3)}(\boldsymbol{R}) \\ -\boldsymbol{R}^T K_v \boldsymbol{p} \end{bmatrix}\,, \tag{2.37}$$

asymptotically stabilizes the state g *at* I*, given any set of initial conditions* $(\boldsymbol{R}(0)\,, \boldsymbol{p}(0))$*, such that* $\mathrm{tr}(\boldsymbol{R}(0)) \neq 1$

Proof. See [28]. □

On the other hand, if the control variable is acceleration and the system under consideration is a fully actuated interconnection of rigid bodies with Cartesian (end-effector) body velocities and $SE(3)$ poses as the states, as is the case assumed in

Sections 2.3 and 4.2.2, the system dynamics can be defined as

$$\begin{cases} \dot{\boldsymbol{g}} = \boldsymbol{g}[{}^B\boldsymbol{V}]^\wedge \\ \boldsymbol{\Lambda}(\boldsymbol{g}){}^B\dot{\boldsymbol{V}} = -\boldsymbol{\mu}(\boldsymbol{g}, {}^B\boldsymbol{V}){}^B\boldsymbol{V} - \boldsymbol{N}(\boldsymbol{g}, {}^B\boldsymbol{V}) + U\,, \end{cases} \tag{2.38}$$

where $\boldsymbol{\Lambda}$, $\boldsymbol{\mu}$, $\boldsymbol{N}$ are the inertia, Coriolis, and friction-gravity matrices and U is the control wrench in body coordinates.

Lemma 2.4.3 (Stabilizing state-feedback control of mechanical systems)**.** *For the above described system, the following control law*

$$U(\boldsymbol{g}, {}^B\boldsymbol{V}) = \boldsymbol{N}(\boldsymbol{g}, {}^B\boldsymbol{V}) - \begin{bmatrix} k_\omega log_{SO(3)}(\boldsymbol{R}) \\ k_v \boldsymbol{R}^T \boldsymbol{p} \end{bmatrix} - K_d {}^B\boldsymbol{V} \tag{2.39}$$

asymptotically stabilizes the state at identity, if positive-definite gains k_v, $k_\omega \in \mathbb{R}$ and $K_d \in \mathbb{R}^{6\times 6}$ are used.

Proof. Asymptotic stability is proven using the following Lyapunov function [28].

$$W(\boldsymbol{g}, {}^B\boldsymbol{V}) = \frac{k_\omega}{2}||\boldsymbol{R}||^2_{SO(3)} + \frac{k_v}{2}||\boldsymbol{p}||^2 + \frac{1}{2}{}^B\boldsymbol{V}^T\boldsymbol{\Lambda}(\boldsymbol{g}){}^B\boldsymbol{V} + \epsilon \begin{bmatrix} \log_{SO(3)}(\boldsymbol{R}) \\ \boldsymbol{R}^T\boldsymbol{p} \end{bmatrix}^T \boldsymbol{\Lambda}(\boldsymbol{g}){}^B\boldsymbol{V}\,, \tag{2.40}$$

whose first derivative with respect to time is

$$\dot{W} = \begin{bmatrix} \varphi \\ \boldsymbol{p} \\ {}^B\omega \\ {}^B\boldsymbol{v} \end{bmatrix}^T \begin{bmatrix} Q_{11} & Q_{12} & Q_{13} & Q_{14} \\ Q_{21} & Q_{22} & Q_{23} & Q_{24} \\ Q_{31} & Q_{32} & Q_{33} & Q_{34} \\ Q_{41} & Q_{42} & Q_{43} & Q_{44} \end{bmatrix} \begin{bmatrix} \varphi \\ \boldsymbol{p} \\ {}^B\omega \\ {}^B\boldsymbol{v} \end{bmatrix}, \tag{2.41}$$

where $\varphi = \log_{SO(3)}(\boldsymbol{R})$ and

$$Q_{11} = -\epsilon k_\omega I_3 \tag{2.42}$$
$$Q_{12} = \mathbf{0}_3 \tag{2.43}$$
$$Q_{13} = \frac{\epsilon}{2}(\dot{\boldsymbol{\Lambda}}_{\omega\omega} + \boldsymbol{\mu}_{\omega\omega} - k_d I_3) \tag{2.44}$$
$$Q_{14} = \frac{\epsilon}{2}(\dot{\boldsymbol{\Lambda}}_{\omega v} + \boldsymbol{\mu}_{\omega v}) \tag{2.45}$$
$$Q_{21} = Q_{12}^T \tag{2.46}$$
$$Q_{22} = -\epsilon k_v I_3 \tag{2.47}$$

$$Q_{23} = \frac{\epsilon}{2}(\boldsymbol{R}(\dot{\boldsymbol{\Lambda}}_{\omega v}^T + \boldsymbol{\mu}_{v\omega}) + \dot{\boldsymbol{R}}\boldsymbol{\Lambda}_{\omega v}^T) \tag{2.48}$$

$$Q_{24} = \frac{\epsilon}{2}(\boldsymbol{R}(\dot{\boldsymbol{\Lambda}}_{vv} + \boldsymbol{\mu}_{vv} - k_d I_3) + \dot{\boldsymbol{R}}\boldsymbol{\Lambda}_{vv}) \tag{2.49}$$

$$Q_{31} = Q_{13}^T \tag{2.50}$$

$$Q_{32} = Q_{23}^T \tag{2.51}$$

$$Q_{33} = -k_d I_3 + \epsilon \boldsymbol{A}(\varphi)^{-1}\boldsymbol{\Lambda}_{\omega\omega} \tag{2.52}$$

$$Q_{34} = \frac{\epsilon}{2}(\boldsymbol{A}(\varphi)^{-1} + I_3)\boldsymbol{\Lambda}_{\omega v} \tag{2.53}$$

$$Q_{41} = Q_{14}^T \tag{2.54}$$

$$Q_{42} = Q_{24}^T \tag{2.55}$$

$$Q_{43} = Q_{34}^T \tag{2.56}$$

$$Q_{44} = -k_d I_3 + \epsilon \boldsymbol{\Lambda}_{vv}\,, \tag{2.57}$$

where the dynamic matrices are divided into 3×3 blocks as

$$\boldsymbol{\Lambda}(\boldsymbol{g}) = \begin{bmatrix} \boldsymbol{\Lambda}_{\omega\omega} & \boldsymbol{\Lambda}_{\omega v} \\ \boldsymbol{\Lambda}_{\omega v}^T & \boldsymbol{\Lambda}_{vv} \end{bmatrix}\,,\ \boldsymbol{\mu}(\boldsymbol{g}, {}^B\boldsymbol{V}) = \begin{bmatrix} \boldsymbol{\mu}_{\omega\omega} & \boldsymbol{\mu}_{\omega v} \\ \boldsymbol{\mu}_{v\omega} & \boldsymbol{\mu}_{vv} \end{bmatrix} \tag{2.58}$$

It can be noted that, assuming smooth and bounded dynamic matrices (i.e., away from singularities), stability can be proven by choosing ϵ small enough. □

It is important to remark that the $SO(3)$ and $\mathbb{R}^3$ distance functions described in Section 2.4.1 are used in the Lyapunov function.

2.4.3 Double-Geodesic Tracking Control on $SE(3)$

As described in BULLO and MURRAY [28] whenever tracking is desired, a composition of the desired pose and the actual one can be defined as $\boldsymbol{e} \triangleq \boldsymbol{g}_d^{-1}\boldsymbol{g} = (\boldsymbol{R}_e, \boldsymbol{p}_e)$ and a body-velocity error term $\boldsymbol{V}_e \triangleq \boldsymbol{V} - \mathrm{Ad}_{\boldsymbol{e}^{-1}}\boldsymbol{V}_d$ the following control law can be applied in order to ensure tracking of the desired pose.

Lemma 2.4.4 (Trajectory tracking controller)**.** *Given the mechanical system from (2.38), with $\boldsymbol{e}$ and $\boldsymbol{V}_e$ defined as above, the following controller asymptotically stabilizes the error $\boldsymbol{e}$ at $I \in SE(3)$.*

$$U = U_{ff} + U_{tr}(\boldsymbol{g}, \boldsymbol{V}, \boldsymbol{V}_d, \dot{\boldsymbol{V}}_d) + U_{reg}(\boldsymbol{e}, \boldsymbol{V}_e)\,, \tag{2.59}$$

where

$$Uff(\boldsymbol{g}, \boldsymbol{V}) = (\mu(\boldsymbol{g}, \boldsymbol{V}) \operatorname{Ad}_{\boldsymbol{e}^{-1}} \boldsymbol{V}_d + \boldsymbol{N}(\boldsymbol{g}, \boldsymbol{V})) \tag{2.60}$$

$$U_{tr}(\boldsymbol{g}, \boldsymbol{V}, \boldsymbol{V}_d, \dot{\boldsymbol{V}}_d) = \boldsymbol{\Lambda}(\boldsymbol{g}) \operatorname{Ad}_{\boldsymbol{e}^{-1}}(\dot{\boldsymbol{V}}_d) + \boldsymbol{\Lambda}(\boldsymbol{g})[\operatorname{Ad}_{\boldsymbol{e}^{-1}} \boldsymbol{V}_d, \boldsymbol{V}] \tag{2.61}$$

$$U_{reg}(\boldsymbol{e}, \boldsymbol{V}_e) = -\begin{bmatrix} -k_\omega log_{SO(3)}(\boldsymbol{R}_e) \\ -k_v \boldsymbol{R}_e^T \boldsymbol{p} \end{bmatrix} - K_d \boldsymbol{V}_e \tag{2.62}$$

Proof. Taking the first derivative of $\boldsymbol{V}_e$ with respect to time yields

$$\dot{\boldsymbol{V}}_e = \dot{\boldsymbol{V}} - \operatorname{Ad}_{\boldsymbol{e}^{-1}} \dot{\boldsymbol{V}}_d - [\operatorname{Ad}_{\boldsymbol{e}^{-1}} \boldsymbol{V}_d, \boldsymbol{V}]. \tag{2.63}$$

By substituting the expression for $\dot{\boldsymbol{V}}$ from (2.38) and the proposed control law from (2.59), the closed-loop dynamics satisfy

$$\begin{cases} \dot{e} = e[\boldsymbol{V_e}]^\wedge \\ \boldsymbol{\Lambda}(\boldsymbol{g})\dot{\boldsymbol{V}}_e = -\mu(\boldsymbol{g}, {}^B\boldsymbol{V})\boldsymbol{V}_e + U_{reg}(\boldsymbol{e}, \boldsymbol{V}_e). \end{cases} \tag{2.64}$$

It can be noted that, with the proposed control law, the problem simplifies to a regulation task on the error coordinates. Therefore, similarly to Lemma 2.4.3, the proposed law can be proven to asymptotically stabilize $(\boldsymbol{g}_e, [\boldsymbol{V}_e]^\wedge)$ at $(I, \boldsymbol{0}) \in SE(3) \times \mathfrak{se}(3)$ with the Lyapunov following function.

$$W(\boldsymbol{g}, \boldsymbol{e}, \boldsymbol{V}_e) = \frac{k_\omega}{2}||\boldsymbol{R}_e||^2_{SO(3)} + \frac{k_v}{2}||\boldsymbol{p}_e||^2 + \boldsymbol{V}_e^T \boldsymbol{\Lambda}(\boldsymbol{g}) \boldsymbol{V}_e + \epsilon \begin{bmatrix} \log_{SO(3)}(\boldsymbol{R}_e) \\ \boldsymbol{R}_e^T \boldsymbol{p}_e \end{bmatrix}^T \boldsymbol{\Lambda}(\boldsymbol{g}) \boldsymbol{V}_e, \tag{2.65}$$

whose time derivative would resemble (2.41) with the error coordinates instead of the regular pose and velocity coordinates. □

Chapter 3

Time Domain Passivity Approach-based Telemanipulation with Drift Compensation

3.1 Overview

In addition to presenting state-of-the art time-domain techniques for enabling passive bilateral telemanipulation, this chapter aims at introducing novel approaches for further improving the position synchronization capabilities of teleoperation systems. Initially, a drift compensation method for 1-DoF devices, firstly introduced in COELHO *et al.* [30], is presented and compared to state-of-the-art methods through experiments. Subsequently, a novel multi-DoF drift compensator, introduced in COELHO *et al.* [31], is presented, which can be regarded as an extension of the 1-DoF methods presented to this date, including the one developed by the author [30]. Experimental validation is provided through the application of the proposed approach to Cartesian-space teleoperation of 3-DoF commercially available haptic devices, as well as to the full 6-dimensional Cartesian Space of the DLR Bimanual Haptic Device (HUG).

3.2 Passivity of Dynamical Systems

Before presenting the approach used to ensure stable bilateral telemanipulation, the notion of passivity will be introduced in this section. The definitions presented here are taken from KHALIL [32].

It is assumed that the systems which will be dealt with in this thesis can be

represented (in local coordinates) by the following state model.

$$\dot{x} = f(x,u) \tag{3.1}$$

$$y = h(x,u)\,, \tag{3.2}$$

where $f : \mathbb{R}^n \times \mathbb{R}^p \to \mathbb{R}^n$, s.t. $f(0,0) = 0$, is locally Lipschitz [32] and $h : \mathbb{R}^n \times \mathbb{R}^p \to \mathbb{R}^p$, s.t. $h(0,0) = 0$, is continuous. It is assumed that the system has the same number of inputs and outputs.

Definition 3.2.1. The system (3.1)–(3.2) is said to be passive if there exists a continuously differentiable positive semidefinite function $W(x)$ (called the storage function) such that

$$u^T y \geq \dot{W} = \frac{\partial W}{\partial x} f(x,u),\ \forall\,(x,u) \in \mathbb{R}^n \times \mathbb{R}^p\ . \tag{3.3}$$

Moreover, it is said to be

- lossless if $u^T y = \dot{W}$.
- input-feedforward passive if $u^T y \geq \dot{W} + u^T \phi(u)$ for some function ϕ.
- input strictly passive if $u^T y \geq \dot{W} + u^T \phi(u)$ and $u^T \phi(u) \geq 0,\ \forall\, u \neq 0$.
- output-feedback passive if $u^T y \geq \dot{W} + y^T \rho(y)$ for some function ρ.
- output strictly passive if $u^T y \geq \dot{W} + y^T \rho(y)$ and $y^T \rho(y) \geq 0,\ \forall\, y \neq 0$.
- strictly passive if $u^T y \geq \dot{W} + \psi(x)$ for some positive-definite function ψ.

In all cases the inequality should hold for all (x,u).

It is important to remark that (3.3) is a condition on the power flow of the system, which is given by the inner product between the system input and output vectors [21] (or equivalently, the input covector applied to the output vector [27]). In addition to that definition, an energy-based definition of passivity could be defined as

$$\int_{t_0}^{t} u(\tau)^T y(\tau) d\tau \geq W(t) - W(t_0),\ \forall\,(y,u) \in \mathbb{R}^p \times \mathbb{R}^p\ . \tag{3.4}$$

In the approach defined subsequently, the passivity condition is defined as a discrete-time version of (3.4). Since no previous knowledge of the system is assumed, the computed inputs and outputs are adapted in order to fulfill the following condition.

$$\Delta T \sum_{j=0}^{k} u(j)^T y(j) \geq 0,\ \forall\,(y,u) \in \mathbb{R}^p \times \mathbb{R}^p\,, \tag{3.5}$$

where ΔT is the sampling interval. Assuming that the inputs and outputs do not change between samples, condition (3.5) ensures that the system (3.1)–(3.2) is passive.

3.3 Time Domain Passivity Approach

3.3.1 Overview

Time Domain Passivity Approach [21, 22] is a widely used method to ensure stability of bilateral teleoperation systems. It consists of measuring the energy flow in the system and adaptively dissipating energy in order to enforce passivity (see (3.3)–(3.5)). In contrast to methods where a damping element is designed for the worst case scenario (e.g. [19, 20]), TDPA adds adaptive damping components in order to dissipate only the necessary amount of energy, computed using measurements of the forces and velocities being exchanged.

In mechanical control systems, the most common control inputs are forces and torques, while the most common states are velocities and positions. One of the most widely used teleoperation schemes is the position-force (P-F) architecture [33]. A block diagram of this architecture is shown in Fig. 3.1. T_f and T_b are the forward and backward delays, respectively. $\boldsymbol{V}_m$ and $\boldsymbol{V}_s$ are the velocities of the master and slave devices. $\boldsymbol{F}_h$, $\boldsymbol{F}_e$, and $\boldsymbol{F}_s$ are the forces exerted by the human, the environment, and the slave controller, respectively. $\boldsymbol{V}_{sd}$ is the delayed master velocity that serves as reference to the slave, and $\boldsymbol{F}_m$ is the delayed slave computed force applied to the master device.

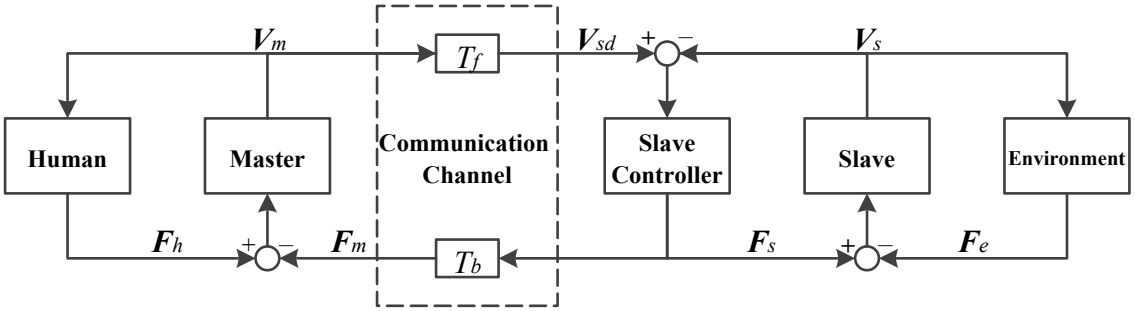

Figure 3.1: Block diagram representation of a P-F teleoperation architecture.

A useful tool to facilitate the application of TDPA is to describe the elements of the teleoperation system in circuit representation. This is achieved by using the velocity-current and force-voltage analogies. Besides allowing for the use of simple tools (e.g. Kirchoff's laws) to derive the dynamic equations, the circuit representation also enables the network representation of the system. This is particularly

important for TDPA, because it makes the power-conjugate pairs in the ports evident, enabling the computation of the energy flows in the system. From the block diagram in Fig. 3.1, a network representation, where the subsystems exchange force and velocity, can be derived. The network representation of the P-F architecture is shown in Fig. 3.2. In this representation the velocity-force pairs become more evident, and the energies at each node can be computed by taking the integral over time of the product of these two quantities.

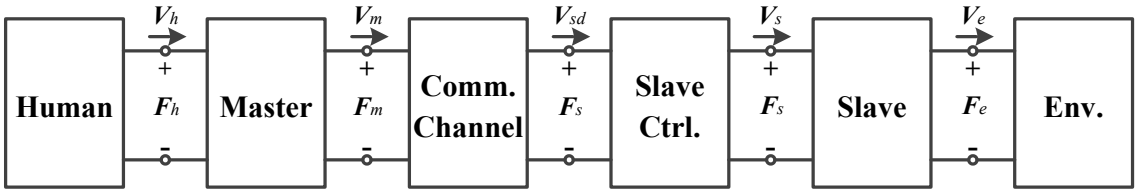

Figure 3.2: Network representation of a P-F teleoperation architecture.

In TDPA, the communication channel is usually represented by one or more Time Delay Power Networks (TDPNs, [22]), which are two-port networks that exchange velocities and forces. In addition to constant or variable time delays, TDPNs can also model package losses in the signals being transmitted. Fig. 3.3 shows the signal flow of a TDPN. E^M and E^S are the energies computed on the master and slave sides, respectively.

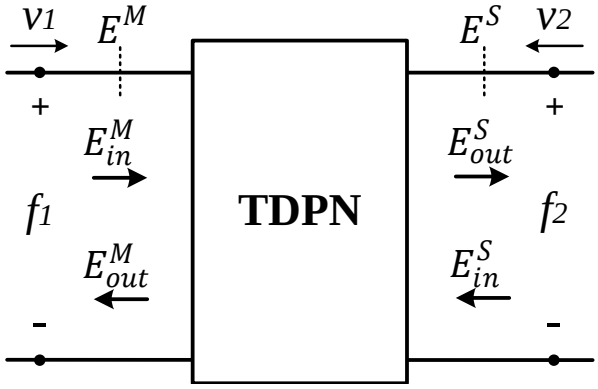

Figure 3.3: Signal flow of the TDPN.

The pairs $\mathbf{v}_1/\mathbf{f}_1$ and $\mathbf{v}_2/\mathbf{f}_2$ from Fig. 3.3 are the flow-effort pairs on each side of the TDPN, such that

$$E^M(k) = \Delta T \sum_{j=0}^{k} \mathbf{f}_1(j)^T \mathbf{v}_1(j), \tag{3.6}$$

$$E^S(k) = \Delta T \sum_{j=0}^{k} -\mathbf{f}_2(j)^T \mathbf{v}_2(j), \tag{3.7}$$

with $\mathbf{v}_1$, $\mathbf{v}_2$, $\mathbf{f}_1$, $\mathbf{f}_2$ being column vector representations in $\mathbb{R}^n$ of the flow and effort variables.

The energies on the sides of the TDPN are divided according to the direction of their flow (into or out of the TDPN) as

$$\begin{aligned} E^M(t) &= E^M_{in}(t) - E^M_{out}(t), \quad \forall t \geq 0, \\ E^S(t) &= E^S_{in}(t) - E^S_{out}(t), \quad \forall t \geq 0, \end{aligned} \tag{3.8}$$

where $E^M_{in}(t)$, $E^M_{out}(t)$, $E^S_{in}(t)$, and $E^S_{out}(t)$ are monotonically increasing and non-negative functions, representing the energies flowing in and out of the master and the slave. Note that these conditions can be regarded as discrete-time versions of the one presented in (3.3) with forces as inputs and velocities as outputs.

It is well known that, due to the presence of delays, the energies computed on each side of the TDPN are not readily available on the other side. However, the passivity of the channel can still be enforced through the following sufficient conditions

$$E^{L2R}_{obs}(t) = E^M_{in}(t - T_f(t)) - E^S_{out}(t) \geq 0, \quad \forall t \geq 0, \tag{3.9}$$

$$E^{R2L}_{obs}(t) = E^S_{in}(t - T_b(t)) - E^M_{out}(t) \geq 0, \quad \forall t \geq 0, \tag{3.10}$$

where $E^{L2R}_{obs}(t)$ and $E^{R2L}_{obs}(t)$ are the observed left-to-right and right-to-left energy flows observed on the right and left-hand sides of the TDPN.

Following the framework presented by ARTIGAS *et al.* [34], using a hybrid of circuit and network representation, the master and slave sides of the P-F architecture can be represented as shown in Figs. 3.4 and 3.5, respectively. There, the communication channel is represented by a TDPN. $\boldsymbol{V}_m$ and $\boldsymbol{V}_s$ are the velocities of the master and slave devices. $\boldsymbol{F}_s$ is the force exerted by the slave-side controller. $\tilde{\boldsymbol{V}}_{sd}$ is the delayed master velocity and $\hat{\boldsymbol{F}}_m$ is the delayed slave control force applied to the master device. $\boldsymbol{V}_{sd}$ and $\boldsymbol{F}_m$ are the delayed velocity and force after being modified by the passivity controllers (PC). $\boldsymbol{\alpha}$ and $\boldsymbol{\beta}$ are the impedance and admittance-type passivity controllers, respectively, while $\boldsymbol{V}_{ad}$ is the drift compensation velocity source, which will be addressed subsequently.

3.3.2 Passivity Observer

In order to take into account the energy removed by the passivity controllers up to the previous time steps ($E^M_{PC}(k-1)$ and $E^S_{PC}(k-1)$), the energy flow on each side

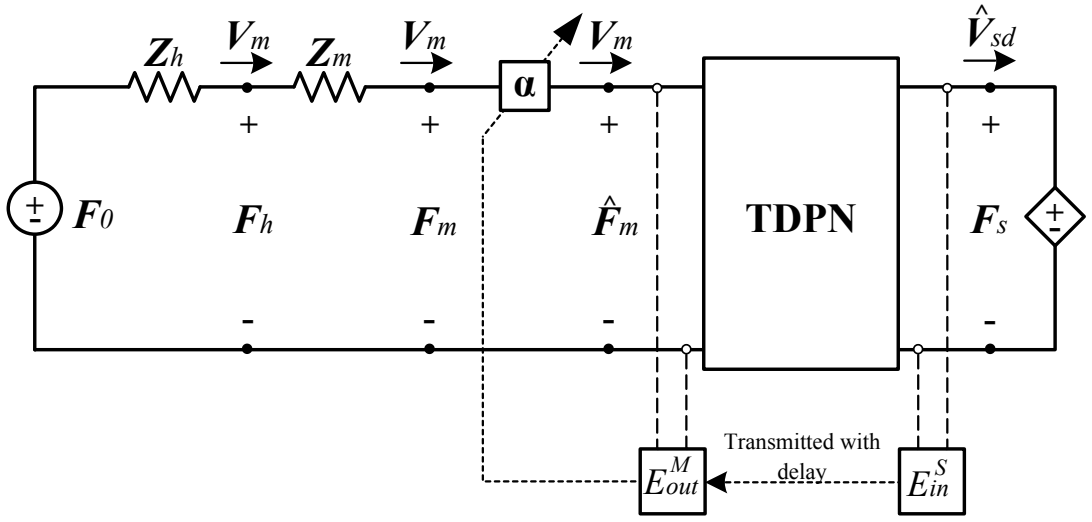

Figure 3.4: Master side of a P-F architecture. The PO-PC ($\boldsymbol{\alpha}$) is applied in impedance configuration.

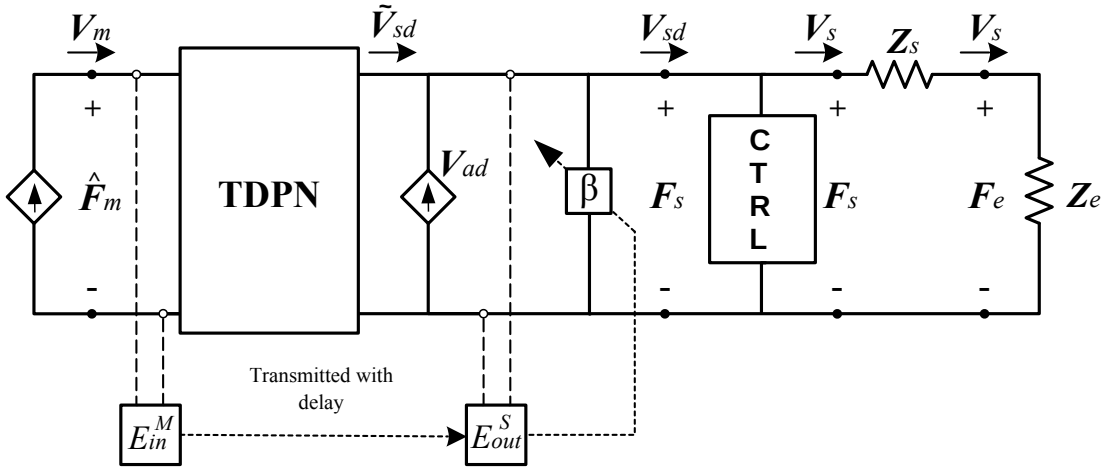

Figure 3.5: Slave side of a P-F architecture. The PO-PC ($\boldsymbol{\beta}$) is applied in admittance configuration. $\boldsymbol{V}_{ad}$ is the drift compensator velocity.

of the TDPN is computed as

$$W_M(k) = E^S_{in}(k - T_b(k)) - E^M_{out}(k) + E^M_{PC}(k-1), \tag{3.11}$$

$$W_S(k) = E^M_{in}(k - T_f(k)) - E^S_{out}(k) + E^S_{PC}(k-1). \tag{3.12}$$

These computations are performed by the so-called passivity observers (PO) and provided to the passivity controllers.

3.3.3 Passivity Controller

The passivity controller acts as an adaptive damping in order to guarantee the passivity of the channel. It can be applied in impedance or admittance configuration,

according to the architecture requirements. In Fig. 3.4 the PC is being applied in impedance configuration in order to modify the force coming out of the channel. In Fig. 3.5 it is applied in admittance configuration and modifies the velocity flowing out of the channel.

In order to fulfill the passivity conditions from (3.9) and (3.10) for the Cartesian-space task, two constructions for the passivity controller are possible, namely the concatenated and the coupled versions.

Concatenated PO-PC

The concatenated version consists of adding a passivity observer to each degree of freedom ($W_S^i(k)$) and computing $\boldsymbol{\alpha}$ and $\boldsymbol{\beta}$ as diagonal matrices, whose diagonal elements α_i and β_i are given by

$$\alpha^i(k) = \begin{cases} 0 & \text{if } W_M^i(k) > 0 \\ -\dfrac{W_M^i(k)}{\Delta T\, V_m^i(k)^2} & \text{else, if } |V_m^i(k)| > 0\,, \end{cases} \tag{3.13}$$

$$\beta^i(k) = \begin{cases} 0 & \text{if } W_S^i(k) > 0 \\ -\dfrac{W_S^i(k)}{\Delta T\, F_s^i(k)^2} & \text{else, if } |F_s^i(k)| > 0\,, \end{cases} \tag{3.14}$$

where V_m^i and F_s^i are the elements of $\boldsymbol{V}_m$ and $\boldsymbol{F}_m$, respectively, and ΔT is the sampling time. The energy dissipated by each of the master and slave passivity controllers can be computed as

$$E_{PC,i}^M(k) = \sum_{j=1}^{k} \alpha^i(j) V_m^i(j)^2\,, \tag{3.15}$$

$$E_{PC,i}^S(k) = \sum_{j=1}^{k} \beta^i(j) F_s^i(j)^2\,, \tag{3.16}$$

where $||.||$ is the Euclidean norm.

Coupled PO-PC

In addition to the concatenated version, the passivity controller can be applied in a coupled manner. For that purpose, the impedance PC presented by OTT *et al.* [35] can be applied as

$$\boldsymbol{\alpha}(k) = d_x(k) \boldsymbol{\Lambda}_x(\boldsymbol{q}(k))\,, \tag{3.17}$$

$$d_x(k) = \begin{cases} 0 & \text{if } W_M(k) > 0 \\ -\dfrac{W_M(k)}{\Delta T ||\boldsymbol{V}_m(k)||_x^2} & \text{else, if } ||\boldsymbol{V}_m(k)||_x^2 > 0\,, \end{cases} \tag{3.18}$$

where

$$||\boldsymbol{V}_m(k)||_x^2 = \boldsymbol{V}_m(k)^T \boldsymbol{\Lambda}_x(\boldsymbol{q}(k)) \boldsymbol{V}_m(k)\,. \tag{3.19}$$

In that case, the energy dissipated by the master PC will be

$$E_{PC}^M(k) = \sum_{j=1}^{k} d_x(j) ||\boldsymbol{V}_m(j)||_x^2\,. \tag{3.20}$$

In addition, the equivalent admittance-type passivity controller would be

$$\boldsymbol{\beta}(k) = d_f(k) \boldsymbol{\Lambda}_x(\boldsymbol{q}(k))^{-1}\,, \tag{3.21}$$

$$d_f(k) = \begin{cases} 0 & \text{if } W_S(k) > 0 \\ -\dfrac{W_S(k)}{\Delta T ||\boldsymbol{F}_s(k)||_f^2} & \text{else, if } ||\boldsymbol{F}_s(k)||_f^2 > 0\,, \end{cases} \tag{3.22}$$

where

$$||\boldsymbol{F}_s(k)||_f^2 = \boldsymbol{F}_s(k)^T \boldsymbol{\Lambda}_x(\boldsymbol{q}(k))^{-1} \boldsymbol{F}_s(k)\,. \tag{3.23}$$

and the energy dissipated by the slave PC will be

$$E_{PC}^S(k) = \sum_{j=1}^{k} d_f(j) ||\boldsymbol{F}_s(j)||_f^2\,. \tag{3.24}$$

For both, concatenated and coupled constructions, the force removed by the impedance-type passivity controller from the delayed slave force in order to keep the system passive will be

$$\boldsymbol{F}_{pc}(k) = \boldsymbol{\alpha}(k) \boldsymbol{V}_m(k)\,, \tag{3.25}$$

the resulting force applied on the master device will be

$$\boldsymbol{F}_m(k) = \hat{\boldsymbol{F}}_m(k) - \boldsymbol{F}_{pc}(k)\,. \tag{3.26}$$

Accordingly, the velocity removed by the admittance PC from the delayed master velocity can be computed as

$$\boldsymbol{V}_{pc}(k) = \boldsymbol{\beta}(k) \boldsymbol{F}_s(k)\,, \tag{3.27}$$

and the resulting velocity used as a reference by the slave will be

$$\boldsymbol{V}_{sd}(k) = \tilde{\boldsymbol{V}}_{sd}(k) - \boldsymbol{V}_{pc}(k)\,. \tag{3.28}$$

It is also important to remark that, for the 1-DoF case, the concatenated and the coupled PO-PC constructions are equivalent. The reader is referred to PANZIRSCH *et al.* [18] for further insights about the multi-DoF implementation of TDPA.

3.4 1-DoF Drift Compensator

This Section presents a novel drift-compensation method, which can be applied to 1-DoF teleoperation devices. Its advantages relative to the previously presented approaches [25, 26] are also discussed.

3.4.1 Cause of Position Drift and Its Definition on $\mathbb{R}$

From Fig. 3.5 and Eq. 3.28 it can be noted that, when the admittance type PC is activated on the slave side, the velocity signal coming from the master is reduced. At these moments the reference to the slave controller ($\boldsymbol{V}_{sd}$) differs from the untouched velocity signal coming from the master ($\tilde{\boldsymbol{V}}_{sd}$). As soon as the PC becomes inactive, $\boldsymbol{V}_{sd}$ assumes the same value as $\tilde{\boldsymbol{V}}_{sd}$ and the velocities can be synchronized. The problem, however, arises when, in addition to velocity, position synchronization is desired, which is the case for many teleoperation applications. Position signals are usually not transmitted through the channel due to limited bandwidth. In order to obtain information about the position of the master, the velocity signal has to be integrated on the slave side. However, in order to keep the system passive the velocity signal used on the slave side is $\boldsymbol{V}_{sd}$. For the case where $\boldsymbol{V}_{sd} \in \mathbb{R}$, the position command from the master can be obtained as

$$\boldsymbol{x}_{sd} = \Delta T \sum_{j=1}^{k} \boldsymbol{V}_{sd}(j). \tag{3.29}$$

The correspondence between $\boldsymbol{x}_{sd}$ and the actual delayed master device's position, $\tilde{\boldsymbol{x}}_{sd}$, is compromised as soon as the PC becomes active for the first time, and the error between them is accumulated whenever the PC modifies the velocity signal. This error remains even when the PC is not active, due to the accumulating characteristic of the integral. The drift between delayed master position and slave reference

position in $\mathbb{R}$ can be defined as

$$\boldsymbol{x}_{err}(k) = \Delta T \sum_{j=1}^{k} \big(\tilde{\boldsymbol{V}}_{sd}(j) - \boldsymbol{V}_{sd}(j)\big). \tag{3.30}$$

By substituting (3.27) and (3.28) into (3.30) we get

$$\boldsymbol{x}_{err}(k) = \Delta T \sum_{j=1}^{k} \boldsymbol{\beta}(j)\boldsymbol{F}_s(j). \tag{3.31}$$

From (3.31) it can be noted that $\boldsymbol{x}_{err}$ is the integral of the velocity removed by the PC at all time steps.

3.4.2 Origin of Force Spikes in Other Compensators

Up to now, two 1-DoF compensators have been developed in order to eliminate the position drift in energy-based TDPA without decreasing the transparency of the task. ARTIGAS *et al.* [25] suggested modification to the classical PO-PC formulation in order to add extra energy whenever there is a positive gap between the delayed energy flowing into the channel on the master side and the energy flowing out of the channel on the slave side. An algorithm was proposed to keep track of the position error shown in (3.30) and to divide it by the sampling period and add it to the velocity coming from the master whenever a passivity gap showed up. By doing that, the error between $\boldsymbol{x}_{sd}$ and $\tilde{\boldsymbol{x}}_{sd}$ is liquidated if sufficient gaps appear.

Based on that idea, CHAWDA *et al.* [26] proposed an approach to keep the classical PO-PC formulation and have the drift compensation part as an ideal current source between the TDPN and the PC, as shown in Fig. 3.5. In this approach, the current source represented by $\boldsymbol{V}_{ad}$ is responsible for adding the correction to eliminate $\boldsymbol{x}_{err}$, and the classical PC checks the signal composed of $\tilde{\boldsymbol{V}}_{sd} + \boldsymbol{V}_{ad}$ in order to dissipate the active energy coming from both the TDPN and the current source.

Despite the different construction, both methods are equivalent and are usually able to eliminate position drift caused by the PC. However, as mentioned in [26], this way of compensating drift generates undesirable force spikes during the teleoperation task. These abrupt forces not only affect the natural feeling of teleoperation, but can also be harmful to the hardware and the human operator.

The root cause of these forces is that the pair, drift compensator and PC, works as an accumulator. During the periods when the PC is active the drift compensator tries to compensate the drift by adding extra velocity. However, until a passivity gap appears, the drift is accumulating and so is the contribution added by the compensator. The correction is usually allowed when changing the direction of

motion or releasing a wall. At these moments, the accumulated velocity signal is added at one time step and an impulse-like signal is given as reference to the slave, adding a force spike to the controller command.

3.4.3 1-DoF Drift Compensator

In order to compensate position drift in a smoother manner, a new approach was developed. The proposed approach is based on the same architecture as presented in [26] (see Fig. 3.5). However, a different expression for the velocity source ($\boldsymbol{V}_{ad}$) was developed. The velocity added by the proposed compensator is given as

$$\boldsymbol{V}_{ad}(k) = K \sum_{j=0}^{k-1} \big(\tilde{\boldsymbol{V}}_{sd}(j) - \boldsymbol{V}_{s}(j) \big). \tag{3.32}$$

From (3.32) and Fig. 3.5 it can be seen that whenever there is an error between the delayed master position and the one modified by the PC, the compensator adds a velocity signal to the untouched velocity coming from the master, which is checked by the PO for passivity. As in [26] the PC is responsible for dissipating the extra energy generated by the TDPN or the drift compensator in order to enforce passivity. The gain K from (3.32) can be appropriately tuned in order to obtain the desired performance. Values of K approaching 1 increase the compensation signal and decrease the number of time steps necessary to remove all drift. Lower values of K yield lower $\boldsymbol{V}_{ad}$, which compensates the drift in a smoother manner over a larger number of time steps.

The presented formulation allows for passive teleoperation while providing position synchronization and keeping the forces in their normal range. This is a desired characteristic since force spikes are not always allowed in teleoperation tasks. In cases where the workspace of the teleoperated robot is limited, if the abrupt forces act towards the limits of the workspace, hardware damages could happen. Another field where the force spikes would not be allowed is human-robot collaboration (e.g. robotic-assisted surgery), where the abrupt forces would pose a risk to humans. On the other hand, as will be shown in the experimental evaluation, the use of regular TDPA without drift compensation also prevents the successful completion of the tasks since the position drift can get to a point where the slave barely responds to the master's commands. The proposed approach is able to provide position synchronization and forces with regular amplitudes, making it possible to successfully complete teleoperation tasks without putting humans and hardware at risk.

As in [26], the passivity of this drift compensator is enforced by the PC, which is implemented after the compensator. If the overall system is passive without time delays, then it is also passive when the TDPN and the PO-PC pair are introduced.

3.5 Multi-DoF Drift Compensator

Although previously presented TDPA-based methods provided a way of reducing drift in teleoperation tasks, their Multi-DoF extension was not provided. In that scope, this Section provides a Multi-DoF drift-compensation approach, which according to the tuning parameters, can be seen as an extension of the previously presented approaches [25, 26] or the one presented in Section 3.4.

3.5.1 Representation of Drift on $SE(3)$

Assuming the teleoperation task comprises the complete Cartesian space, the velocities $\tilde{\boldsymbol{V}}_{sd}(k)$ and $\boldsymbol{V}_{sd}(k)$ can be defined to be *body velocities* [29] in $\mathbb{R}^6$ as

$$^{\hat{\mathcal{D}}}\tilde{\boldsymbol{V}}_{sd}(k) = \begin{bmatrix} \omega_{\tilde{\mathcal{D}}} \\ \boldsymbol{v}_{\tilde{\mathcal{D}}} \end{bmatrix}, \quad ^{\mathcal{D}}\boldsymbol{V}_{sd}(k) = \begin{bmatrix} \omega_{\mathcal{D}} \\ \boldsymbol{v}_{\mathcal{D}} \end{bmatrix}, \tag{3.33}$$

where $\tilde{\mathcal{D}}$ and $\mathcal{D}$ are the frames defined by the delayed master orientation and the orientation given to the slave as the reference, respectively. The discrete-time integral of $^{\hat{\mathcal{D}}}\tilde{\boldsymbol{V}}_{sd}$ and $^{\mathcal{D}}\boldsymbol{V}_{sd}$ can be computed following (2.23) as

$$\boldsymbol{g}_{\mathcal{D}}(k) = \boldsymbol{g}_{\mathcal{D}}(k-1)\exp_{\mathrm{SE(3)}}\left([^{\mathcal{D}}\boldsymbol{V}_{sd}(k)]^{\wedge}\Delta T\right), \tag{3.34}$$

$$\boldsymbol{g}_{\tilde{\mathcal{D}}}(k) = \boldsymbol{g}_{\tilde{\mathcal{D}}}(k-1)\exp_{\mathrm{SE(3)}}\left([^{\hat{\mathcal{D}}}\tilde{\boldsymbol{V}}_{sd}(k)]^{\wedge}\Delta T\right), \tag{3.35}$$

Using the definitions above, the drift present in the system at a given time step (k) can be represented in $SE(3)$ by

$$\boldsymbol{g}_E(k) = \boldsymbol{g}_{\tilde{\mathcal{D}}}(k)^{-1}\boldsymbol{g}_{\mathcal{D}}(k) = \begin{bmatrix} \boldsymbol{R}_E(k) & \boldsymbol{p}_E(k) \\ \boldsymbol{0} & 1 \end{bmatrix}. \tag{3.36}$$

It can be noted from (3.28) and (3.34)–(3.36) that, if the PC acts at a time step, it will affect the value of $\boldsymbol{g}_E$ for all future time steps. In case $\boldsymbol{g}_E$ is not the identity matrix, there will be a drift between the delayed master pose and the pose given as reference to the slave.

3.5.2 Cartesian-Space Drift Compensation

In order to compensate for the drift caused by TDPA, an additional velocity signal $\boldsymbol{V}_{ad}$ can be added to the delayed master velocity before it is checked by the PO. In Fig. 3.5 the drift compensator is represented by a current source. It can be noted that, since $\boldsymbol{V}_{ad}$ is applied before the point where the energies are computed, the modified velocity $\tilde{\boldsymbol{V}}_{sd}(k) + \boldsymbol{V}_{ad}(k)$ will be checked and corrected for passivity.

This guarantees that the compensation action will only be applied when so-called "passivity gaps" appear, i.e., when $W_S(k)$ from (3.12) would be greater than zero. Therefore, the compensator would not compromise the passivity of the system. From Fig. 3.5, it can been seen that, when the drift compensator is added, (3.28) becomes

$$\mathrm{Ad}_{\boldsymbol{g_e}}(k)\ {}^{\mathcal{D}}\boldsymbol{V}_{sd}(k) = {}^{\hat{\mathcal{D}}}\tilde{\boldsymbol{V}}_{sd}(k) + {}^{\hat{\mathcal{D}}}\boldsymbol{V}_{ad}(k) - {}^{\hat{\mathcal{D}}}\boldsymbol{V}_{pc}(k)\,, \tag{3.37}$$

where $\mathrm{Ad}_{\boldsymbol{g_e}}(k)$ (see Section 2.2.4) is defined as

$$\mathrm{Ad}_{\boldsymbol{g_e}}(k) = \begin{bmatrix} \boldsymbol{R}_E(k) & \boldsymbol{0} \\ \widehat{\boldsymbol{p}}_E(k)\boldsymbol{R}_E(k) & \boldsymbol{R}_E(k) \end{bmatrix}. \tag{3.38}$$

In order to reduce the drift between master and slave devices whenever allowed by the aforementioned passivity conditions, the following law can be used

$$\begin{aligned} \omega_{ad}(k) &= -\frac{1}{\Delta T}\boldsymbol{k_R}\,\varphi_E(k-1)\,, \\ \boldsymbol{v}_{ad}(k) &= -\frac{1}{\Delta T}\boldsymbol{A}\left(\omega_{ad}(k)\Delta T\right)^{-T}\boldsymbol{K_T}\,\boldsymbol{p}_E(k-1)\,, \end{aligned} \tag{3.39}$$

$${}^{\hat{\mathcal{D}}}\boldsymbol{V}_{ad}(k) = \begin{bmatrix} \omega_{ad}(k) \\ \boldsymbol{v}_{ad}(k) \end{bmatrix}, \tag{3.40}$$

where $\widehat{\varphi}_E(k-1) = \log_{SO(3)}\left(\boldsymbol{R}_E(k-1)\right)$, and $\boldsymbol{K_T} \in \mathbb{R}^{3\times3}$ and $\boldsymbol{k_R} \in \mathbb{R}$ are the translational and rotational gains of the compensator. Moreover, $\boldsymbol{A}^{-T}$ is defined in Section 2.2.3.

3.5.3 Convergence Analysis

As mentioned in Section 3.5.1, in order to keep passivity, the proposed compensator is only able to reduce the drift when energy gaps are present. During the moments when the passivity controller is acting to reduce the delayed master velocity coming from the channel, the accumulation of drift is unavoidable. For that reason, this section aims to analyze the convergence characteristics of the compensator during the moments where it is allowed to act.

At the moments where the compensation action is allowed, (3.37) becomes

$$\mathrm{Ad}_{\boldsymbol{g_e}}(k)\ {}^{\mathcal{D}}\boldsymbol{V}_{sd}(k) = {}^{\hat{\mathcal{D}}}\tilde{\boldsymbol{V}}_{sd}(k) + {}^{\hat{\mathcal{D}}}\boldsymbol{V}_{ad}(k)\,. \tag{3.41}$$

By defining a velocity error $\boldsymbol{V}_E(k)$, (3.41) becomes

$${}^{\hat{\mathcal{D}}}\boldsymbol{V}_E(k) \triangleq \mathrm{Ad}_{\boldsymbol{g_e}}(k)\ {}^{\mathcal{D}}\boldsymbol{V}_{sd}(k) - {}^{\hat{\mathcal{D}}}\tilde{\boldsymbol{V}}_{sd}(k) = {}^{\hat{\mathcal{D}}}\boldsymbol{V}_{ad}(k)\,. \tag{3.42}$$

From this definition, the error pose $\boldsymbol{g}_E(k)$ can be defined as in (2.22) with ${}^{\hat{\mathcal{D}}}\boldsymbol{V}_E(k)$ as its spatial velocity as follows

$$\boldsymbol{g}_E(k) = \exp_{\mathrm{SE}(3)}\big([{}^{\hat{\mathcal{D}}}\boldsymbol{V}_E(k)]^{\wedge}\Delta T\big)\boldsymbol{g}_E(k-1)\,. \tag{3.43}$$

By exploring the equality between ${}^{\hat{\mathcal{D}}}\boldsymbol{V}_E(k)$ and ${}^{\hat{\mathcal{D}}}\boldsymbol{V}_{ad}(k)$ defined in (3.42), the error pose from (3.43) becomes

$$\boldsymbol{g}_E(k) = \exp_{\mathrm{SE}(3)}\big([{}^{\hat{\mathcal{D}}}\boldsymbol{V}_{ad}(k)]^{\wedge}\Delta T\big)\boldsymbol{g}_E(k-1)\,. \tag{3.44}$$

It follows from the compensation law (3.39) and the definition of the exponential function in $SE(3)$ (2.8) that the rotational part of (3.43) becomes

$$\boldsymbol{R}_E(k) = \exp_{\mathrm{SO}(3)}\left(-\boldsymbol{k}_{\boldsymbol{R}}\,\widehat{\varphi}_E(k-1)\right)\boldsymbol{R}_E(k-1)\,, \tag{3.45}$$

which results in the following relation

$$\varphi_E(k) = (1-\boldsymbol{k}_{\boldsymbol{R}})\varphi_E(k-1)\,. \tag{3.46}$$

Likewise, the translational part becomes

$$\begin{aligned}\boldsymbol{p}_E(k) = {}& \exp_{\mathrm{SO}(3)}\left(\widehat{\omega}_{ad}(k)\Delta T\right)\boldsymbol{p}_E(k-1)\\ & -\boldsymbol{A}\left(\omega_{ad}(k)\Delta T\right)\,\boldsymbol{A}\left(\omega_{ad}(k)\Delta T\right)^{-T}\boldsymbol{K}_{\boldsymbol{T}}\,\boldsymbol{p}_E(k-1)\;.\end{aligned} \tag{3.47}$$

By using the identity from (2.13), (3.47) becomes

$$\boldsymbol{p}_E(k) = \exp_{\mathrm{SO}(3)}\left(\widehat{\omega}_{ad}(k)\Delta T\right)\left(\mathbf{I}-\boldsymbol{K}_{\boldsymbol{T}}\right)\,\boldsymbol{p}_E(k-1)\;. \tag{3.48}$$

It can be verified that a sufficient condition for convergence is

$$0 <\; \boldsymbol{k}_{\boldsymbol{R}} \;< 2 \quad \wedge \quad 0 <\; \mathrm{eig}(\boldsymbol{K}_{\boldsymbol{T}}) \;< 2\,, \tag{3.49}$$

which ensures that

$$||\varphi_E(k)|| < ||\varphi_E(k-1)||\,, \tag{3.50}$$

$$||\boldsymbol{p}_E(k)|| < ||\boldsymbol{p}_E(k-1)||\,, \tag{3.51}$$

as long as the trace of the accumulated rotational error $\boldsymbol{R}_E$ is not equal to one when the compensator is allowed to act after the drift has been accumulated by the passivity controller. The above presented compensation law makes sure that the magnitude of the drift is decreased from one time step to the next, even if the compensator is only allowed to act during a short period of time. Moreover,

if the passivity controller allows the compensator to act for an infinite number of consecutive time steps, convergence of $\boldsymbol{g}_E$ is ensured (see Lemma 2.4.1.).

It is also interesting to note that, if the gain matrices are chosen to be identity matrices, the drift converges within one time step. This can be seen as the multi-DoF extension of the compensators proposed in [25] and [26]. However, in case the force peaks described in [26] are undesirable, other values within the convergent range could be chosen. In that case, the proposed compensator can be considered as an extension of the one presented in Section 3.4.

Another important observation is that the proposed compensator looks similar to the kinematic regulator shown in Section 2.4.2. However, two differences can be noted. First, a spatial-velocity representation is chosen for the drift. This is due to the fact that, since the compensator is applied before the passivity controller, it is easier to work with velocities in the $\tilde{\mathcal{D}}$ frame. The spatial-velocity regulator is also showed by BULLO and MURRAY [28]. Nevertheless, the substantial difference comes from the discrete-time nature of the problem being solved. It has also been considered meaningful to add the term $\boldsymbol{A}\left(\omega_{ad}(k)\Delta T\right)^{-T}$ in order to achieve independent speed of convergence of the translational term from the rotational one, which is suitable for the case when slow rotational- and fast translational-drift compensation is desired.

3.6 Experimental Evaluation

This section provides both experimental evaluation of the proposed drift compensator. Section 3.6.1 presents the results of experiments performed using two 1-DoF rotational devices, which aimed at comparing the proposed approach with one of the previously presented approaches [26]. Section 3.6.1 presents the results of experiments performed using two 3-DoF translational devices. In that section, the concatenated PO-PC construction (see Section 3.3.3) alone and with the proposed Multi-DoF compensator is evaluated. The results of the application of the proposed drift compensator to the complete 6-DoF Cartesian Space of an Aerial Manipulator will be shown in Chapter 5.

3.6.1 1-DoF Implementation

Initial experiments were performed using two 1-DoF rotational devices (see Fig. 3.6) composed of two independent motor-gear units, each of them equipped with a torque sensor. The devices were controlled using the same computer, which was running at a sampling rate of 1 kHz. The devices were connected through a position-force architecture and communication delay was simulated in software. The logic was

implemented using a mix of block diagram and *MATLAB* code in *Simulink*. Low-level code was automatically generated and embedded onto an on-board computer, which ran at 1 kHz.

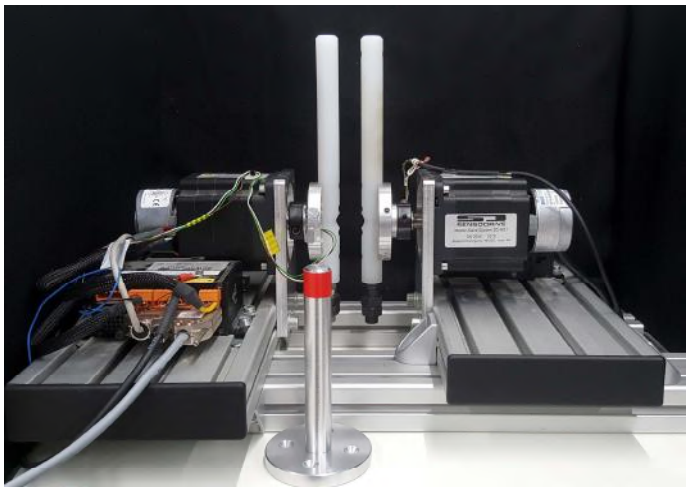

Figure 3.6: 1-DoF teleoperation setup used for the experiments.

The experiments were conducted with regular TDPA, the compensator proposed by CHAWDA *et al.* [26], and the proposed 1-DoF compensator with a gain K of 0.0025. The approach from ARTIGAS *et al.* [25] is not tested here since its results are similar to the ones from CHAWDA *et al.* [26], despite having different construction.

Each approach was tested for round-trip delays ($T_{rt} = T_f + T_b$) of 100 ms, 200 ms, and 500 ms. The human operator attempted to simulate a sinusoidal reference in position while the slave device performed hard-wall contacts. The wall was located at around 90 degrees ($\approx$ 1.5 rad) of deflection. Teleoperation without TDPA was found to be unstable for all three delays tested and the data is not shown. The figures are divided into four subplots: (a) shows the master and slave positions, (b) shows the control torques acting on the master and the slave, (c) shows the input energy from the slave and the output energy at the master, (d) shows the input energy from the master, the output energy at the slave, and the energy added by the compensators before the PC (E_{ad}), except for the pure TDPA case.

Fig. 3.7 shows hard-wall contacts for pure TDPA without drift compensation for $T_{rt} = 100$ ms. It can be noted that the drift between master and slave accumulates over the wall contacts (Fig. 3.7a). Due to the drift, the wall contacts happen earlier at each time and the operator has to exert higher forces (Fig. 3.7b) in order to follow the sinusoidal reference. The experiments were repeated with the compensator from [26] (Fig. 3.8) and the proposed compensator (Fig. 3.9). Both compensators are able to eliminate the position drift (Figs. 3.8a and 3.9a). However, high torque spikes happen when the compensator from [26] is applied (Fig. 3.8b). These impulse-like torques make the slave device oscillate at its natural frequency, as can be seen in

Fig. 3.8a. Vibrations are much lower when the proposed approach is used (Fig. 3.9a) and the forces are kept within their normal range (Fig. 3.9b). It can also be noted that the energy injected (E_{ad}) by the compensator from [26] (Fig. 3.8d) is much higher than the energy injected in the proposed approach (Fig. 3.9d).

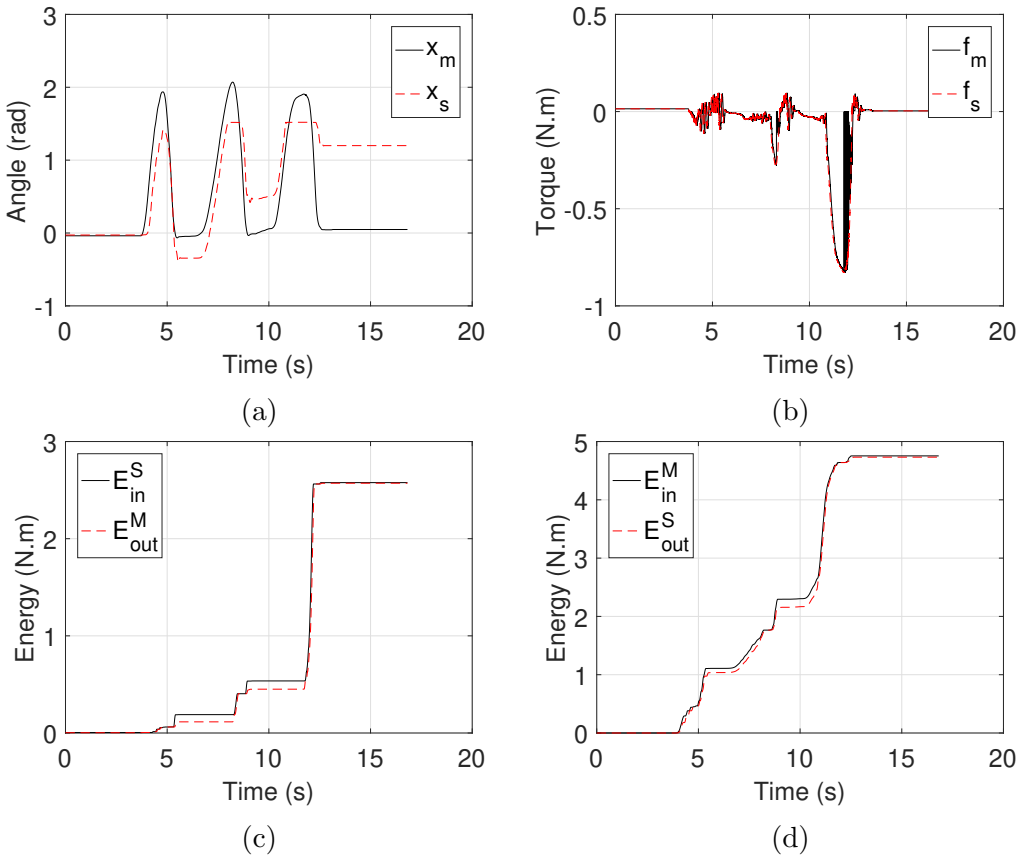

Figure 3.7: $T_{rt} = 100$ ms wall contact – no drift compensator

Figs. 3.10, 3.11, and 3.12 show the results of the experiments for a 200 ms round-trip delay. In Fig. 3.10a it can be seen that in regular TDPA the position offset was increased to a point where the slave barely moved, despite the commands from the master. With the compensator from [26], oscillations on the slave device (Fig. 3.11a) are induced by the torque spikes (Fig. 3.11b) generated when the energy stored by the compensator is released. The energy added (E_{ad}) by the proposed compensator (Fig. 3.12d) is much lower than the energy added by the compensator from [26] (Fig. 3.11d). It can be noted from Fig. 3.12a that the proposed compensator is capable of removing the position drift while causing much smaller oscillations.

The experiments conducted for $T_{rt} = 500$ ms (Figs. 3.13, 3.14, and 3.15) show that both compensators are able to remove the position drift. However, for 500 ms the system tends to become more active due to the low inertia and damping of the devices used. To dissipate the extra energy the PC acts at almost all time steps, which gives both compensators few opportunities to act. Because of that,

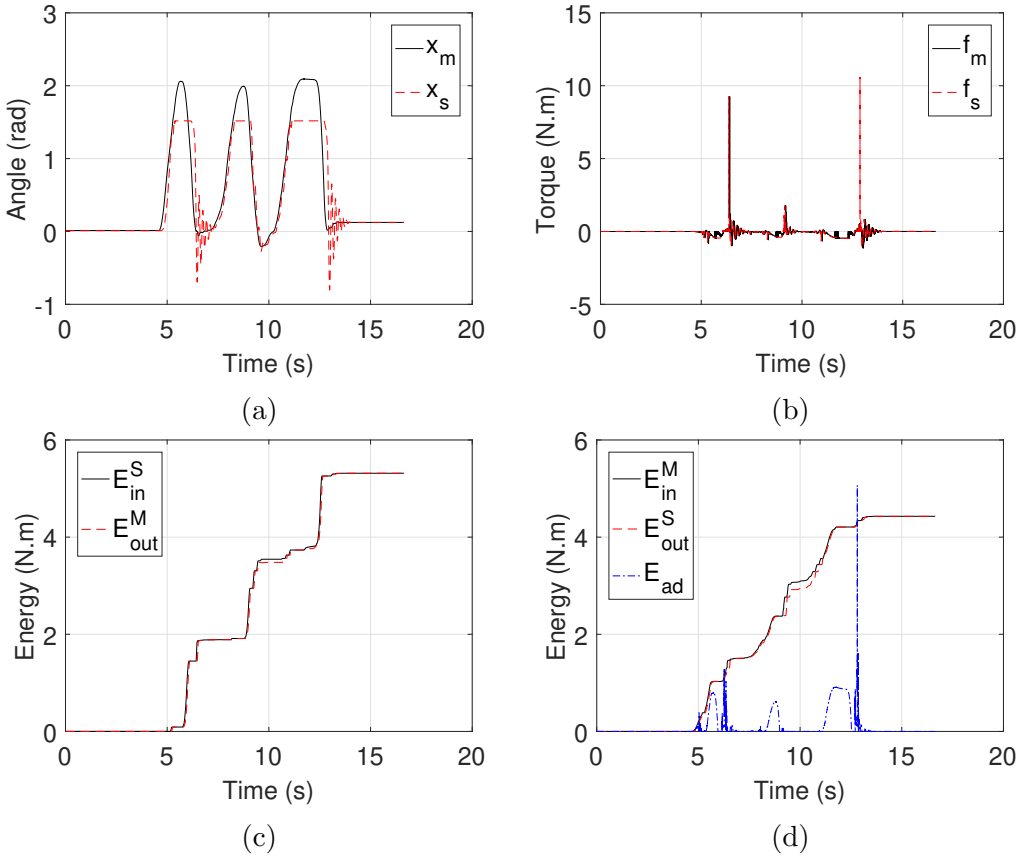

Figure 3.8: $T_{rt} = 100$ ms wall contact – compensator from Chawda et al.

the human operator had to add extra low amplitude movements to the sinusoidal reference in order to create extra passivity gaps (Fig. 3.14a and 3.15a). Note that the value of T_{rt} where passivity gaps start becoming rare depends on the damping and inertia of the device. A larger or more damped device could allow for teleoperation with higher delays without the operator having to care about passivity gaps. Comparing the behavior of both compensators, it can be noted that, even though some torque spikes also start to become present in the proposed approach due to drift accumulation (Fig. 3.15b), these are still close to the range of the normal teleoperation torques. On the other hand, the compensator from [26] presents higher torques (Fig. 3.14b), which are much more perceptible and could be even dangerous to the human operator.

The fact that force spikes generated by the method described in [26] are not significant in the proposed approach is due to the addition of the gain K, which spreads the compensation action over a number of time steps, instead of trying to compensate for the drift at once. Moreover, adding a gain K to the compensator equation makes this approach more versatile to different tasks since the gain could be increased or decreased according to the nature of the task in order to obtain faster or smoother corrections.

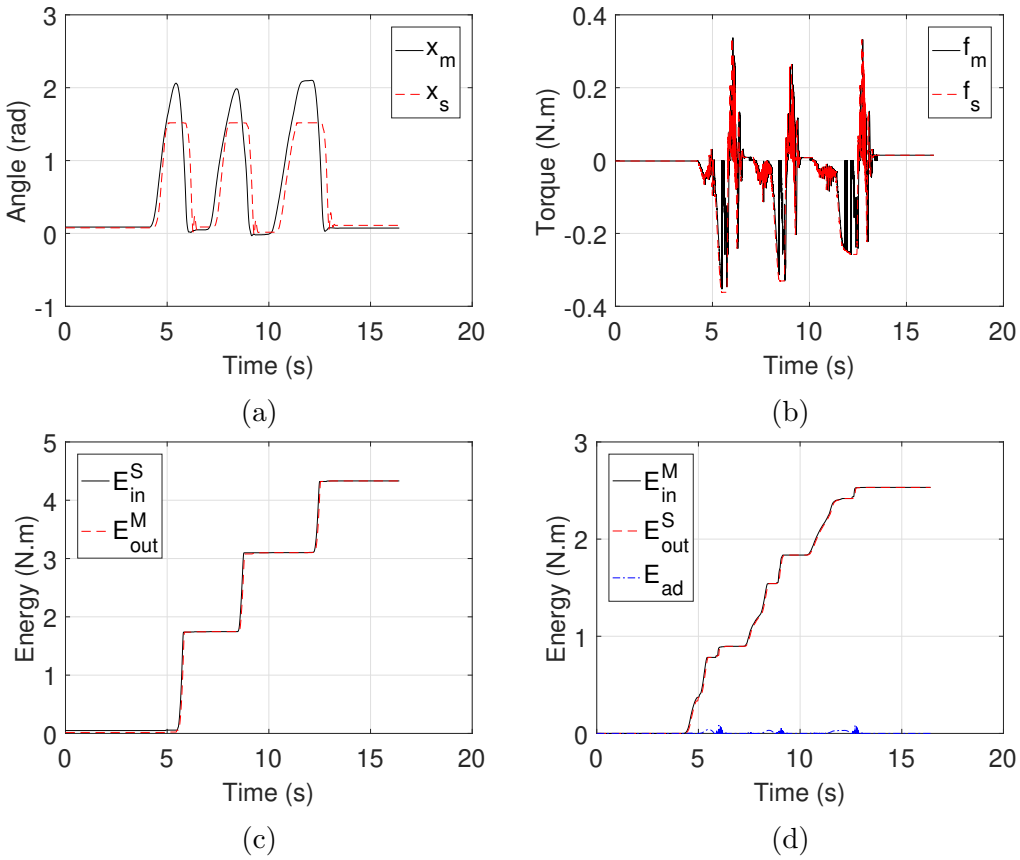

Figure 3.9: $T_{rt} = 100$ ms wall contact – proposed compensator

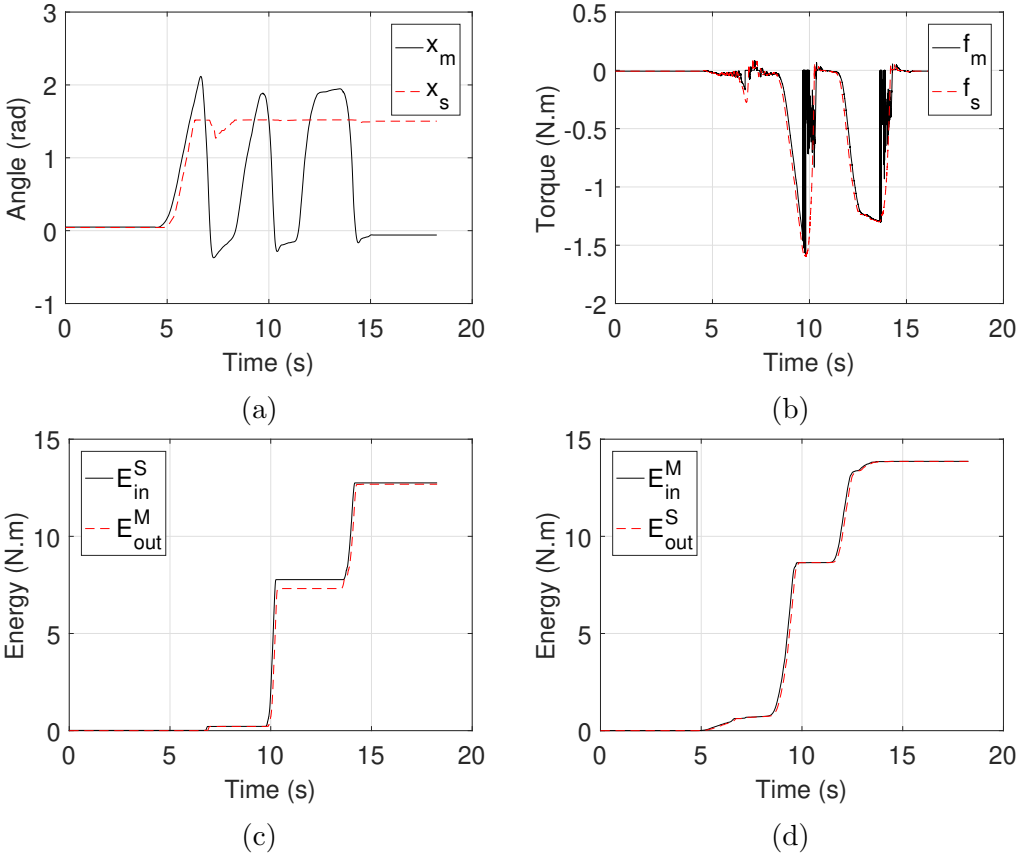

Figure 3.10: $T_{rt} = 200$ ms wall contact – no drift compensator

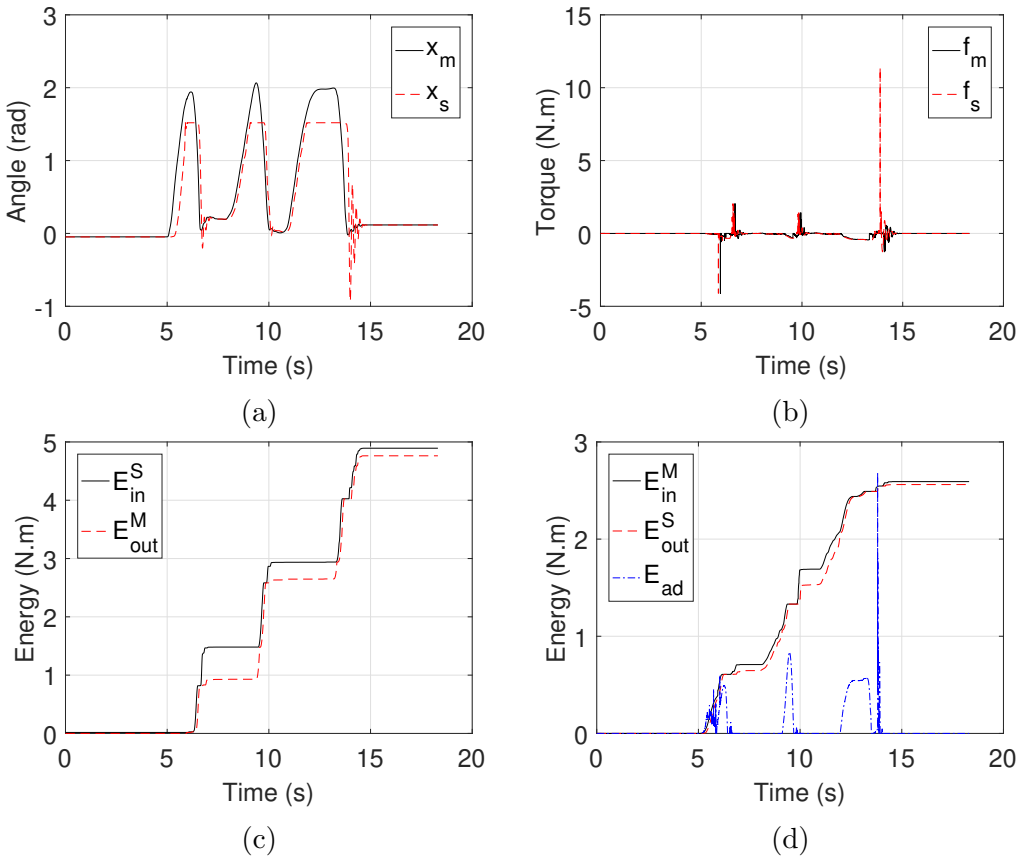

Figure 3.11: $T_{rt} = 200$ ms wall contact – compensator from Chawda et al.

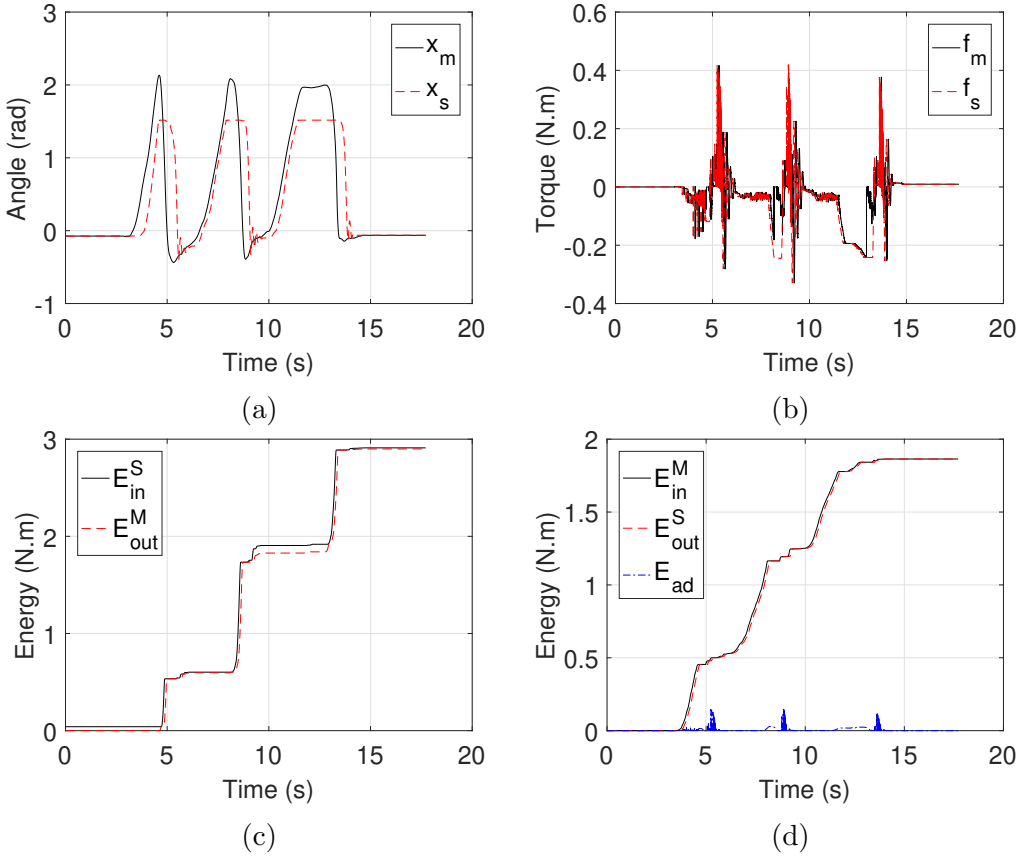

Figure 3.12: $T_{rt} = 200$ ms wall contact – proposed compensator

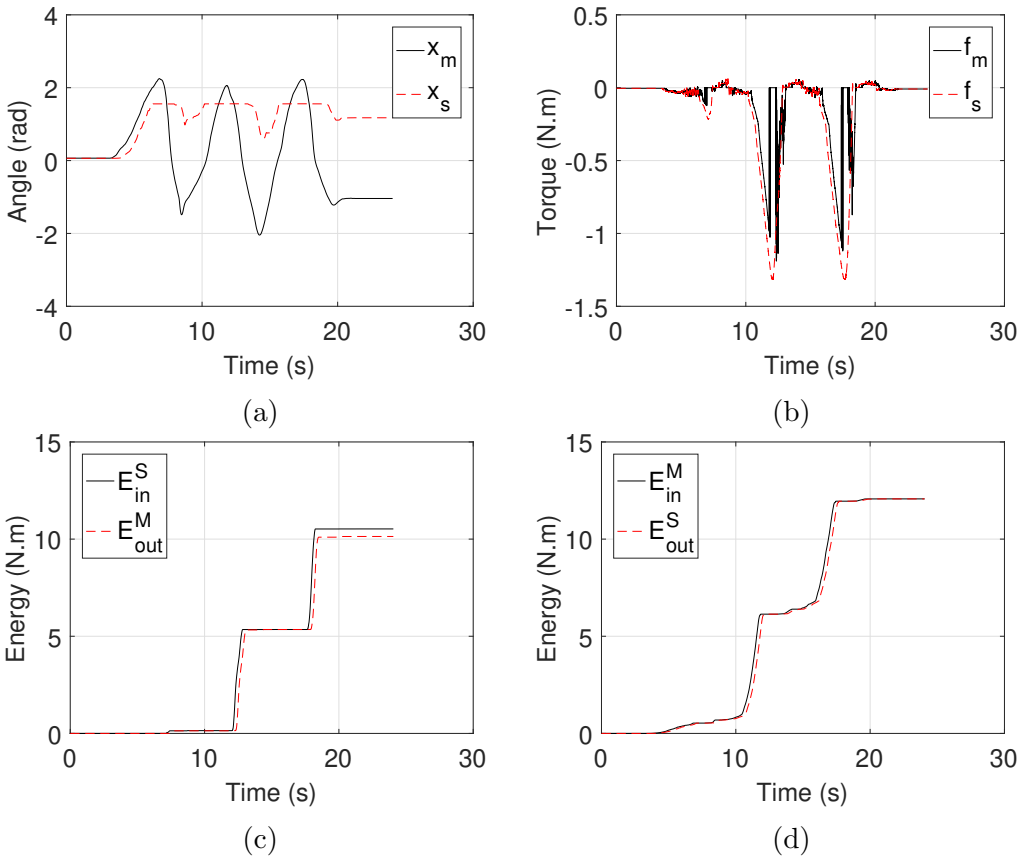

Figure 3.13: $T_{rt} = 500$ ms wall contact – no drift compensator

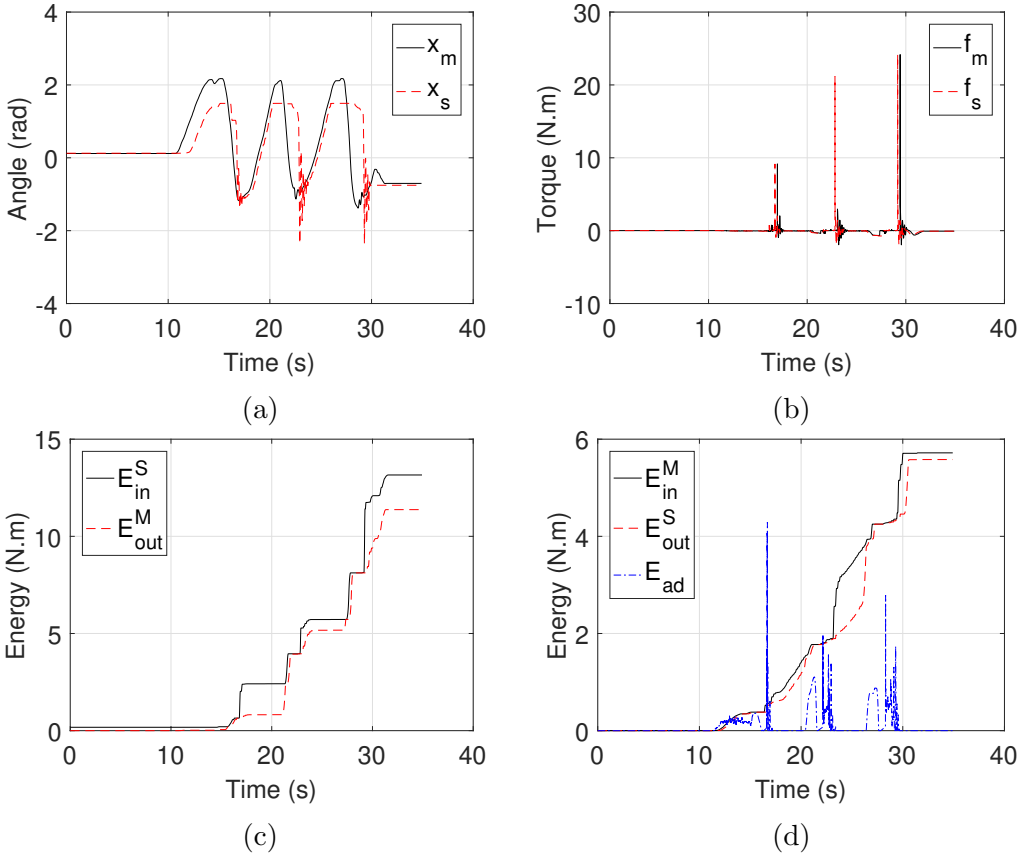

Figure 3.14: $T_{rt} = 500$ ms wall contact – compensator from Chawda et al.

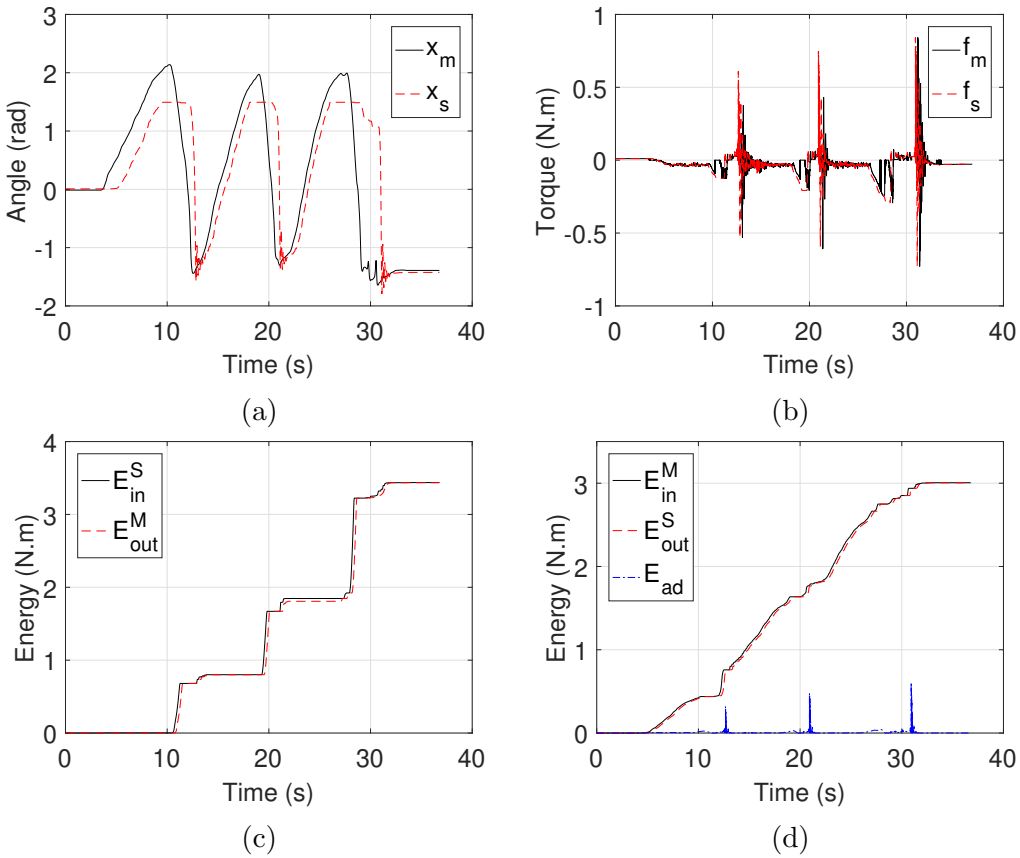

Figure 3.15: $T_{rt} = 500$ ms wall contact – proposed compensator

Figure 3.16: 3-DoF teleoperation device used in experiments.

3.6.2 3-DoF Implementation

In order to validate the proposed compensator on multi-DoF devices, telemanipulation experiments were performed using two 3-DoF translational haptic devices (Fig. 3.16). Firstly, the concatenated PO-PC alone was applied to passivate the communication channel set to artificially add 200 ms round-trip time delays (T_{rt}). Subsequently, the translational part of the proposed compensation law (see (3.39)) was applied. The logic was implemented using C code and embedded onto an on-board computer, which ran at 1 kHz.

Figs. 3.17 and 3.18 show position and control forces, respectively, of the master and slave devices for the non-compensated case. Fig. 3.19 shows the master-input and slave-output energies observed on the slave side. It can be seen that, in order to ensure passivity of the channel, not only the impedance-type PC, intermittently reduced the force values (Fig. 3.18), but also the admittance-type PC removed part of the velocity coming from the master, generating significant drift (see Fig. 3.17).

Figs. 3.20–3.22 show position, force, and energy values, respectively, for the case when the proposed drift compensator was applied. It can be seen that the compensator was able to completely remove the drift in the y- and z-axes (Fig. 3.20). However, an offset can still be observed in the x-axis. This is due to the fact that not enough passivity gaps appeared in order to compensate for the drift in a passive way. The occurrence of passivity gaps depends on the system dynamics, the task being performed and the delay of the channel.

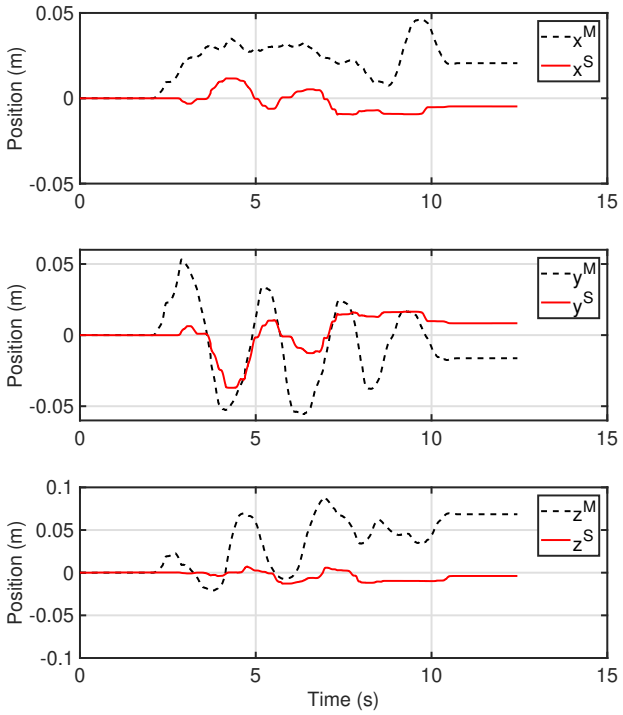

Figure 3.17: Master and slave positions, no drift compensator – $T_{rt} = 200$ ms.

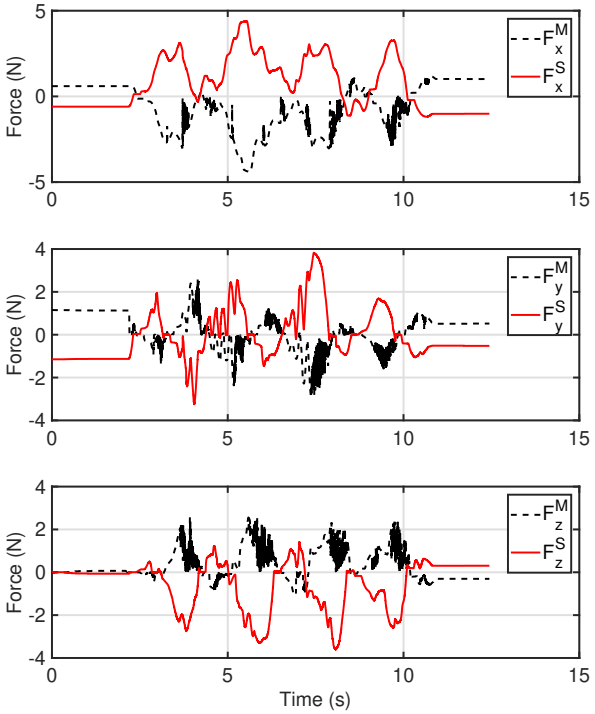

Figure 3.18: Master and slave forces, no drift compensator – $T_{rt} = 200$ ms.

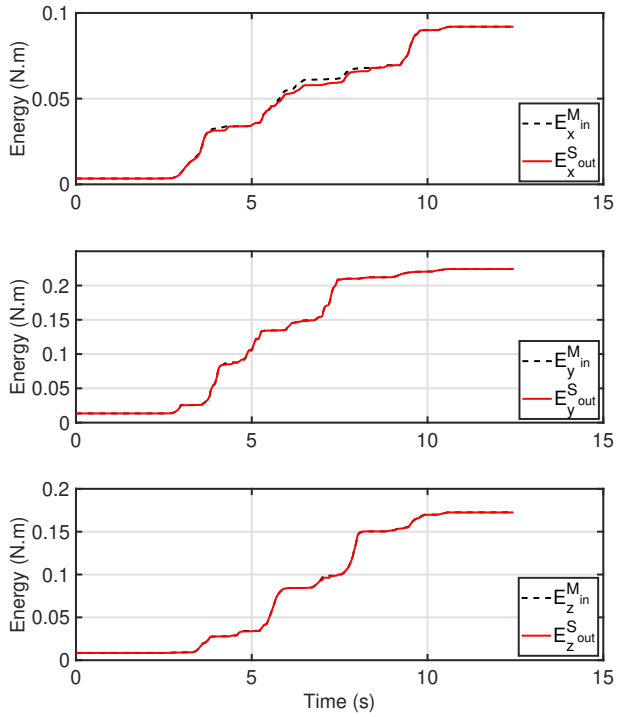

Figure 3.19: Master-in and slave-out energies, no drift compensator – $T_{rt} = 200$ ms.

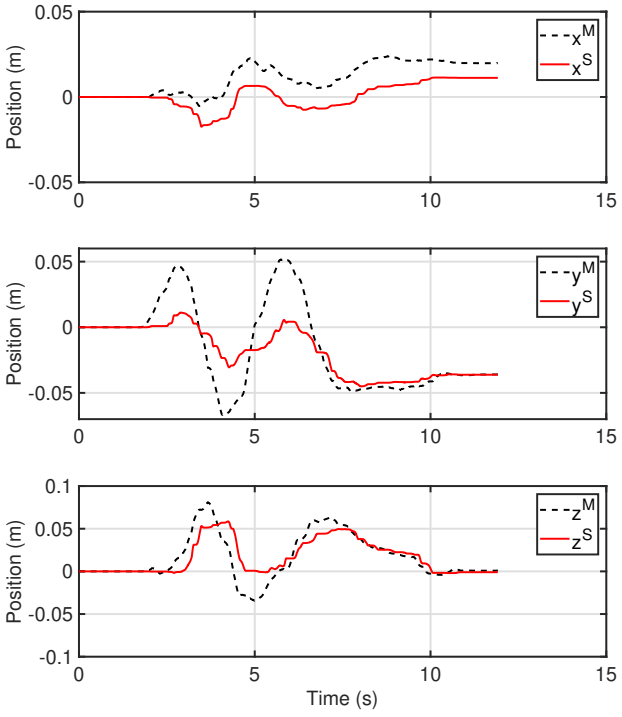

Figure 3.20: Master and slave positions, drift compensator on – $T_{rt} = 200$ ms.

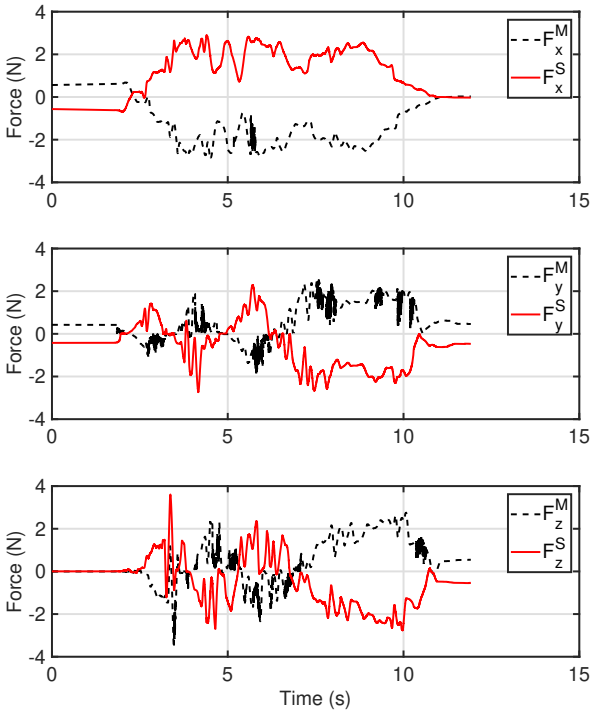

Figure 3.21: Master and slave forces, drift compensator on – $T_{rt} = 200$ ms.

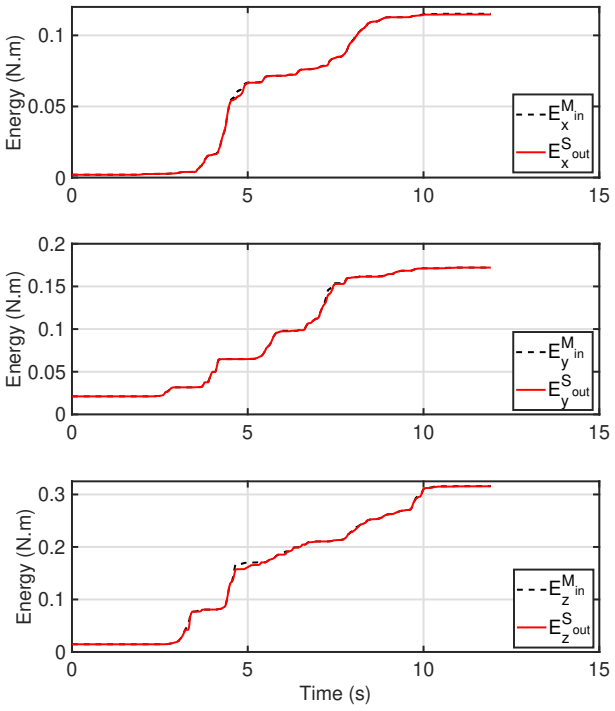

Figure 3.22: Master-in and slave-out energies, drift compensator on – $T_{rt} = 200$ ms.

3.6.3 6-DoF Implementation

In addition to 3-DoF translational devices, the proposed compensator was evaluated with full six-dimensional Cartesian-space teleoperation using the DLR Bimanual Haptic Device (HUG, [36]), which is depicted in Fig 3.23. The device is composed of two torque-controlled 7-DoF LWR manipulators. In the conducted experiments one of the devices was used as a master device and the other, as the slave. Artificial round-trip time delay of 800 ms was added between the two devices (400 ms in each direction). The devices were connected in a P-F architecture (see Fig. 3.1) and the coupled TDPA scheme (see Section 3.3.3) was applied in order to enforce passivity. The logic was implemented using a mix of block diagram and *MATLAB* code in *Simulink*. Low-level code was automatically generated and embedded onto the devices' on-board computers, which ran at 1 kHz.

The first experiment aimed at analyzing the behavior of the teleoperation system when TDPA was applied without the proposed compensator. The results of that experiment are depicted in Figs 3.24–3.28, which show translational master and slave position, roll-pitch-yaw orientation, translational end-effector control forces, and end-effector control torques, respectively. During that experiment, hard-wall contact was performed once between 10 and 20 seconds (see Fig. 3.24). A second contact was attempted by the operator at around 35 seconds, but that was not achieved due to excessive drift. As it can be noted from Figs 3.24 and 3.25, after 25 seconds of operation, the slave device barely follows the master's commands. This behavior is caused by the passivity enforcing strategy of the slave-side passivity controller and causes significant drift. Adding to that, high frequency oscillations can be seen in the master force and torque values (see Figs. 3.26 and 3.27). That effect, which is caused by the master passivity controller in order to enforce passivity, can be reduced by the use of passive filters (e.g., see [22]).

Figure 3.23: DLR Bimanual Haptic Device.

The second experiment was conducted with the purpose of evaluating the behavior of TDPA with the proposed drift compensator. The results are shown in Figs. 3.29–3.33. A first wall contact was performed between 10 and 20 seconds and is visible in the translational x- and z-axes in Fig. 3.29. A shorter wall contact was performed at around 25 seconds and is mostly visible in the orientation plots (Fig. 3.30). It can be noted that, despite not completely removing the drift in all axes due to the lack of passivity gaps (see Fig. 3.33), the position tracking capabilities of the system when the proposed compensator was applied were significantly improved. The action of the drift compensator can be especially seen on the orientation plots between 25 and 40 seconds, when the position offset is smoothly reduced. It should be noted that, alike the non-compensated case, high frequency force and torque oscillations appear in the compensated one (see Figs. 3.31 and 3.30). Those oscillations are caused by the master passivity controller, which is not directly affected by the compensator.

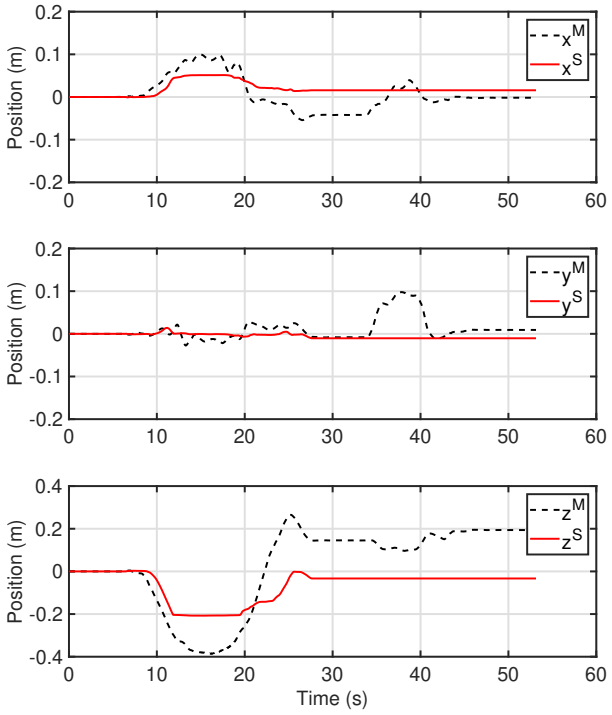

Figure 3.24: Master and slave positions, no drift compensator – $T_{rt} = 800$ ms.

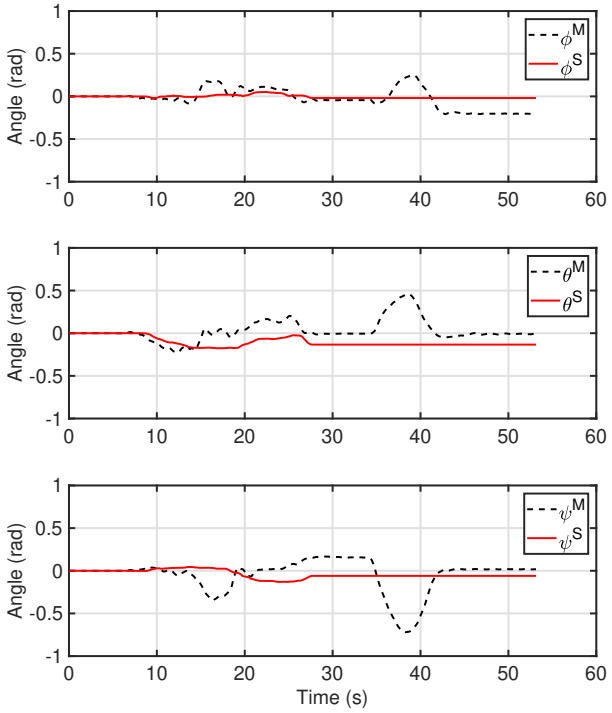

Figure 3.25: Master and slave orientation, no drift compensator – $T_{rt} = 800$ ms.

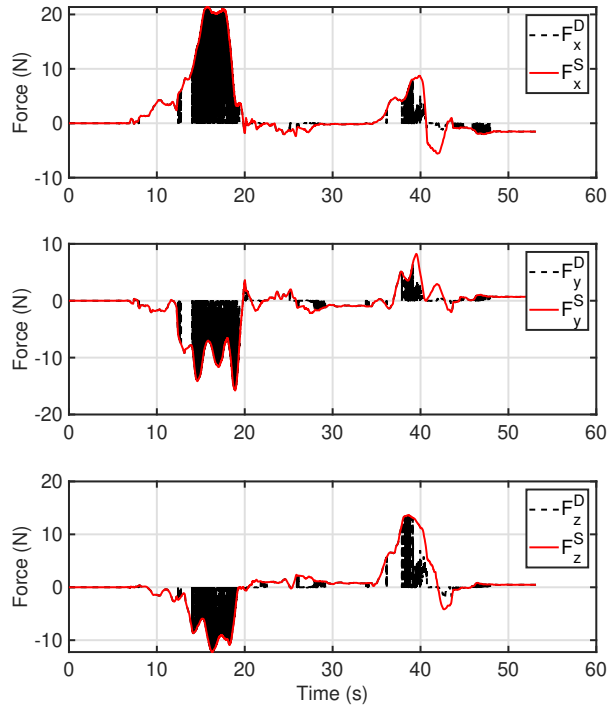

Figure 3.26: Master and slave Cartesian forces in the tool frame, no drift compensator – $T_{rt} = 800$ ms.

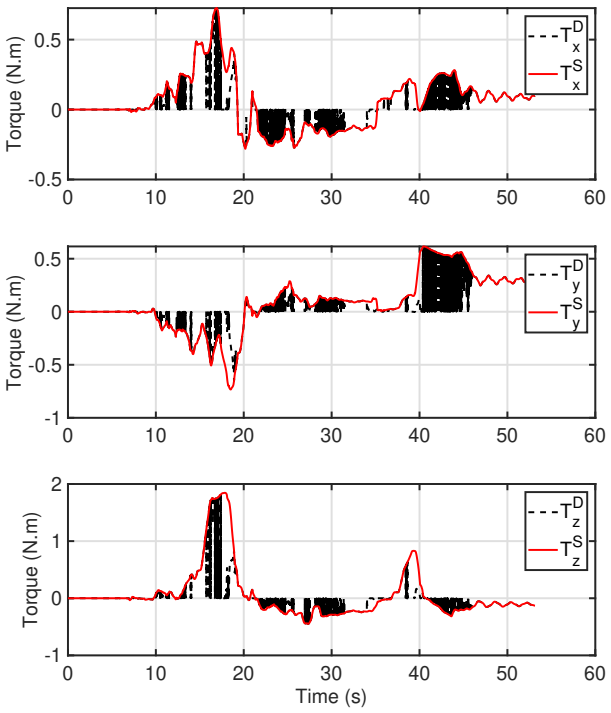

Figure 3.27: Master and slave Cartesian torques in the tool frame, no drift compensator – $T_{rt} = 800$ ms.

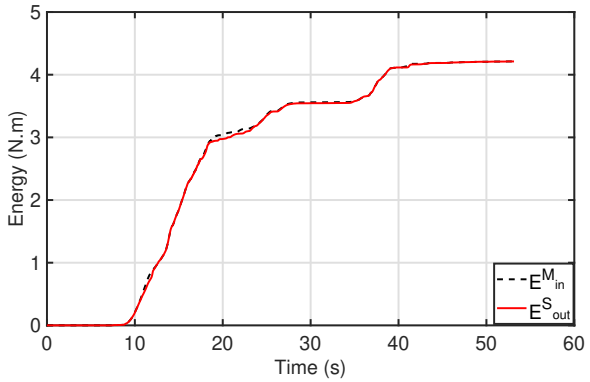

Figure 3.28: Master-in and slave-out energies, no drift compensator – $T_{rt} = 800$ ms.

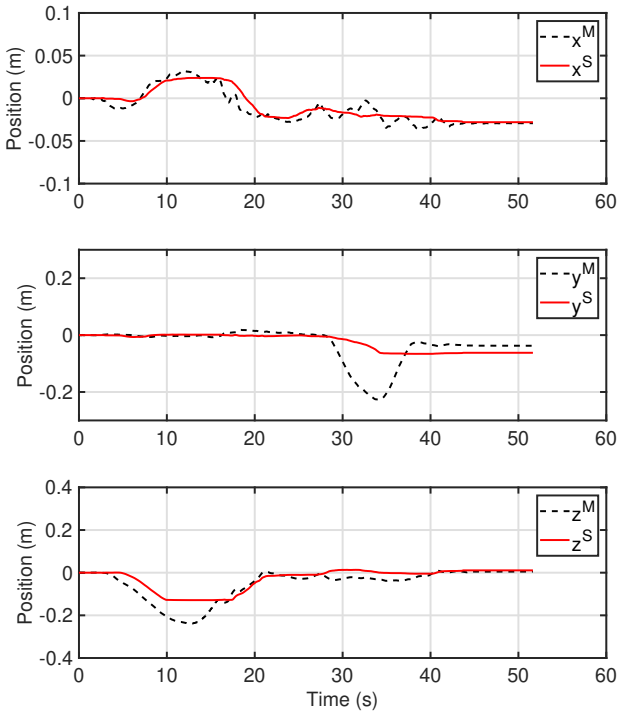

Figure 3.29: Master and slave positions, drift compensator on – $T_{rt} = 800$ ms.

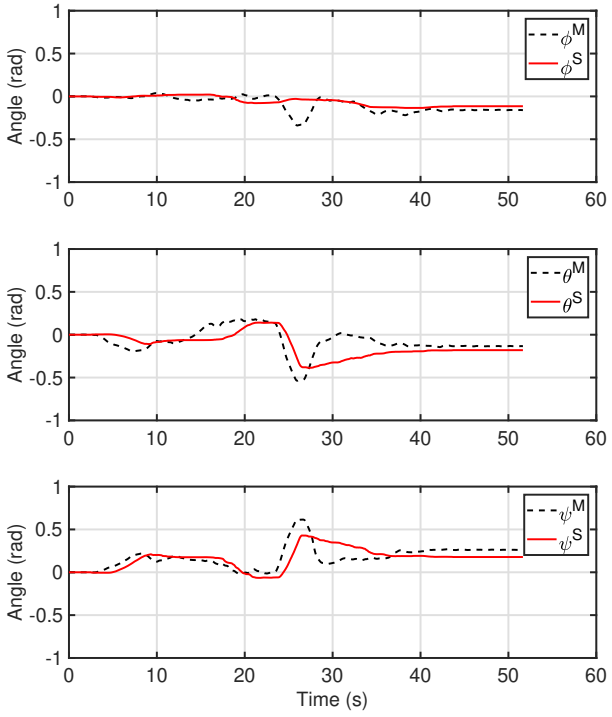

Figure 3.30: Master and slave orientation, drift compensator on – $T_{rt} = 800$ ms.

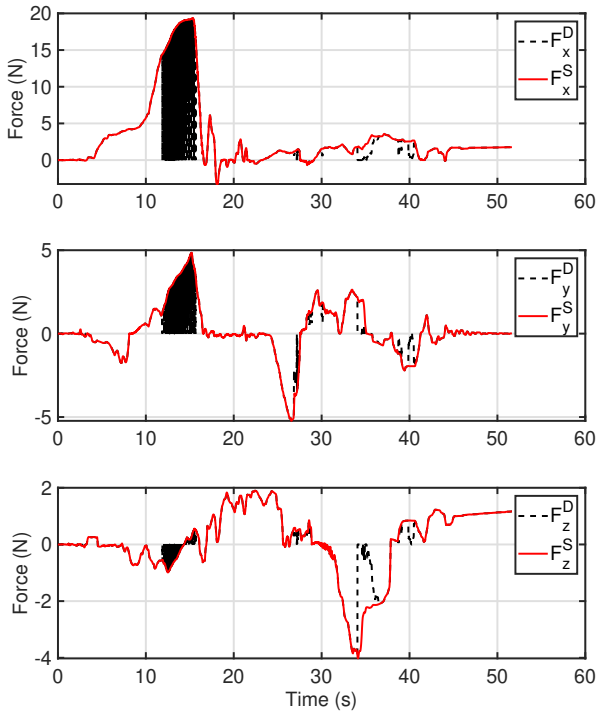

Figure 3.31: Master and slave Cartesian forces in the tool frame, drift compensator on – $T_{rt} = 800$ ms.

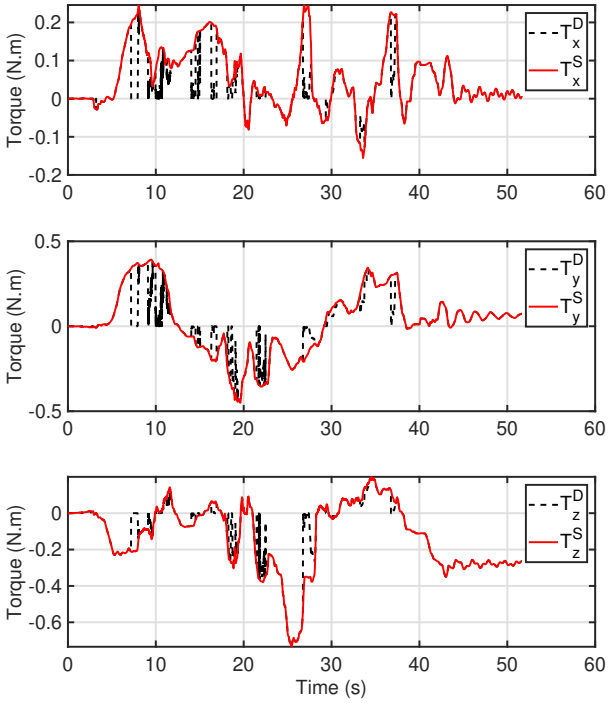

Figure 3.32: Master and slave Cartesian torques in the tool frame, drift compensator on – $T_{rt} = 800$ ms.

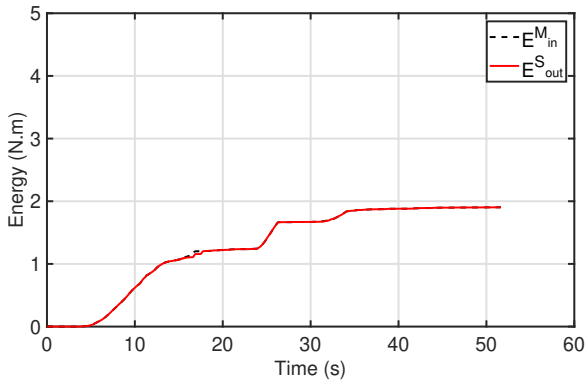

Figure 3.33: Master-in and slave-out energies, drift compensator on – $T_{rt} = 800$ ms.

Chapter 4

Whole-body Control of Redundant Aerial Manipulators

4.1 Overview

This chapter focuses on presenting whole-body control techniques for redundant aerial manipulators, which are necessary for enabling teleoperation of such systems. Initially, state-of-the-art techniques developed for modeling and whole-body control of general redundant manipulators are presented. Subsequently, after introducing the DLR Suspended Manipulator, meaningful whole-body tasks for such systems are discussed and control laws to accomplish them are proposed. Lastly, the results of numerical validation of the proposed techniques are presented and discussed.

4.2 Modeling and Control of General Redundant Manipulators

4.2.1 Kinematics of Redundant Manipulators

Section 2.3 presented the kinematics and dynamics of non-redundant manipulators. However, for redundant manipulators as the SAM where $n > m$, there will be a number of joint velocity combinations, which would yield the same end-effector velocity. This means, $\boldsymbol{J}(\boldsymbol{q})$ does not have a unique inverse map. In this situation, the set of task coordinates can be extended to

$$\begin{bmatrix} \boldsymbol{V} \\ \boldsymbol{V_n} \end{bmatrix} = \bar{\boldsymbol{J}}(\boldsymbol{q})\dot{\boldsymbol{q}} = \begin{bmatrix} \boldsymbol{J}(\boldsymbol{q}) \\ \boldsymbol{N}(\boldsymbol{q}) \end{bmatrix} \dot{\boldsymbol{q}}\,, \tag{4.1}$$

where $\boldsymbol{V_n} \in \mathbb{R}^{n-m}$ is the set of *null-space velocities*. The matrix $\boldsymbol{N}(\boldsymbol{q})$ can be constructed as [37]

$$\boldsymbol{N}(\boldsymbol{q}) = (\boldsymbol{Z}(\boldsymbol{q})\boldsymbol{M}(\boldsymbol{q})\boldsymbol{Z}(\boldsymbol{q})^T)^{-1}\boldsymbol{Z}(\boldsymbol{q})\boldsymbol{M}(\boldsymbol{q})\,, \tag{4.2}$$

where $\boldsymbol{Z}(\boldsymbol{q})$ is a full row rank null-space base matrix, such that $\boldsymbol{J}(\boldsymbol{q})\boldsymbol{Z}(\boldsymbol{q})^T = \boldsymbol{0}$. This matrix can be taken from a Singular-Value Decomposition of $\boldsymbol{J}(\boldsymbol{q})$. Note that the choice of $\boldsymbol{N}(\boldsymbol{q})$ is not unique. In this work, the approach presented by OTT *et al.* [37] is followed. The reader is referred to DIETRICH *et al.* [38] for an overview of the choice of null space projectors.

The definition of $\bar{\boldsymbol{J}}(\boldsymbol{q})$ generates a bijective map between the newly defined task coordinates and the joint coordinates, which will be used in order to define the dynamics the of the manipulator in the task space.

4.2.2 Dynamics and Control of Redundant Manipulators

The dynamic model of a robotic manipulator with n joints can be written as presented in (2.27). By using the previously defined mapping $\bar{\boldsymbol{J}}(\boldsymbol{q})$, a change of coordinates can be performed as

$$\boldsymbol{\Lambda}(\boldsymbol{q}) = \left(\bar{\boldsymbol{J}}(\boldsymbol{q})\,\boldsymbol{M}(\boldsymbol{q})^{-1}\,\bar{\boldsymbol{J}}(\boldsymbol{q})^T\right)^{-1} \tag{4.3}$$

$$\boldsymbol{\mu}(\boldsymbol{q},\dot{\boldsymbol{q}}) = \boldsymbol{\Lambda}(\boldsymbol{q})\left(\bar{\boldsymbol{J}}(\boldsymbol{q})\,\boldsymbol{M}(\boldsymbol{q})^{-1}\,\boldsymbol{C}(\boldsymbol{q},\dot{\boldsymbol{q}}) - \dot{\bar{\boldsymbol{J}}}(\boldsymbol{q})\right)\bar{\boldsymbol{J}}(\boldsymbol{q})^{-1}\,. \tag{4.4}$$

Such formulation allows the manipulator dynamics to be written as

$$\begin{bmatrix}\boldsymbol{\Lambda_x}(\boldsymbol{q}) & 0\\ 0 & \boldsymbol{\Lambda_n}(\boldsymbol{q})\end{bmatrix}\begin{bmatrix}\dot{\boldsymbol{V}}\\ \dot{\boldsymbol{V}}_{\boldsymbol{n}}\end{bmatrix} + \begin{bmatrix}\boldsymbol{\mu}_x(\boldsymbol{q},\dot{\boldsymbol{q}}) & \boldsymbol{\mu}_{xn}(\boldsymbol{q},\dot{\boldsymbol{q}})\\ \boldsymbol{\mu}_{nx}(\boldsymbol{q},\dot{\boldsymbol{q}}) & \boldsymbol{\mu}_n(\boldsymbol{q},\dot{\boldsymbol{q}})\end{bmatrix}\begin{bmatrix}\boldsymbol{V}\\ \boldsymbol{V_n}\end{bmatrix} = \bar{\boldsymbol{J}}(\boldsymbol{q})^{-T}(\boldsymbol{\tau} - \boldsymbol{G}(\boldsymbol{q}))\,, \tag{4.5}$$

where $\boldsymbol{\Lambda_x}(\boldsymbol{q})$ and $\boldsymbol{\Lambda_n}(\boldsymbol{q})$ are the elements of $\boldsymbol{\Lambda}(\boldsymbol{q})$. In addition, $\boldsymbol{\mu}_x(\boldsymbol{q},\dot{\boldsymbol{q}})$, $\boldsymbol{\mu}_{xn}(\boldsymbol{q},\dot{\boldsymbol{q}})$, $\boldsymbol{\mu}_{nx}(\boldsymbol{q},\dot{\boldsymbol{q}})$, and $\boldsymbol{\mu}_n(\boldsymbol{q},\dot{\boldsymbol{q}})$ are the elements of $\boldsymbol{\mu}(\boldsymbol{q},\dot{\boldsymbol{q}})$.

The choice of $\boldsymbol{N}(\boldsymbol{q})$ as in (4.2) generates a block diagonal matrix $\boldsymbol{\Lambda}(\boldsymbol{q})$. However, it is possible to see that the null-space task could still influence the Cartesian space one by means of $\boldsymbol{\mu}_{nx}(\boldsymbol{q},\dot{\boldsymbol{q}})$.

To solve this issue, the joint control torque can be chosen such that the null-space

task has no influence on the Cartesian one as

$$\boldsymbol{\tau} = \boldsymbol{\tau}_x + \boldsymbol{\tau}_n + \boldsymbol{\tau}_\mu + \boldsymbol{G}(\boldsymbol{q})\,, \tag{4.6}$$

$$\boldsymbol{\tau}_x = \boldsymbol{J}(\boldsymbol{q})^T \boldsymbol{F_x}\,, \tag{4.7}$$

$$\boldsymbol{\tau}_n = \boldsymbol{N}(\boldsymbol{q})^T \boldsymbol{Z}(\boldsymbol{q})\, \boldsymbol{J}_2(\boldsymbol{q})^T \boldsymbol{F_n}\,, \tag{4.8}$$

$$\boldsymbol{\tau}_\mu = \bar{\boldsymbol{J}}(\boldsymbol{q})^T \begin{bmatrix} \mathbf{0} & \boldsymbol{\mu}_{xn}(\boldsymbol{q}, \dot{\boldsymbol{q}}) \\ \boldsymbol{\mu}_{nx}(\boldsymbol{q}, \dot{\boldsymbol{q}}) & \mathbf{0} \end{bmatrix} \begin{bmatrix} \boldsymbol{V} \\ \boldsymbol{V_n} \end{bmatrix}\,, \tag{4.9}$$

where $\boldsymbol{J}_2(\boldsymbol{q})$ is the Jacobian of a secondary task, which could be performed in the null space of the primary one. Moreover, $\boldsymbol{F_x}$ is a Cartesian-space wrench and $\boldsymbol{F_n}$ is the control wrench of the secondary task, before being projected into the null space of the primary one. It is important to note that, even if no null-space task is commanded, i.e., $\boldsymbol{\tau}_n = \mathbf{0}$, the null-space velocity $\boldsymbol{V_n}$ is likely to be nonzero. Therefore, the choice of the aforementioned control law is advisable for any redundant manipulator.

With the aforementioned control torque, the dynamics of the Cartesian-space task can be rewritten as

$$\boldsymbol{\Lambda_x}(\boldsymbol{q})\dot{\boldsymbol{V}} + \boldsymbol{\mu_x}(\boldsymbol{q}, \dot{\boldsymbol{q}})\boldsymbol{V} = \boldsymbol{F_x}\,, \tag{4.10}$$

where $\boldsymbol{F_x}$ could implement a control law in the Cartesian-space (e.g., see [37]).

The above described dynamic decoupling allows for the teleoperation of the Cartesian space of kinematically redundant manipulators without taking the energy generated by the null-space task into account or having null-space velocities disturb the main task.

4.3 The Suspended Aerial Manipulator

The suspended Suspended Aerial Manipulator (SAM, [12]) developed at the German Aerospace Center (see Fig. 1.1) consists of an omnidirectional octarotor system with eight body-frame fixed unidirectional propellers, which hangs by means of a steerable set of cables. The lengths of the cables can be varied in order to control a number of degrees of freedom of the platform. The platform is intended to hang from either a crane or an unmanned helicopter, which is able to fly to desired positions in order to extended the workspace of the system. The integration concept of the Suspended Aerial Manipulator can be seen in Figure 4.1.

The pose of the propellers was defined through numerical optimization, following the work presented by TOGNON and FRANCHI [39] in order to maximize the force and torque exertion capability of the octarotor. With eight fixed propellers, a constant full-rank matrix $\mathbf{B} \in \mathbb{R}^{6\times 8}$ maps propeller thrusts $\mathbf{u} \in \mathbb{R}^8$ to body wrenches

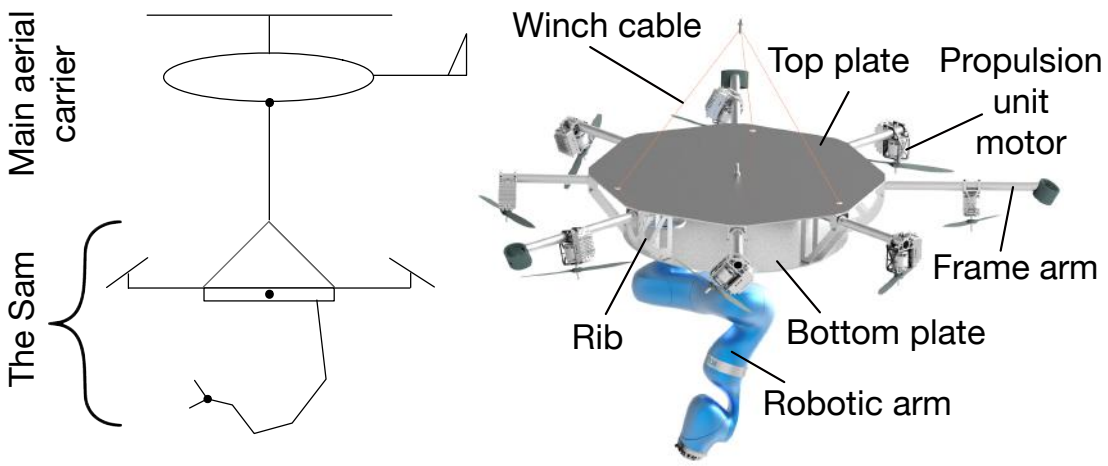

Figure 4.1: An integration concept (left) and the structure of the platform (right).

Figure 4.2: KUKA LWR manipulator.

of the octarotor, $\mathbf{F_b} \in \mathbb{R}^6$, as follows.

$$\mathbf{F_b} = \mathbf{Bu} \tag{4.11}$$

Attached to the octarotor is a KUKA LWR IV manipulator [40] (see Figure 4.2). This device is a 7-DoF torque controlled robotic arm suitable for industrial applications involving human-robot interactions.

4.4 Whole-Body Control of Redundant Omnidirectional Aerial Manipulators

4.4.1 Modeling

In order to simulate teleoperation tasks performed by the Suspended Aerial Manipulator, its simplified model was developed. By taking the cable structure into account, the system becomes a parallel manipulator [29]. The modeling of such systems requires the application of additional techniques, which are beyond the scope of this thesis. For the purpose of applying whole-body control and aerial manipulation techniques, the system was considered as a free-flying omnidirectional manipulator, as shown in Fig. 4.3. Such a model should locally hold for the SAM, especially if the mass of the cables is negligible.

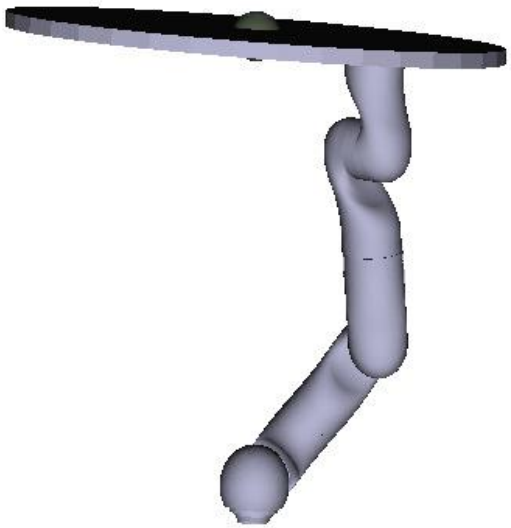

Figure 4.3: Model of a free-flying omnidirectional aerial manipulator

The dynamics of such system can be described as in (2.27), where a total of 13 generalized coordinates was chosen. The first six coordinates represents a set of three rotational and three translational joints, which describe the set of all possible rigid body motions performed by the omnidirectional platform. The remaining seven generalized coordinates were chosen to be the joint angles of the LWR manipulator.

In order to compute the kinematics and dynamics of the system, an iterative Newton-Euler-based algorithm [41] was applied. That algorithm provided the values of the dynamic matrices ($\boldsymbol{M}(\boldsymbol{q})$, $\boldsymbol{C}(\boldsymbol{q}, \dot{\boldsymbol{q}})$, and $\boldsymbol{G}(\boldsymbol{q})$ from 2.27) and their time derivatives evaluated at each time-step, based on a URDF file [42] containing the kinematic and dynamic parameters of the aerial manipulator.

4.4.2 Control

This section describes the Cartesian and Null-space control laws applied to the aerial manipulator, which will be plugged into (4.6)-(4.9).

Primary task

The primary task performed by the aerial manipulator is the control of its end-effector. For that task, the Jacobian mapping from joint velocities, $\dot{\boldsymbol{q}} \in \mathbb{R}^{13}$, to end-effector velocities, $\boldsymbol{V} \in \mathbb{R}^6$, is given by the matrix $\boldsymbol{J}(\boldsymbol{q}) \in \mathbb{R}^{6\times 13}$.

In order to control the end-effector pose in the Cartesian space, its desired pose with respect to the robot's base frame can be described in $SE(3)$ as

$$\boldsymbol{g}_{\mathcal{BD}} = \begin{bmatrix} \boldsymbol{R}_{\mathcal{BD}} & \boldsymbol{p}_{\mathcal{BD}} \\ \boldsymbol{0} & 1 \end{bmatrix} . \tag{4.12}$$

Likewise, the robot end-effector pose with respect to its base frame can be represented as

$$\boldsymbol{g}_{\mathcal{BT}} = \begin{bmatrix} \boldsymbol{R}_{\mathcal{BT}} & \boldsymbol{p}_{\mathcal{BT}} \\ \boldsymbol{0} & 1 \end{bmatrix} . \tag{4.13}$$

Accordingly, an error homogeneous transformation can be defined as

$$\boldsymbol{g}_{\mathcal{DT}} = {\boldsymbol{g}_{\mathcal{BD}}}^{-1} \boldsymbol{g}_{\mathcal{BT}} = \begin{bmatrix} \boldsymbol{R}_{\mathcal{DT}} & \boldsymbol{p}_{\mathcal{DT}} \\ \boldsymbol{0} & 1 \end{bmatrix} . \tag{4.14}$$

This element can be interpreted as describing the basis vectors of the tool frame with respect to the basis vector of the desired tool frame. Adding to that, a velocity error can be defined as

$${}^{\mathcal{T}}\boldsymbol{V}_{\mathcal{DT}} = {}^{\mathcal{T}}\boldsymbol{V}_{\mathcal{BT}} - \mathrm{Ad}_{\boldsymbol{g}_{\mathcal{DT}}^{-1}} {}^{\mathcal{D}}\boldsymbol{V}_{\mathcal{BD}} , \tag{4.15}$$

where the velocities ${}^{\mathcal{T}}\boldsymbol{V}_{\mathcal{BT}}$ and ${}^{\mathcal{D}}\boldsymbol{V}_{\mathcal{BD}} \in \mathbb{R}^6$ represent body velocities of the element $\boldsymbol{g}_{\mathcal{BT}}$ and $\boldsymbol{g}_{\mathcal{BD}} \in SE(3)$, respectively.

With this definition, a Cartesian PD controller can be implemented in the end-effector frame as

$${}^{\mathcal{T}}\boldsymbol{F}_{\boldsymbol{x}} = -\begin{bmatrix} k_\omega \log_{SO(3)}(\boldsymbol{R}_{\mathcal{DT}}) \\ k_v \boldsymbol{R}_{\mathcal{DT}}^T \boldsymbol{p}_{\mathcal{DT}} \end{bmatrix} - \boldsymbol{K}_D {}^{\mathcal{T}}\boldsymbol{V}_{\mathcal{DT}} , \tag{4.16}$$

where k_v and $k_\omega \in \mathbb{R}$ are positive position and orientation stiffness gains, respectively, defined in the tool frame. In addition, $\boldsymbol{K}_D \in \mathbb{R}^{6\times 6}$ is a positive-definite Cartesian-damping matrix.

Note that, even though tracking tasks are intended to be performed, the proposed Cartesian PD controller resembles the regulation controller presented in Section 2.4.2 and not the tracking controller presented in Section 2.4.3. This is due to two reasons. The main reason is that, since the desired velocity during teleoperation tasks is given by the human operator and not by a trajectory generation code, the desired acceleration is not available. Adding to that, the aerial manipulator is intended to be used in unstructured-environment interaction tasks, which are more safely performed when controllers with some compliant behavior are applied [37]. Therefore, perfect tracking is not guaranteed by the proposed controller. However, if the desired acceleration is low and the controller gains are high enough, satisfactory tracking can be achieved. The reason for that can be explained by perturbation theory (see [32]). As will be seen in the numerical validation section, satisfactory tracking is indeed achieved by the proposed controller. In practice, actuator limitations have to be taken into account when choosing gains. In this thesis, gain magnitudes were chosen based on the experience of colleagues working on other robotic systems at the German Aerospace Center, but have not yet been tested on the SAM.

Null-space task

Under the assumption of full rank of $\boldsymbol{J}(\boldsymbol{q})$, its null space, $\mathcal{N}\{\boldsymbol{J}(\boldsymbol{q})\}$, will have nonzero dimension. This allows a secondary task to be performed in the null space of the primary.

For the aerial manipulation platform, it has been considered meaningful to attempt to keep the base steady. As a secondary task, this would make sure the base only moves when it is necessary in order reach points in the Cartesian space that would not be reachable by moving the arm alone. Such approach also prevents the flying base from tilting unnecessarily, which could increase the power consumption of the propellers in order to compensate for gravity. In addition, an extra LWR joint angle can be used to maximize the manipulability measure [43] and avoid singularities. The manipulability measure can be defined as

$$w(\boldsymbol{q}) = \sqrt{\det(\boldsymbol{J}(\boldsymbol{q})\,\boldsymbol{J}(\boldsymbol{q})^T)}\,. \tag{4.17}$$

The above described secondary task coordinates can be described by

$$\begin{bmatrix} \dot{\boldsymbol{q}}_{1-6} \\ \dot{q}_{10} \end{bmatrix} = \begin{bmatrix} \mathbf{I}_6 & \mathbf{0}_{6\times3} & \mathbf{0}_{6\times1} & \mathbf{0}_{6\times3} \\ \mathbf{0}_{1\times6} & \mathbf{0}_{1\times3} & 1 & \mathbf{0}_{1\times3} \end{bmatrix} \dot{\boldsymbol{q}} = \boldsymbol{J}_2(\boldsymbol{q})\,\dot{\boldsymbol{q}}\,, \tag{4.18}$$

where $\boldsymbol{J}_2(\boldsymbol{q}) \in \mathbb{R}^{7\times13}$ is a selection matrix, which selects the joints to be controlled in the secondary task, i.e., joints 1 to 6 from the flying base and joint 10, which

corresponds to the fourth LWR joint.

The secondary-task force can be defined as

$$\boldsymbol{F_n} = \begin{bmatrix} -\boldsymbol{K}_{Pb}\,\boldsymbol{q}_{1-6} - \boldsymbol{K}_{Db}\,\dot{\boldsymbol{q}}_{1-6} \\ K_m \dfrac{\partial w(\boldsymbol{q})}{\partial q_{10}} - K_{d10}\dot{q}_{10} \end{bmatrix}, \tag{4.19}$$

where $\boldsymbol{K}_{Pb} \in \mathbb{R}^{6\times6}$ and $\boldsymbol{K}_{Db} \in \mathbb{R}^{6\times6}$ are the positive definite proportional and derivative gain matrices acting to keep the flying-base joints at zero, K_m is a positive gain multiplying the manipulability gradient with respect to q_{10}, and K_{d10} is a damping factor applied to joint 10. Adding K_{d10} makes sure q_{10} will not change abruptly while trying to maximize the manipulability measure.

The above defined expressions for the Jacobian matrix $\boldsymbol{J}_2(\boldsymbol{q})$ and the secondary-task force $\boldsymbol{F_n}$ can be plugged into (4.8), where they will be projected into the null space of the primary task.

4.5 Numerical Validation

In order to analyze the efficacy of the aforementioned whole-body controller, three different control strategies were applied to the simulated aerial manipulator. Initially, a non-hierarchical controller with conflicting tasks was implemented (no. 1). Subsequently, the whole-body controller was applied. First, without a secondary task (no. 2), and, subsequently, adding the previously described secondary task in the null space of the primary one (no. 3).

Table 4.1 depicts the Cartesian controller gains used in all three simulations. The term diag(.) means that the matrix has the specified elements as its main diagonal and all non-diagonal elements are zero. Table 4.2 shows the null-space controller parameters applied to each of the tasks.

Table 4.1: Cartesian controller gains

k_v	k_ω	$\boldsymbol{K}_D$
500	300	diag(100 100 300 230 230 230)

Table 4.2: Null-space controller parameters

no.	**Projector**	$\boldsymbol{\tau}_\mu$	$\boldsymbol{K}_{Pb}$	$\boldsymbol{K}_{Db}$	K_m	K_{d10}
1	$\mathbf{I}_{13}$	$\mathbf{0}$	$100\,\mathbf{I}_3$	$200\,\mathbf{I}_3$	0.2	2
2	$\boldsymbol{N}(\boldsymbol{q})^T\boldsymbol{Z}(\boldsymbol{q})$	Eq. 4.9	$\mathbf{0}$	$\mathbf{0}$	0	0
3	$\boldsymbol{N}(\boldsymbol{q})^T\boldsymbol{Z}(\boldsymbol{q})$	Eq. 4.9	$100\,\mathbf{I}_3$	$200\,\mathbf{I}_3$	0.2	2

Figs. 4.4–4.7 present the results of the application of the two-task controller without task hierarchy implementation via null-space projection (no. 1). Fig. 4.4

shows the desired and actual values of the Cartesian positions of the end-effector while Fig. 4.5 depicts the end-effector orientation using a Roll-Pitch-Yaw representation. Fig. 4.6 shows the norm of the control torque values. Fig. 4.7 presents the squared norm of the vector $\boldsymbol{q}_{1-6}$ and the value of the manipulability measure $w(\boldsymbol{q})$ from (4.17).

Figs. 4.8–4.11 show the results of the application of the dynamic-decoupling controller with only the Cartesian-space task being performed. Figs. 4.8 and 4.9 show the position and orientation of the end-effector, Fig. 4.10 depicts the norm of the control torques, and Fig. 4.11 shows the square of the norm of $\boldsymbol{q}_{1-6}$ and the manipulability value.

Figs. 4.12–4.15 show the results of the application of the dynamic-decoupling controller with the above-described secondary task being performed in the null space of the Cartesian one. Figs. 4.12 and 4.13 show the position and orientation of the end-effector, Fig. 4.14 shows the norm of the control torques, and Fig. 4.15 shows the square of the norm of $\boldsymbol{q}_{1-6}$ and the manipulability value.

Table 4.3 shows a comparison between the control performance parameters for each controller. Namely, average value of the absolute position and orientation errors, average value for the squared-norm of $\boldsymbol{q}_{1-6}$, average manipulability, and average values of the norms of the control torques. Values whose order of magnitude is 10^{-4} and below are shown as zero.

Table 4.3: Control performance parameters

no.	$\bar{x}_e$	$\bar{y}_e$	$\bar{z}_e$	$\bar{\phi}_e$	$\bar{\theta}_e$	$\bar{\psi}_e$	$\bar{\boldsymbol{q}}_{1-6}$	$\bar{w}(\boldsymbol{q})$	$\bar{\boldsymbol{\tau}}_x$	$\bar{\boldsymbol{\tau}}_n$	$\bar{\boldsymbol{\tau}}_\mu$
1	0.048	0.001	0.064	0.004	0.001	0.001	0.141	9.109	67.20	67.75	0
2	0.002	0	0.002	0.001	0.001	0	0.568	9.430	2.993	0	0.874
3	0.002	0	0.002	0.001	0.001	0	0.218	9.635	3.292	2.546	1.810

It can be noted that, when two control tasks were applying without a conflict resolution strategy (no. 1), the Cartesian-space task had its position tracking performance worsened in comparison with the decoupled controllers (no. 2 and 3). This can be seen from the error values from Table 4.3 as well as by comparing Figs. 4.4 and 4.5 with Figs. 4.8, 4.9, 4.12, and 4.13. In addition, due to the conflicting nature of the tasks being performed, the controller had to apply much higher torques in order to fulfill both tasks. From Table 4.3 it can be noted that the average torques $\boldsymbol{\tau}_x$ and $\boldsymbol{\tau}_n$ applied by the conflicting controller (no. 1) were more than 20 times as high as those applied in the hierarchically decoupled controller (no. 3).

When comparing the position tracking between the two dynamically decoupled controllers, with and without a secondary task (no. 2 and no. 3, respectively), it can be noted that the tracking performance was not altered when a secondary task was added. This is due to the fact that the secondary task does not influence

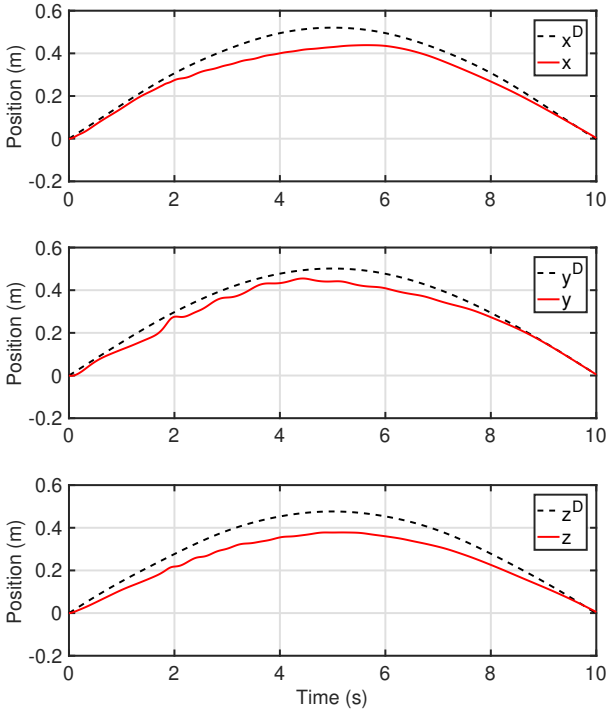

Figure 4.4: End-effector positions – Conflicting-task controller with no null-space projection (no. 1).

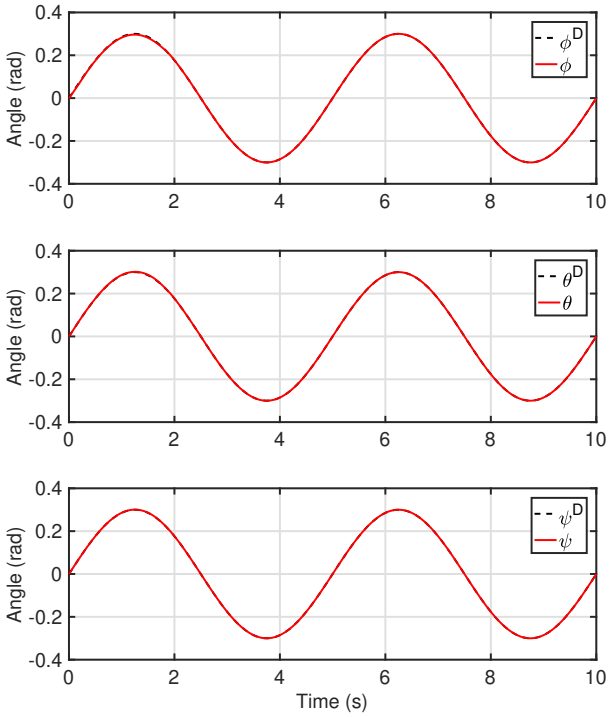

Figure 4.5: End-effector orientations – Conflicting-task controller with no null-space projection (no. 1).

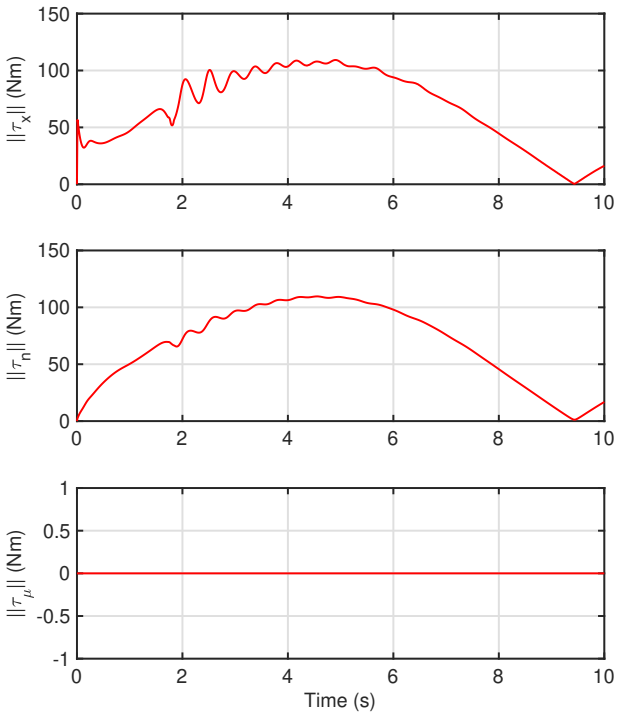

Figure 4.6: Control torques – Conflicting-task controller with no null-space projection (no. 1).

the primary one when being projected into its null space. It is also important to remark that the control torques remained in the same order of magnitude when the secondary task was applied.

Another remarkable result of the dynamically decoupled controller with a secondary task (no. 3) is that it was able to increase the average manipulability value of the manipulator and decrease the joint angles of the flying base ($\boldsymbol{q}_{1-6}$) in comparison to the case when no secondary task was performed. In comparison with controller no. 1, despite increasing the average manipulability, controller no. 3 presented a higher average value for joints $\boldsymbol{q}_{1-6}$. This is due to the fact that the projection of the secondary control action reduces its capability at the cost of not influencing the primary task. However, since the regulation of the flying base is a secondary task, this behavior is desirable.

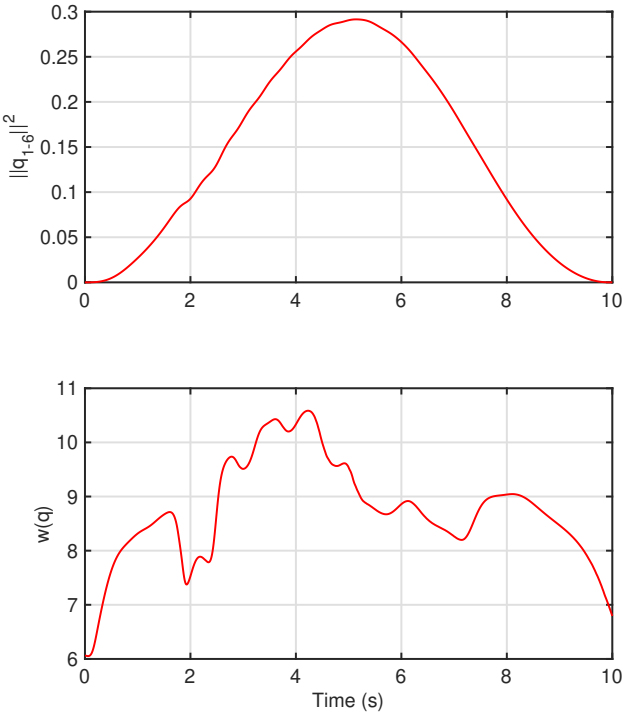

Figure 4.7: Optimized measures – Conflicting-task controller with no null-space projection (no. 1).

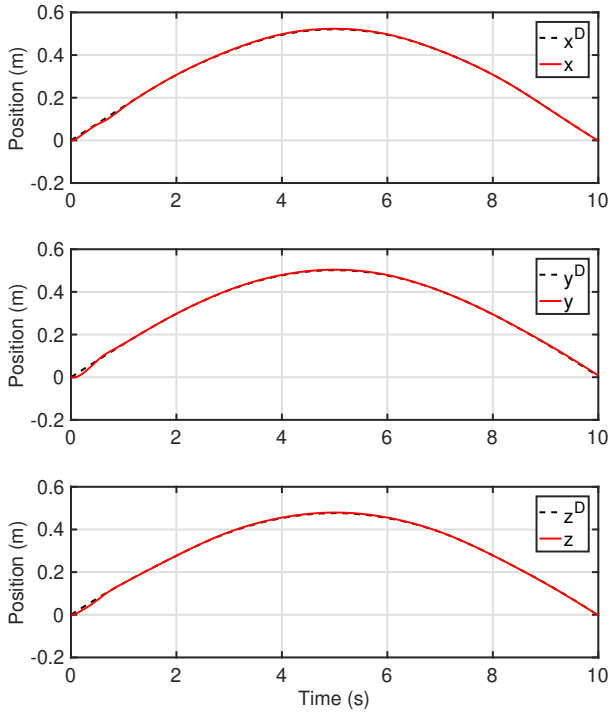

Figure 4.8: End-effector positions – Dynamically decoupled whole-body controller with no secondary task (no.2).

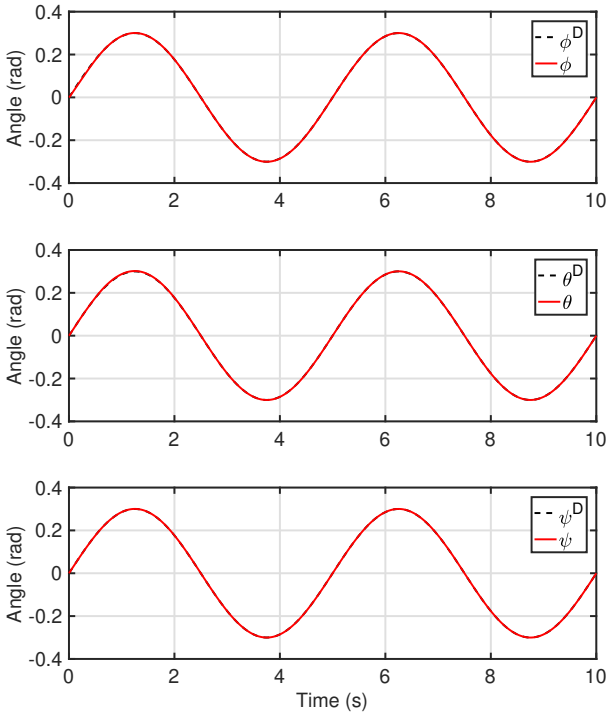

Figure 4.9: End-effector orientations – Dynamically decoupled whole-body controller with no secondary task (no.2).

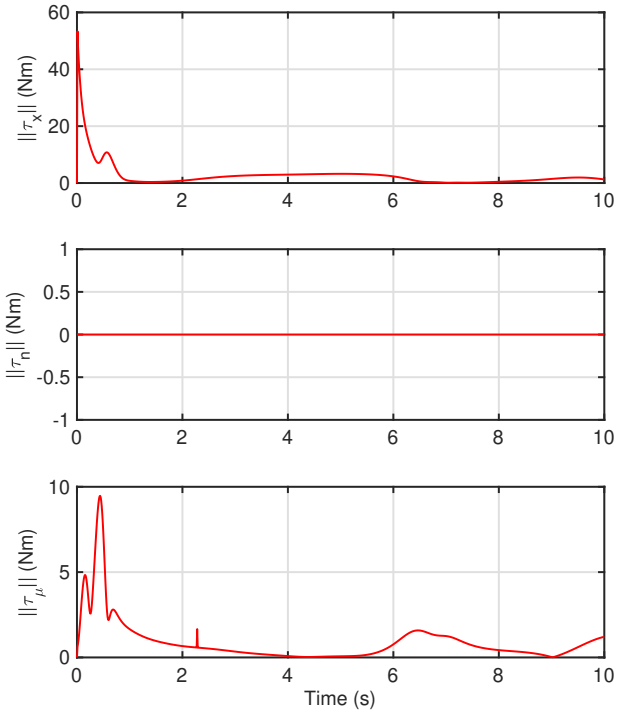

Figure 4.10: Control torques – Dynamically decoupled whole-body controller with no secondary task (no.2).

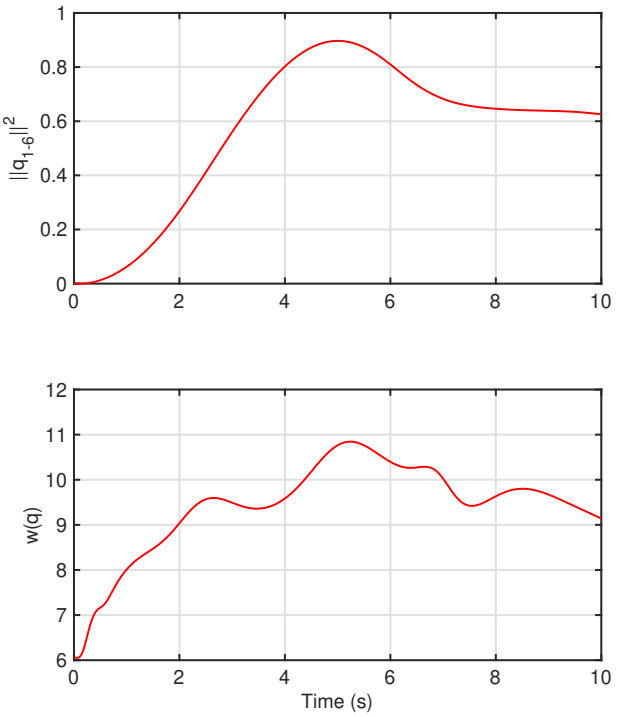

Figure 4.11: Optimized measures – Dynamically decoupled whole-body controller with no secondary task (no.2).

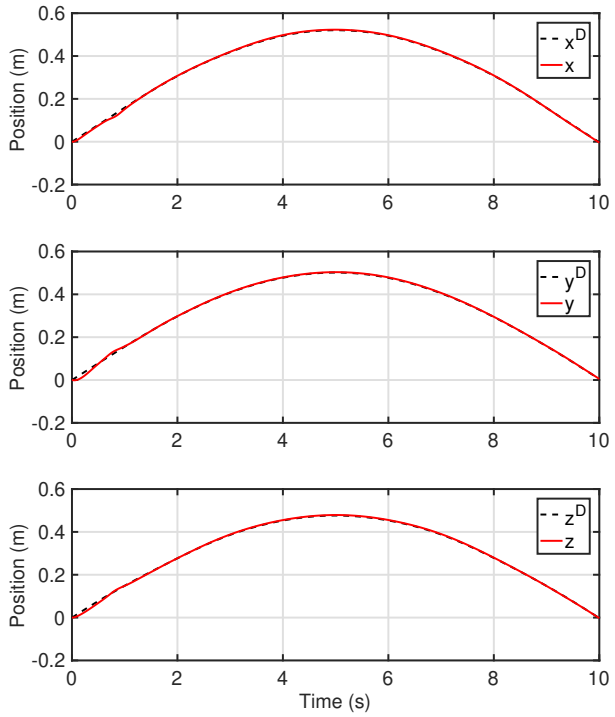

Figure 4.12: End-effector positions – Dynamically decoupled whole-body controller with secondary task (no.3).

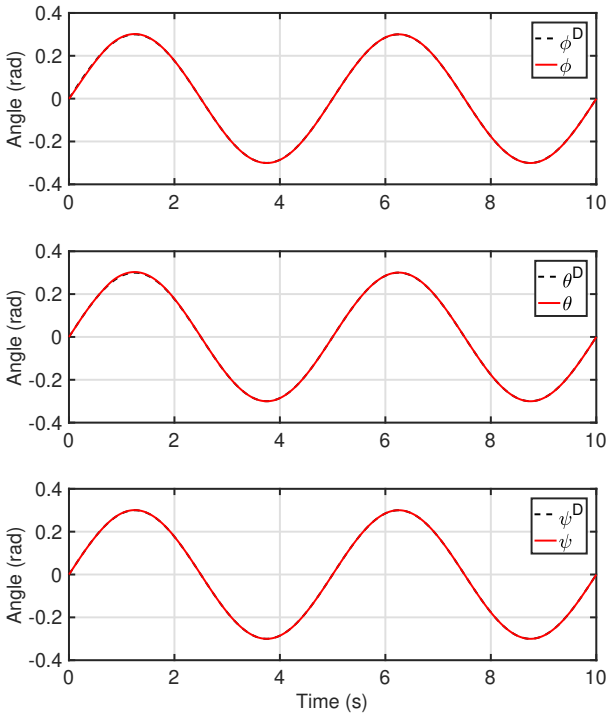

Figure 4.13: End-effector orientations – Dynamically decoupled whole-body controller with secondary task (no.3).

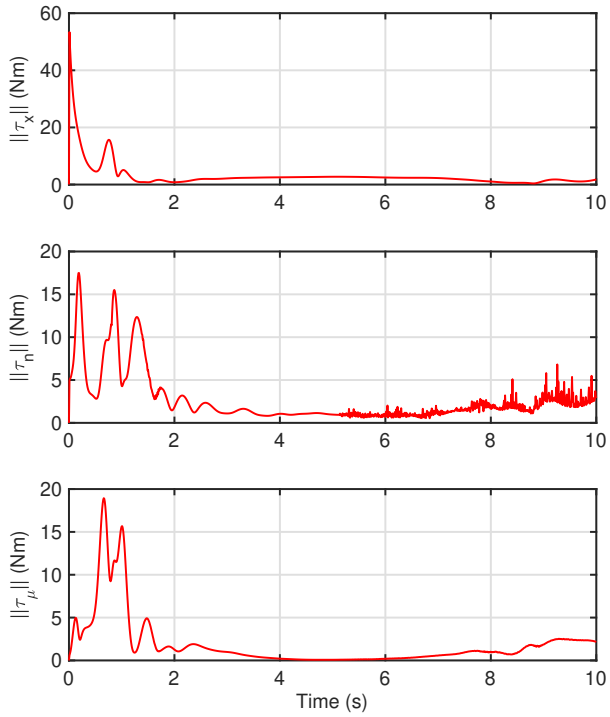

Figure 4.14: Control torques – Dynamically decoupled whole-body controller with secondary task (no.3).

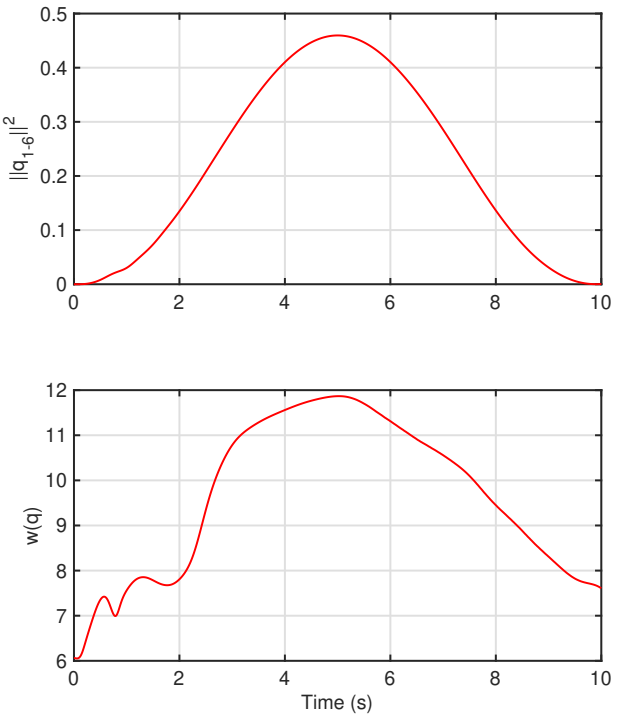

Figure 4.15: Optimized measures – Dynamically decoupled whole-body controller with secondary task (no.3).

Chapter 5

Bilateral Teleoperation of a Redundant Aerial Manipulator

5.1 Overview

This chapter brings together the approaches presented in Chapters 3 and 4 in order to show numerical simulation results of bilateral teleoperation of the Cartesian space of a redundant Aerial Manipulator.

The aerial manipulator was teleoperated as the slave of a P-F architecture. The slave controller was the dynamically decoupled controller described in Chapter 4. This allowed the Cartesian-space teleoperation task to be performed without having to take the energy acting in the null space into account.

The performance of the teleoperation task with the coupled passivity controller from Section 3.3.3 is evaluated with and without the multi-DoF compensator presented in Section 3.5. In order to show the applicability of the proposed multi-DoF drift compensation law, the compensator was applied to the teleoperation of the Cartesian space of the Suspended Aerial Manipulator when round-trip communication delays of 700 ms were present.

5.2 Numerical Simulation Results

Figs 5.1–5.5 depict the Cartesian positions, tool-frame forces and torques, and slave-side energy signals computed when applying coupled TDPA without drift compensation. It is important to note that Roll-Pitch-Yaw angles were used in order to facilitate the understanding of the orientation plots. However, this representation is not used in the compensation law.

From Figs. 5.1 and 5.2, significant drift caused by the admittance-type PC can be observed in all axes. In addition, from Fig. 5.5 it can be seen that the PO-PC

pair keeps the energy coming out of the channel on the slave side smaller than the one that is flowing into it on the master side.

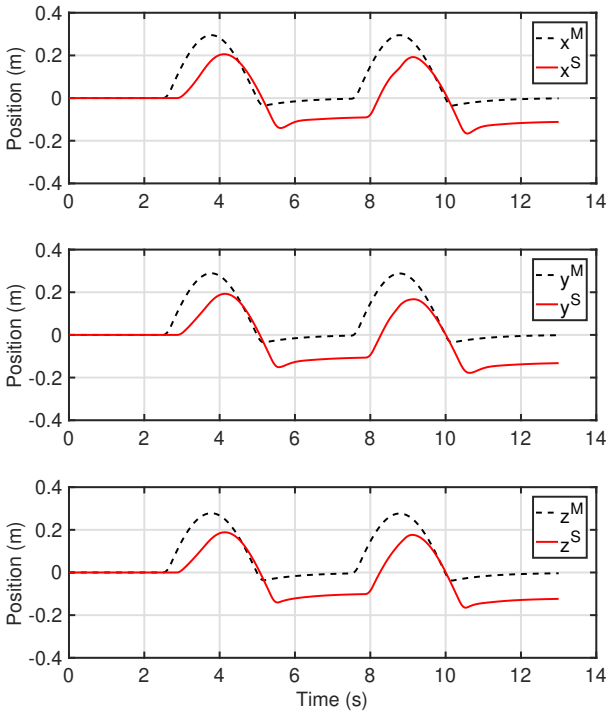

Figure 5.1: Master and slave positions, no drift compensator – $T_{rt} = 700$ ms.

When drift compensation was added (Figs. 5.6–5.10), it can be noted that the drift converged to zero in all position and orientation axes (see Figs. 5.6 and 5.7). It is also important to remark that the control forces and torques were not increased significantly when the compensator was applied (compare Figs. 5.3 and 5.4 with Figs. 5.8 and 5.9). Moreover, it can be seen in Fig. 5.10 that the passivity controller kept the system passive, allowing the compensator to act only when passivity gaps were present.

The numerical simulation results show that the compensator is able to preserve the controller tracking capabilities even in the presence of high communication delays without compromising the overall stability of the system. This allows the application of TDPA to tasks to which it would not be otherwise suitable due to the induced position drift.

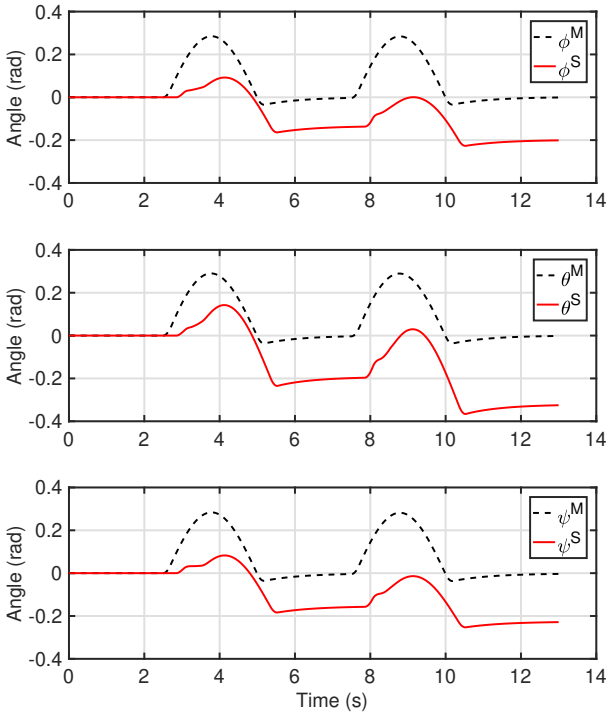

Figure 5.2: Master and slave orientation, no drift compensator – $T_{rt} = 700$ ms.

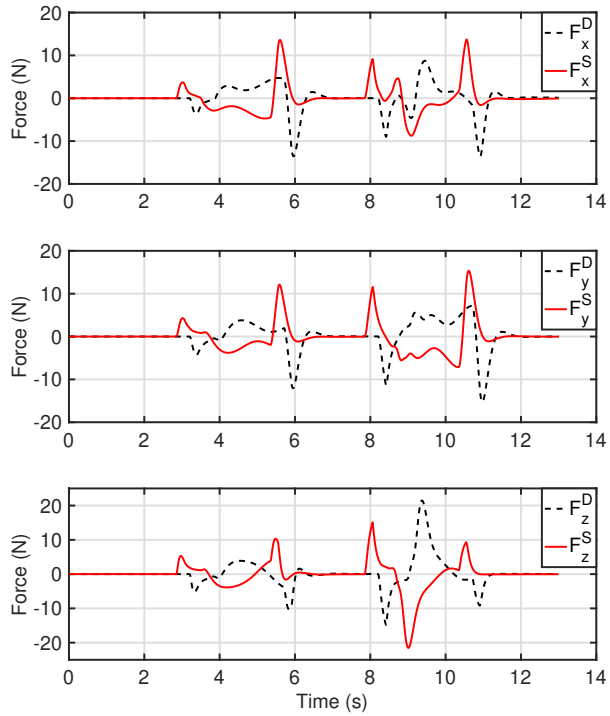

Figure 5.3: Master and slave Cartesian forces in the tool frame, no drift compensator – $T_{rt} = 700$ ms.

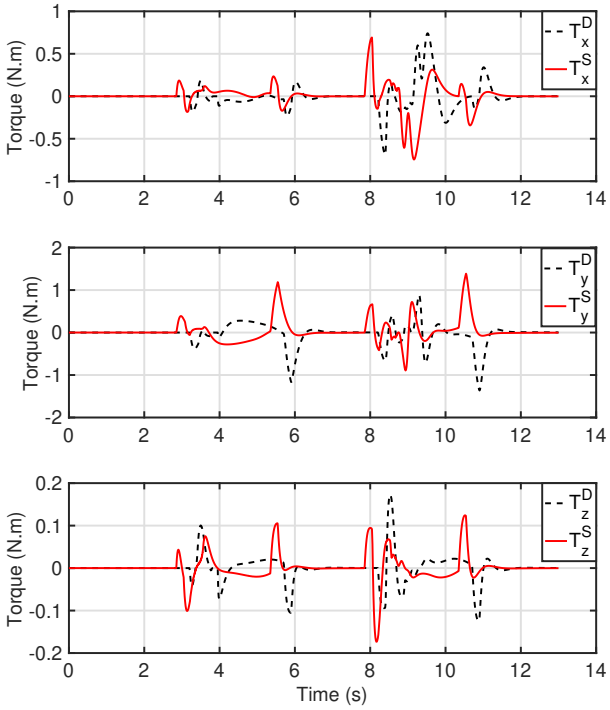

Figure 5.4: Master and slave Cartesian torques in the tool frame, no drift compensator – $T_{rt} = 700$ ms.

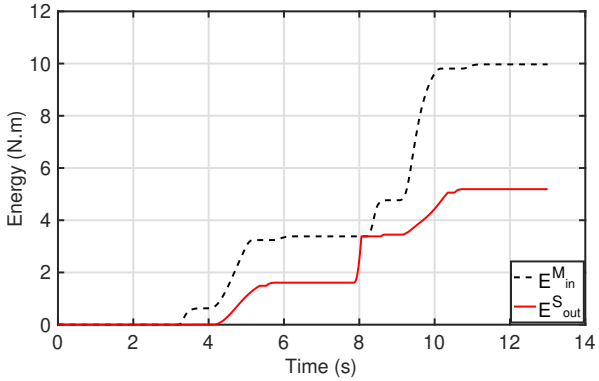

Figure 5.5: Master-in and slave-out energies, no drift compensator – $T_{rt} = 700$ ms.

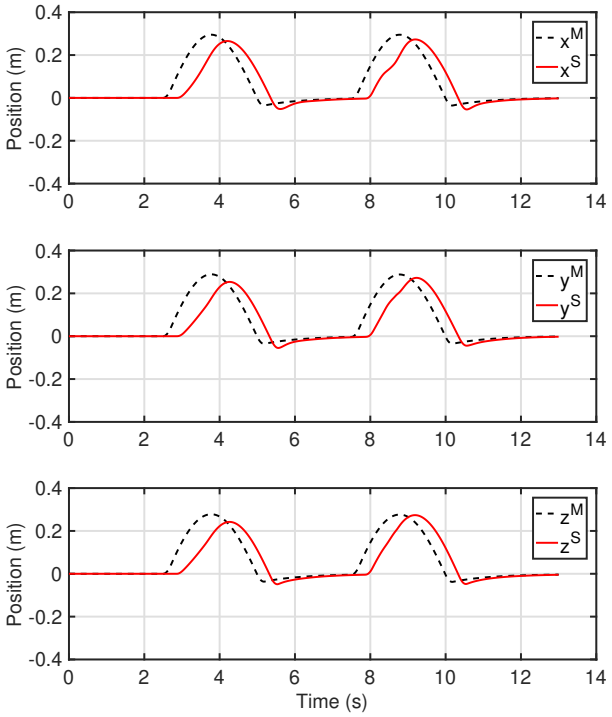

Figure 5.6: Master and slave positions, drift compensator on – $T_{rt} = 700$ ms.

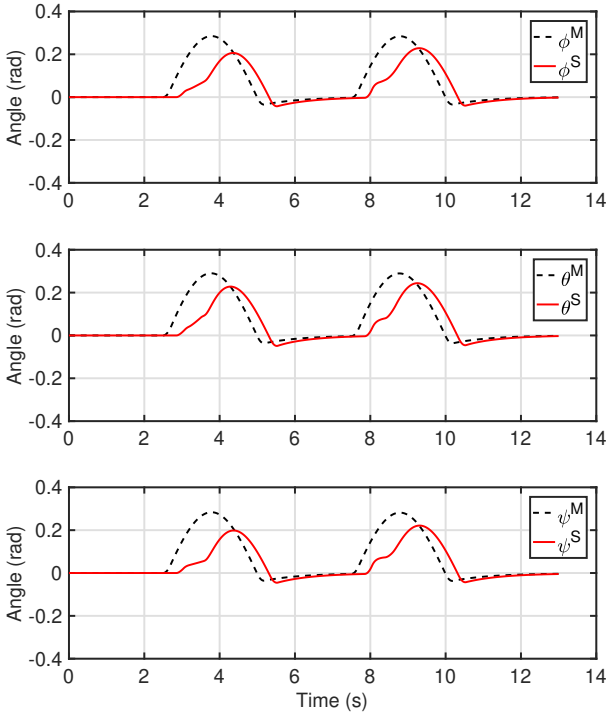

Figure 5.7: Master and slave orientation, drift compensator on – $T_{rt} = 700$ ms.

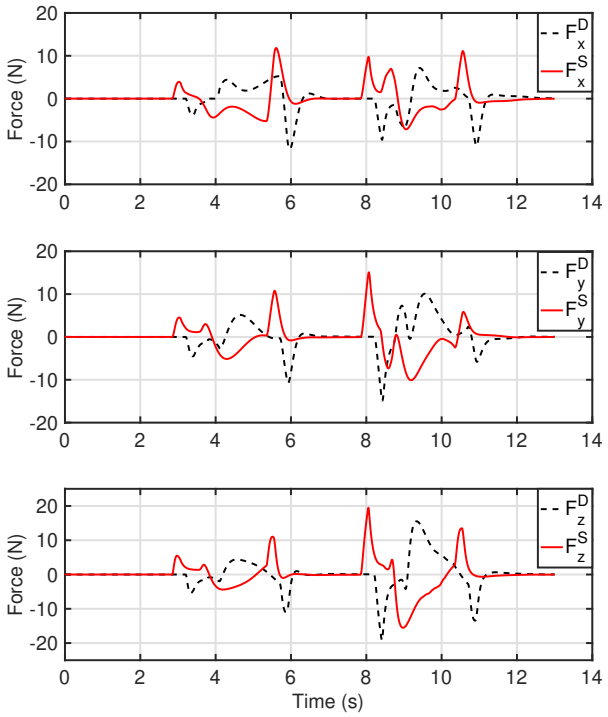

Figure 5.8: Master and slave Cartesian forces in the tool frame, drift compensator on – $T_{rt} = 700$ ms.

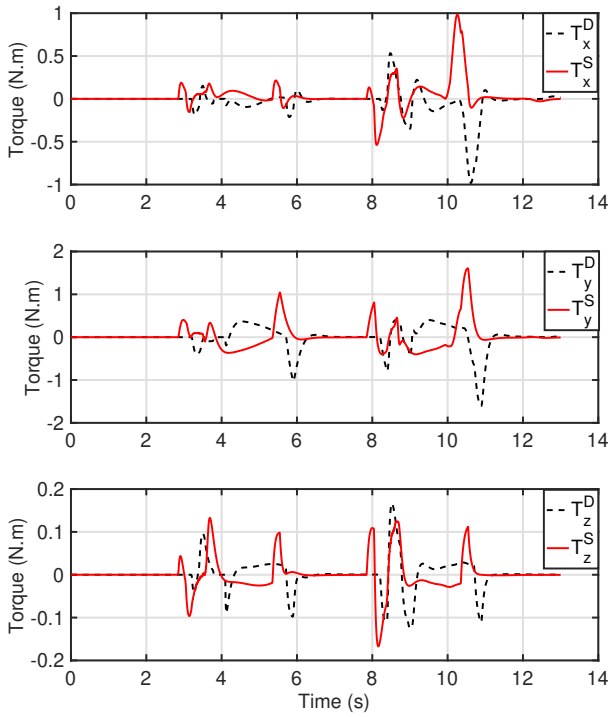

Figure 5.9: Master and slave Cartesian torques in the tool frame, drift compensator on – $T_{rt} = 700$ ms.

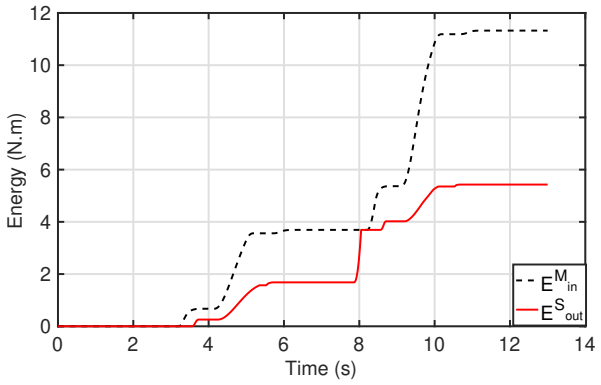

Figure 5.10: Master-in and slave-out energies, drift compensator on – $T_{rt} = 700$ ms.

Chapter 6

Conclusions and Future Work

This work presented an overview of the Time Domain Passivity Approach applied in order to passivate the communication channel in time-delayed bilateral teleoperation. Two constructions of the passivity-observer/passivity-controller pair were applied. The first was a concatenated version, in which the excess of energy is dissipated in order to make each degree of freedom passive. The second approach is a coupled version, where the total energy of the Cartesian space is computed and the dissipation is distributed according to the inertia of each link. This approach had been previously shown to work in impedance configuration for haptic interaction with virtual environments. However, to the best of the author's knowledge, this is the first time where the admittance case is presented and its efficacy is shown in bilateral teleoperation tasks.

Adding to that, a novel 1-DoF TDPA-based drift compensator method has been presented. It has been shown that the presented approach is able to compensate for the drift caused by the admittance-type passivity controller while keeping the control forces in the normal range of the teleoperation task. The efficacy of the proposed method and its performance compared with previous approaches has been demonstrated through its application to teleoperation of a 1-DoF setup.

Subsequently, an extension of the previously proposed TDPA-based drift compensators to multi-DoF Cartesian-Space teleoperation has been presented. A convergence analysis has also been provided. It has been shown that, if the gain is set within certain bounds, the proposed approach is able to reduce the drift caused by the passivity controller in case it is able to do so without violating the passivity condition. That analysis also provided an insight about the cause of force spikes, which are generated when the drift converges within one time step. In addition, hardware experiments with two translational 3-DoF off-the-shelf haptic devices, as well as with the DLR Bimanual Haptic Device, demonstrated the applicability of the proposed compensator to time-delayed bilateral teleoperation of multi-DoF devices, when using both concatenated and coupled implementations of the PO-PC pair.

Moreover, a dynamically decoupling control strategy was presented. Such approach allows the control of redundant manipulators in a hierarchical manner, where a secondary task is performed in the null space of the main one. Numerical validation demonstrated the efficacy of such approach in controlling the Cartesian space of an aerial manipulator while keeping the flying base joints as close to zero as possible and using one of the robotic arm joints to increase the manipulability of the system.

Finally, by using the dynamically decoupled controller, the coupled PO-PC implementation, and the proposed multi-DoF drift compensator, time-delayed bilateral teleoperation of the Cartesian space of a redundant aerial manipulator was simulated. The efficacy of the proposed multi-DoF approach in compensating the drift and preserving the tracking performance of the local controller has been demonstrated in the presence of 700 ms round-trip delays.

Future work will involve studying meaningful haptic feedback and null-space controller passivation for applying bilateral teleoperation techniques to the null space of redundant aerial manipulators.

Bibliography

[1] OLLERO, A., HEREDIA, G., FRANCHI, A., et al. "The aeroarms project: Aerial robots with advanced manipulation capabilities for inspection and maintenance", *IEEE Robotics and Automation Magazine*, 2018.

[2] RUGGIERO, F., LIPPIELLO, V., OLLERO, A. "Aerial manipulation: A literature review", *IEEE Robotics and Automation Letters*, v. 3, n. 3, pp. 1957–1964, 2018.

[3] LEE, J., BALACHANDRAN, R., SARKISOV, Y., et al. "Visual-Inertial Telepresence for Aerial Manipulation". In: *International Conference on Robotics and Automation (ICRA) (submitted)*, 2020.

[4] SARKISOV, Y., KIM, M. J., COELHO, A., et al. "Optimal Oscillation Damping Control of cable-Suspended Aerial Manipulator with a Single IMU Sensor". In: *International Conference on Robotics and Automation (ICRA) (submitted)*, 2020.

[5] COELHO, A., SINGH, H., OTT, C., et al. "Whole-Body Bilateral Teleoperation of a Redundant Aerial Manipulator". In: *International Conference on Robotics and Automation (ICRA) (submitted)*, 2020.

[6] THOMAS, J., POLIN, J., SREENATH, K., et al. "Avian-inspired grasping for quadrotor micro UAVs". In: *ASME 2013 international design engineering technical conferences and computers and information in engineering conference*, pp. V06AT07A014–V06AT07A014. American Society of Mechanical Engineers, 2013.

[7] MCARTHUR, D. R., CHOWDHURY, A. B., CAPPELLERI, D. J. "Design of the I-BoomCopter UAV for environmental interaction". In: *2017 IEEE International Conference on Robotics and Automation (ICRA)*, pp. 5209–5214. IEEE, 2017.

[8] RYLL, M., BICEGO, D., FRANCHI, A. "A truly redundant aerial manipulator exploiting a multi-directional thrust base", *IFAC-PapersOnLine*, v. 51, n. 22, pp. 138–143, 2018.

[9] KONDAK, K., HUBER, F., SCHWARZBACH, M., et al. "Aerial manipulation robot composed of an autonomous helicopter and a 7 degrees of freedom industrial manipulator". In: *2014 IEEE international conference on robotics and automation (ICRA)*, pp. 2107–2112. IEEE, 2014.

[10] KIM, M. J., KONDAK, K., OTT, C. "A stabilizing controller for regulation of uav with manipulator", *IEEE Robotics and Automation Letters*, v. 3, n. 3, pp. 1719–1726, 2018.

[11] KIM, M. J., BALACHANDRAN, R., DE STEFANO, M., et al. "Passive compliance control of aerial manipulators". In: *2018 IEEE/RSJ International Conference on Intelligent Robots and Systems (IROS)*, pp. 4177–4184. IEEE, 2018.

[12] SARKISOV, Y. S., KIM, M. J., BICEGO, D., et al. "Development of SAM: cable-Suspended Aerial Manipulator". In: *IEEE International Conference on Robotics and Automation (ICRA)*, 2019.

[13] SCHMAUS, P., LEIDNER, D., KRÜGER, T., et al. "Preliminary insights from the meteron supvis justin space-robotics experiment", *IEEE Robotics and Automation Letters*, v. 3, n. 4, pp. 3836–3843, 2018.

[14] LII, N. Y., LEIDNER, D., BIRKENKAMPF, P., et al. "Toward Scalable Intuitive Teleoperation of Robots for Space Deployment with the METERON SUPVIS Justin Experiment". In: *Proceedings of the 14th Symposium on Advanced Space Technologies for Robotics and Automation (ASTRA)*, 2017.

[15] ARTIGAS, J., BALACHANDRAN, R., RIECKE, C., et al. "Kontur-2: force-feedback teleoperation from the international space station". In: *2016 IEEE International Conference on Robotics and Automation (ICRA)*, pp. 1166–1173. IEEE, 2016.

[16] PANZIRSCH, M., RYU, J.-H., FERRE, M. "Reducing the conservatism of the time domain passivity approach through consideration of energy reflection in delayed coupled network systems", *Mechatronics*, v. 58, pp. 58–69, 2019.

[17] SINGH, H., PANZIRSCH, M., COELHO, A., et al. "Position Synchronization of Delayed Robot Coupling with Proxy-based Approach". In: *International Conference on Robotics and Automation (ICRA) (submitted)*, 2020.

[18] PANZIRSCH, M., COELHO, A., SINGH, H., et al. "The 6-DoF Implementation of the 4-Channel Time Domain Passivity Approach for Delayed Teleoperation", *IEEE/ASME Transactions on Mechatronics (submitted)*, 2020.

[19] ANDERSON, R. J., SPONG, M. W. "Bilateral control of teleoperators with time delay", *IEEE Transactions on Automatic control*, v. 34, n. 5, pp. 494–501, 1989.

[20] NIEMEYER, G., SLOTINE, J.-J. "Stable adaptive teleoperation", *IEEE Journal of oceanic engineering*, v. 16, n. 1, pp. 152–162, 1991.

[21] HANNAFORD, B., RYU, J.-H. "Time-domain passivity control of haptic interfaces", *IEEE Transactions on Robotics and Automation*, v. 18, n. 1, pp. 1–10, 2002.

[22] RYU, J.-H., ARTIGAS, J., PREUSCHE, C. "A passive bilateral control scheme for a teleoperator with time-varying communication delay", *Mechatronics*, v. 20, n. 7, pp. 812–823, 2010.

[23] BALACHANDRAN, R., ARTIGAS, J., MEHMOOD, U., et al. "Performance comparison of wave variable transformation and time domain passivity approaches for time-delayed teleoperation: Preliminary results". In: *2016 IEEE/RSJ International Conference on Intelligent Robots and Systems (IROS)*, pp. 410–417. IEEE, 2016.

[24] ARTIGAS, J., RYU, J.-H., PREUSCHE, C. "Time domain passivity control for position-position teleoperation architectures", *Presence: Teleoperators and Virtual Environments*, v. 19, n. 5, pp. 482–497, 2010.

[25] ARTIGAS, J., RYU, J.-H., PREUSCHE, C. "Position drift compensation in time domain passivity based teleoperation". In: *2010 IEEE/RSJ International Conference on Intelligent Robots and Systems (IROS)*, pp. 4250–4256. IEEE, 2010.

[26] CHAWDA, V., VAN QUANG, H., O'MALLEY, M. K., et al. "Compensating position drift in time domain passivity approach based teleoperation". In: *2014 IEEE Haptics Symposium*, pp. 195–202. IEEE, 2014.

[27] BULLO, F., LEWIS, A. D. *Geometric control of mechanical systems: modeling, analysis, and design for simple mechanical control systems*, v. 49. Springer Science & Business Media, 2004.

[28] BULLO, F., MURRAY, R. M. "Proportional Derivative (PD) Control on The Euclidean Group". 1995.

[29] MURRAY, R. M. *A mathematical introduction to robotic manipulation*. CRC press, 1994.

[30] COELHO, A., SINGH, H., MUSKARDIN, T., et al. "Smoother Position-Drift Compensation for Time Domain Passivity Approach Based Teleoperation". In: *2018 IEEE/RSJ International Conference on Intelligent Robots and Systems (IROS)*, pp. 5525–5532. IEEE, 2018.

[31] COELHO, A., OTT, C., SINGH, H., et al. "Multi-DoF Time Domain Passivity Approach Based Drift Compensation for Telemanipulation". In: *2019 19th International Conference on Advanced Robotics (ICAR)*, 2019.

[32] KHALIL, H. K. *Nonlinear systems*, v. 3. Upper Saddle River, NJ, Prentice Hall, 2002.

[33] LAWRENCE, D. A. "Stability and transparency in bilateral teleoperation", *IEEE transactions on robotics and automation*, v. 9, n. 5, pp. 624–637, 1993.

[34] ARTIGAS, J., RYU, J.-H., PREUSCHE, C., et al. "Network representation and passivity of delayed teleoperation systems". In: *2011 IEEE/RSJ International Conference on Intelligent Robots and Systems (IROS)*, pp. 177–183. IEEE, 2011.

[35] OTT, C., ARTIGAS, J., PREUSCHE, C. "Subspace-oriented energy distribution for the time domain passivity approach". In: *2011 IEEE/RSJ International Conference on Intelligent Robots and Systems*, pp. 665–671. IEEE, 2011.

[36] HULIN, T., HERTKORN, K., KREMER, P., et al. "The DLR bimanual haptic device with optimized workspace". In: *2011 IEEE International Conference on Robotics and Automation*, pp. 3441–3442. IEEE, 2011.

[37] OTT, C., DIETRICH, A., ALBU-SCHÄFFER, A. "Prioritized multi-task compliance control of redundant manipulators", *Automatica*, v. 53, pp. 416–423, 2015.

[38] DIETRICH, A., OTT, C., ALBU-SCHÄFFER, A. "An overview of null space projections for redundant, torque-controlled robots", *The International Journal of Robotics Research*, v. 34, n. 11, pp. 1385–1400, 2015.

[39] TOGNON, M., FRANCHI, A. "Omnidirectional aerial vehicles with unidirectional thrusters: Theory, optimal design, and control", *IEEE Robotics and Automation Letters*, v. 3, n. 3, pp. 2277–2282, 2018.

[40] ALBU-SCHÄFFER, A., HADDADIN, S., OTT, C., et al. "The DLR lightweight robot: design and control concepts for robots in human environments", *Industrial Robot: an international journal*, v. 34, n. 5, pp. 376–385, 2007.

[41] GAROFALO, G., OTT, C., ALBU-SCHÄFFER, A. "On the closed form computation of the dynamic matrices and their differentiations". In: *2013 IEEE/RSJ International Conference on Intelligent Robots and Systems (IROS)*, pp. 2364–2359. IEEE, 2013.

[42] "ROS Wiki – URDF Tutorials". `http://wiki.ros.org/urdf/Tutorials`. Accessed: 2019-11-16.

[43] SICILIANO, B., SCIAVICCO, L., VILLANI, L., et al. *Robotics: modelling, planning and control*. Springer Science & Business Media, 2010.